

**Table-top tunable narrow-band
extreme-ultraviolet sources:
from low to high-order optical harmonic
generation**

VRIJE UNIVERSITEIT

**Table-top tunable narrow-band
extreme-ultraviolet sources:
from low to high-order optical harmonic
generation**

ACADEMISCH PROEFSCHRIFT

ter verkrijging van de graad van doctor aan
de Vrije Universiteit Amsterdam,
op gezag van de rector magnificus
prof.dr. T. Sminia,
in het openbaar te verdedigen
ten overstaan van de promotiecommissie
van de faculteit der Exacte Wetenschappen
op donderdag 1 juli 2004 om 15.45 uur
in het auditorium van de universiteit
De Boelelaan 1105

door

Fernando Brandi

geboren te Pisa, Italië

promotor: prof.dr. W.M.G. Ubachs

A Roberta,
per la pazienza avuta.

Contents

1	Introduction	1
1.1	Optical harmonic generation	1
1.2	Low-order harmonic generation	3
1.2.1	Perturbative solution	3
1.2.2	VUV sources for high-resolution spectroscopy	7
1.3	Photoionization mechanisms	11
1.4	High-order harmonic generation	13
1.4.1	The semiclassical model	13
1.4.2	Propagation effects	14
1.4.3	Generation of tunable coherent XUV radiation	18
I	LHG applied to high-resolution VUV spectroscopy	23
2	High-resolution photoionization spectroscopy of xenon	25
2.1	Introduction	25
2.2	Experiment	26
2.3	Results and Discussion	27
2.3.1	Hyperfine Splitting	27
2.3.2	Isotope Shift	29
2.3.3	Absolute Calibration	33
2.4	Conclusions	35
3	High-resolution photoionization spectroscopy of krypton	37
3.1	Introduction	37
3.2	Experimental setup and procedure	39
3.2.1	1VUV+1UV photoionization spectroscopy	39
3.2.2	2UV+1UV photoionization spectroscopy	40
3.3	Experimental results and discussion	41
3.3.1	Isotope Shift	41
3.3.2	Absolute frequency calibration	45
3.3.3	ac Stark effect	47
3.3.4	Consequences for narrow-band XUV/VUV generation	49
3.4	Conclusions	51

3.5	Appendix: new determination of the ionization energy of krypton	51
II	A novel setup for narrow-band HHG	53
4	Laser system	55
4.1	Introduction	55
4.2	Laser system	57
4.2.1	cw-seeder	57
4.2.2	Pump and compressor	58
4.2.3	Pulsed-dye-amplifier	58
4.2.4	Ti:Sapphire amplifier	61
4.3	Characterization of the laser system	62
4.3.1	Temporal and frequency characteristics	62
4.3.2	Spatial beam quality	64
5	Narrow-band high-order harmonic generation	67
5.1	Introduction	67
5.2	Experiment and results	69
5.3	Discussion	71
5.3.1	Absolute frequency of the harmonics	71
5.3.2	Bandwidths of the harmonics	71
5.3.3	Tunability of the harmonics	72
5.4	Conclusions	74
5.5	Appendix: determination of the number of XUV photons	74
6	High-resolution investigation of frequency chirp in HHG	79
6.1	Introduction	79
6.2	Experimental setup and procedure	81
6.3	Results and interpretation	84
6.4	Discussion	89
6.5	Conclusions and outlook	91
6.6	Appendix: measurement of the frequency shift in the amplifier chain . .	92
6.6.1	Experimental setup and technique	92
6.6.2	Misalignment effect	94
	Samenvatting	97
	Summary	99

Riassunto	101
Acknowledgments	103
Publications	105
Bibliography	107

Chapter 1

Introduction

The process of harmonic generation with laser radiation and its use for high-resolution spectroscopy are presented. In specific, low and high-order harmonic generation in gaseous media as a source of coherent radiation in the vacuum-ultraviolet (VUV, 200-100 nm) and extreme-ultraviolet (XUV, 100-10 nm) are discussed. A description of photoionization mechanisms in intense laser pulses is also given. Spectroscopic application of low-order harmonic generation and wave-mixing, as well as recent progress and future prospects in the use of high-order harmonic generation for the development of a continuously tunable narrow-band table-top XUV source are presented.

1.1 Optical harmonic generation

Optical harmonic generation (OHG) is the prototype process of nonlinear optics, the study of the interaction between intense optical radiation and matter. In the physical process of OHG an intense light field interacting with matter produces radiation at spectral components, called harmonics, with frequencies at integer multiples of the fundamental frequency. Experimental investigations of nonlinear optics have become possible only with the invention of the laser [1] which made available sufficiently intense light beams; the first nonlinear optical phenomenon observed has been the generation of second harmonics in a crystal in 1961 [2].

Low-order harmonic generation (LHG), $q \leq 5$, is a nonlinear optical process that can be fully explained with a perturbative solution of Maxwell's equations. At light intensities needed to trigger LHG process, typically in the range $10^9 - 10^{12}$ W/cm², the optical response of a medium is determined by the dipole moment per unit volume, or polarization, which can be expressed as a power series in the electric field associated with an intense light beam. Harmonic radiation is produced with an efficiency that rapidly decreases with the harmonic order, as is schematically shown in Figure 1.1(a). Note that in an isotropic medium, e.g., gases, for symmetry reasons only odd harmonics are produced. In most practical cases LHG is used to produce coherent electromagnetic radiation at those short wavelengths where laser radiation is not available, at least not in tunable or narrow-band form. A key prerequisite for efficient frequency conversion is the availability of a nonlinear material transparent at both the fundamental and the harmonic frequency. Crystals are routinely used to up-convert near-infrared and visible laser radiation, generating radiation down to the deep ultraviolet, with efficiencies up to 50%. However, generation of short wavelength

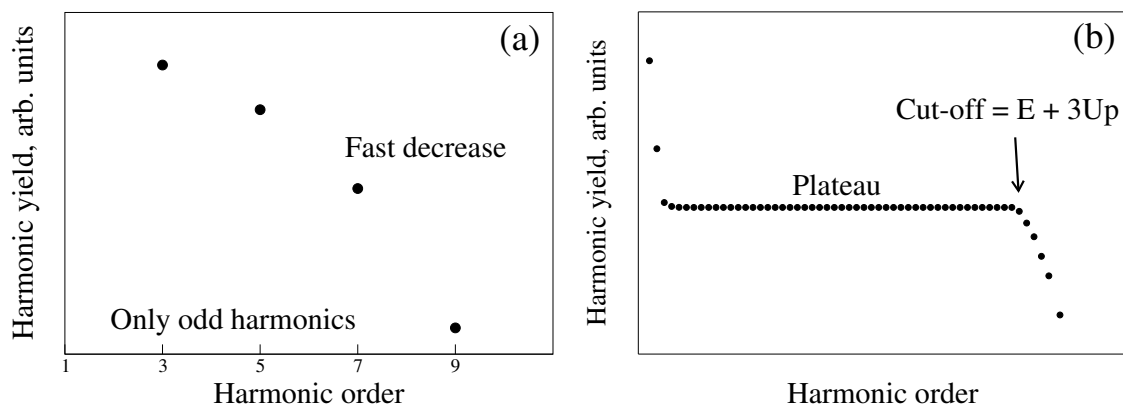


Figure 1.1. Schematic presentation of the typical spectra from low (a) and high (b) order harmonic generation in gases.

harmonics in crystals is not possible due to the lack of transparent materials below 200 nm. Thus, the production of vacuum-ultraviolet (200-100 nm) and extreme-ultraviolet (100-10 nm) harmonic radiation is feasible only in gaseous media, but at much lower efficiency, typically $10^{-4} - 10^{-7}$.

The development in the last two decades of high-power ps and fs pulsed lasers, has brought the discovery of new features in optical harmonic generation. Notably, it has been found that at very high field intensity, $I \geq 10^{13} \text{ W/cm}^2$, a plateau in the harmonic generation efficiency is reached, as is schematically shown in Figure 1.1(b). At such high intensities the atoms are ionized by the laser pulse and perturbation theory is no longer valid. Harmonic generation in the high field regime can be understood in terms of a semiclassical approach, the so-called *three-step model*: first the atom is ionized by the intense laser field, then the free electron accelerates in the laser field and finally it recombines with the parent ion. This model predicts a *cutoff* at a photon energy of about $E + 3U_p$, where E is the ionization energy of the atom and U_p is the ponderomotive energy of an electron in the intense laser field. This nonlinear optical process, called high-order harmonic generation (HHG), has an efficiency that is orders of magnitude lower than LHG, typically $10^{-8} - 10^{-11}$ [3]. However, efficiencies on the order of $10^{-6} - 10^{-7}$ can be obtained if special interaction geometries are used, e.g., gas filled hollow fibers [4] or valves with a slit opening [5]. Nowadays, HHG has become a leading research field in nonlinear optics as a way to produce coherent soft-X-rays and attosecond pulses. Generation of radiation in the water window [6] and of sub-femtosecond pulses [7] has already been demonstrated.

In the following Sections OHG in gases for the generation of tunable narrow-band XUV coherent radiation is described. In Section 1.2 the basic perturbation theory of LHG in gases is presented and applications of the generated VUV radiation in high-resolution spectroscopy is discussed. In Section 1.3 the onset of the photoionization mechanism of an atom in an intense laser field is presented. Finally, in Section 1.4 a semi-classical model for HHG in gases is presented, and the use of high-order harmonics in spectroscopic applications discussed.

1.2 Low-order harmonic generation

1.2.1 Perturbative solution

When an intense laser pulse interacts with a gas two main processes can occur: emission of electromagnetic radiation and ionization of the atoms. At relatively low intensity, when no significant ionization is present, the field-atom interaction is successfully described by perturbative methods. This approach is valid for electric field strengths much smaller than the characteristic atomic field strength $E_{at} = e/(4\pi\epsilon_0 a_0^2) \sim 5 \times 10^{11}$ V/m, where e is the electron charge magnitude and a_0 is the Bohr radius, corresponding to an equivalent intensity of 3.5×10^{16} W/cm². The so-called *perturbative regime* in the field-matter interaction is defined for laser intensities up to 10^{13} W/cm².

When the ionization probability of the atoms is low and no free electrons are created, the nonlinear response of a gas excited by an intense laser pulse is well described in terms of the electric polarization, i.e., the average dipole moment per unit volume acquired by the atoms. An extensive presentation of LHG in gases is given in the book by Reintjes [8]. Here, a compact analysis is given, aiming at highlighting the principal characteristics of the process. The macroscopic polarization of the medium $P(r, t)$ can be expressed as a power series in the total electric field strength $E(r, t)$

$$P(r, t) = \epsilon_0[\chi^{(1)}E(r, t) + \chi^{(2)}E^2(r, t) + \chi^{(3)}E^3(r, t) + \dots], \quad (1.1)$$

where $\chi^{(1)}$ is the linear susceptibility, $\chi^{(3)}$ is the third-order susceptibility and so forth¹. The linear polarization $P_1(r, t) = \epsilon_0\chi^{(1)}E(r, t)$ is responsible for the wave propagation described by linear optics. The higher order susceptibilities have in general a tensor nature, however for isotropic media (e.g., gases) and linearly polarized light they reduce to scalar quantities. In the following discussion, it is assumed that only one pump beam is present, i.e., harmonic generation process.

The electromagnetic field involved in the nonlinear process is assumed to be linearly polarized and is expressed as a series of harmonics of the fundamentele frequency ω_1 ,

$$E(r, t) = \sum_q^q E_q(r, t) = \sum_q^q [A_q(r)e^{i(k_q z - \omega_q t)} + c.c.], \quad (1.2)$$

where $\omega_q = q\omega_1$ with q positive integer. The pump field ($q = 1$) is always much more intense than the harmonic field, so that the total electric field in Eq. (1.1) can be replaced by the fundamental field alone. In centrosymmetric media, like gases, all even terms in the power series vanish due to symmetry reasons (also related to parity conservation in multiphoton processes as schematically shown in Figure 1.2), and the nonlinear part of the polarization reduces to

$$P^{NL}(r, t) = \sum_q^q P_q(r, t) = \sum_q^q \epsilon_0\chi^{(q)}E_1^q(r, t), \quad (1.3)$$

with q odd.

¹The SI system of units is used in the thesis, unless explicitly stated otherwise.

Within the perturbative approach, the nonlinear polarizations $P_q(r, t)$ are considered source terms in the Maxwell's equations for the harmonic fields $E_q(r, t)$. Adopting the usual slowly-varying-amplitude approximation, i.e., variation of the electric field amplitude occurs only over distances much larger than an optical wavelength, the wave equation for the q^{th} harmonic field can be written as

$$2ik_q \frac{\partial A_q(r)}{\partial z} + \nabla_T^2 A_q(r) = -\frac{\omega_q^2}{c^2} \chi^{(q)} A_1^q(r) e^{i\Delta k_q z}, \quad (1.4)$$

where the so-called wave vector mismatch Δk_q is given by $qk_1 - k_q$. Considering the practical situation of a Gaussian laser beam the fundamental electric field can be expressed by

$$A_1(r) = A_{10} \frac{e^{-R^2/w_0^2(1+i\xi)}}{1+i\xi}, \quad (1.5)$$

where R is the cylindrical radial coordinate, i.e. $R^2 = x^2 + y^2$, $\xi = 2z/b$ is a normalized coordinate along the z axis with the zero set at the beam waist, $b = 2\pi w_0^2/\lambda$ is the beam confocal parameter, or two times the Rayleigh length, w_0 is the $1/e$ field radius of the beam waist and A_{10} is the electric field amplitude at $\xi = 0$ and $R = 0$. Integration of Eq. (1.4) for a Gaussian beam given by Eq. (1.5) yields the generated electric field amplitude at the q^{th} harmonic [9],

$$A_q(r) = \frac{i2\pi q\omega_1}{n_0 c} \chi^{(q)} F_q(\Delta k_q, z_0, z) A_{10}^q \frac{e^{-qR^2/w_0^2(1+i\xi)}}{1+i\xi}, \quad (1.6)$$

where n_0 is the linear index of refraction of the medium. The so-called phase matching integral $F_q(\Delta k_q, z_0, z)$, which describes the effect of de-phasing between the harmonic wave and its source polarization, is given by

$$F_q(\Delta k_q, z_0, z) = \int_{z_0}^z \frac{e^{i\Delta k_q z'}}{(1+2iz'/b)^{q-1}} dz', \quad (1.7)$$

with z_0 and z representing the starting and ending coordinates of the interaction region respectively. The intensity of the generated harmonic radiation is given by

$$\begin{aligned} I_q(r) &\equiv \frac{2n_0}{Z_0} |A_q(r)|^2 \\ &= \frac{8\pi^2 q^2 \omega_1^2}{n_0 c^2 Z_0} |\chi^{(q)}|^2 |F_q(\Delta k_q, z_0, z)|^2 A_{10}^{2q} \frac{|e^{-qR^2/w_0^2(1+i\xi)}|^2}{1+\xi^2}, \end{aligned} \quad (1.8)$$

where $Z_0 \equiv \sqrt{\epsilon_0/\mu_0} = 377\Omega$ is the impedance of free space. This expression shows the main characteristics of LHG process.

First, the peak intensity of the q^{th} harmonic, $I_q(0)$, is proportional to the q^{th} power of the peak intensity of the fundamental beam, $I_1(0) \propto A_{10}^2$. In principle, at sufficiently high pump powers the higher order harmonics could be produced more efficiently than the lower ones. However, the perturbative description is no longer valid at very high intensities comparable to the atomic electric field.

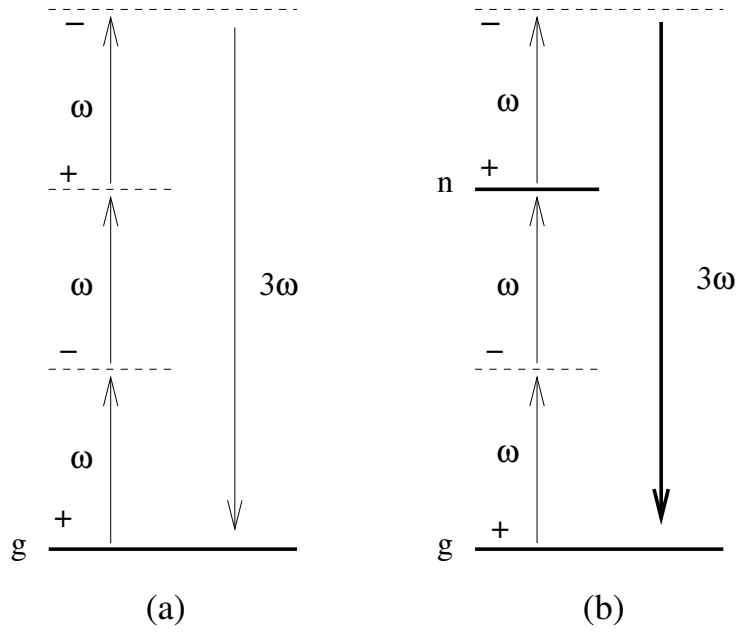


Figure 1.2. Schematic representation of third-harmonic generation: non-resonant (a), and two-photon resonant (b) cases. The dashed horizontal lines represent virtual states, while the solid lines are real atomic levels. Also shown is the parity of the states.

Second, I_q is proportional to the square of the q^{th} order nonlinear susceptibility, $|\chi^{(q)}|^2$. An analytical expression for the nonlinear susceptibilities can be obtained from quantum mechanical perturbation theory [9]. As an example the third order susceptibility describing third-harmonic generation (THG), as schematically shown in Figure 1.2(a), is given by

$$\chi^{(3)} = \frac{N}{\hbar^3} \sum^{m\nu v} \mu_{gv} \mu_{vn} \mu_{nm} \mu_{mg} \times \quad (1.9)$$

$$\left[\frac{1}{(\omega_{vg} - 3\omega)(\omega_{ng} - 2\omega)(\omega_{mg} - \omega)} + \frac{1}{(\omega_{vg} + \omega)(\omega_{ng} - 2\omega)(\omega_{mg} - \omega)} + \frac{1}{(\omega_{vg} + \omega)(\omega_{ng} + 2\omega)(\omega_{mg} - \omega)} + \frac{1}{(\omega_{vg} + \omega)(\omega_{ng} + 2\omega)(\omega_{mg} + 3\omega)} \right],$$

where N is the particle density, μ_{ij} are the dipole moments of the transition between states i and j , g refers to the ground state and the summation is performed over all intermediate states.

In writing Eq. (1.9) it is implicitly assumed that the frequencies involved in the process, ω , 2ω and 3ω are far from resonance, so that the denominators do not diverge. However, the occurrence of resonances enhances the susceptibility, thus increasing the harmonic generation efficiency. For the specific case of THG two-photon resonance

(see Figure 1.2(b)) is favorable compared to one-photon and three-photon resonances, since absorption of fundamental or generated fields leads to the depletion of third harmonic intensity. By substituting in Eq. (1.9), $\omega_{ng} \rightarrow (\omega_{ng} - i\Gamma_n/2)$, where Γ_n is the decay rate of level n , it is possible to write the expression of the two-photon resonance enhanced third-order nonlinear susceptibility describing THG

$$\chi_{res}^{(3)} = \frac{N}{\hbar^3} \sum^{mnv} \mu_{gv} \mu_{vn} \mu_{nm} \mu_{mg} \times \quad (1.10)$$

$$\left\{ \frac{1}{(\omega_{mg} - \omega)(\omega_{ng} - 2\omega - i\Gamma_n/2)} \left[\frac{1}{(\omega_{vg} - 3\omega)} + \frac{1}{(\omega_{vg} + \omega)} \right] \right.$$

$$\left. + \frac{1}{(\omega_{vg} + \omega)(\omega_{ng} + 2\omega - i\Gamma_n/2)} \left[\frac{1}{(\omega_{mg} - \omega)} + \frac{1}{(\omega_{mg} + 3\omega)} \right] \right\},$$

where the first term inside the curly brackets represents the actual resonant contribution.

To achieve optimum energy conversion from the pump beam to the harmonic beam the field strength E_q has to stay in phase with its source polarization P_q . Calculation of the phase matching integral $F_q(\Delta k_q, z, z_0)$ (see Eq. (1.7)) shows a strong dependence on the focusing condition. For a beam with $b \gg |z|, |z_0|$, usual for experiments employing a gas jet, the phase matching integral approaches the sinc^2 function, typical of the phase matching for plane-waves, where maximum efficiency is achieved at $\Delta k_q \sim 0$. In this configuration harmonic generation is allowed for both negative and positive values of wave vector mismatch.

In the opposite case of tight-focusing, $b \ll |z|, |z_0|$, typical for LHG in cells, F_q has a maximum for positive values of Δk_q , and is zero for $\Delta k_q \leq 0$. This peculiar behavior can be understood in terms of the Gouy phase, $\tan^{-1}(2z/b)$ [9], which describes the on-axis space-dependent phase shift between a Gaussian beam and a plane wave beam. Because of the Gouy phase, there is a change in the sign of the phase lag between the field E_q and the source polarization P_q when passing through the beam focus. As a consequence, the harmonic field generated in first half of the interaction region would be converted back to the pump beam in the second half, if no compensating wave vector mismatch is present. One important consequence of this behavior is that THG is not possible in a positive (or normal) dispersive medium, like single component gases far from resonances. This characteristic, however, is not typical for all third order nonlinear parametric processes. An important exception is that of difference frequency mixing processes, (e.g. $\omega_1 - \omega_2 - \omega_3 \rightarrow \omega_4$, $2\omega_1 - \omega_2 \rightarrow \omega_4$, and $\omega_1 + \omega_2 - \omega_3 \rightarrow \omega_4$), for which the phase matching integral has the opposite behavior, i.e. is maximized for negative values of Δk_q , so that phase matching in the tight focusing limit is achieved in positive dispersive media [8, 10]. This characteristic makes difference frequency mixing processes attractive for efficient production of VUV radiation.

To quantitatively assess the limit of the perturbative approach, evaluation of the nonlinear susceptibility of atoms in a high laser fields can be performed by direct numerical integration of the time-dependent Schrödinger equation. As an example, in Figure 1.3 results of such a calculation for several noble gases are presented assuming a pulse duration of about 10 cycles at $\omega = 1.55$ eV ($\lambda = 800$ nm) [11]. Here, $\Delta\chi(\omega) = \chi^{(3)}(\omega)I(\omega) + \chi^{(5)}(\omega)I^2(\omega) + \dots$, is the complex intensity-dependent part of

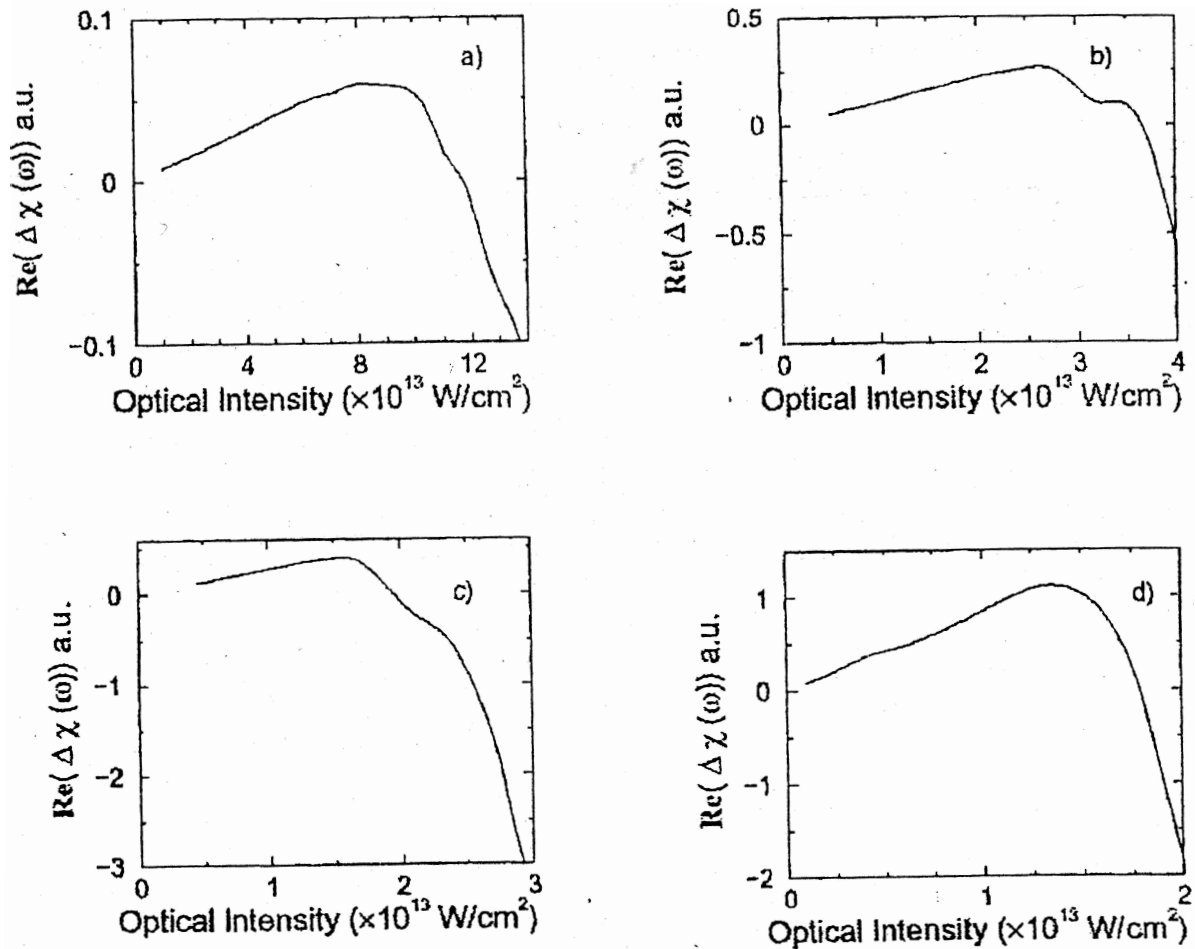


Figure 1.3. Calculation for the real part of the complex intensity-dependent susceptibility for Ne, Ar, Kr and Xe (graphs a), b), c) and d) respectively) as reported in Ref. [11].

the total susceptibility $\chi(\omega)$ defined as $P(\omega) = \chi(\omega)E(\omega)$. Note that in the above relations atomic units are used. Figure 1.3 shows the initial linear increase of $\text{Re}(\Delta\chi(\omega))$ for intensities of few times 10^{13} W/cm². This behavior agrees with the predictions of perturbation theory, and is due to the dominant contribution of the smallest perturbative term $\chi^{(3)}(\omega)I(\omega)$. The break-down of the perturbative approach is clearly visible as the intensity increases: the higher order nonlinear susceptibilities overcome the third, violating the basic assumption of the perturbation theory. Similar calculations performed for atomic hydrogen result also in the break-down of the perturbative theory for intensities in the range $10^{13} - 10^{14}$ W/cm² [12].

1.2.2 VUV sources for high-resolution spectroscopy

After the invention of the laser the nonlinear polarization induced by a strong laser field in a medium was identified by Bloembergen and coworkers [13] as an efficient source of coherent light. Soon thereafter Ward and New demonstrated THG in gases, producing deep-UV radiation at 231 nm, using a pulsed Ruby laser [14]. The production of short wavelength radiation by harmonic up-conversion in gaseous media has

been the subject of a large number of investigations and we wish to mention the pioneering groups and scientists in this field. Harris and coworkers at Stanford were the first to demonstrate phase-matching in metal vapors early in the 1970's [15, 16] and this group has been involved in experimental progress over three decades. Also in the early 1970s Hodgson, Sorokin, and Wynne made a leap forward by demonstrating the use of two tunable dye lasers for a resonance enhancement scheme producing tunable VUV light [17]. In the late 1970's Bjorklund carried out a detailed study on phase-matching conditions in noble gases [10], while Reintjes and coworkers investigated the scaling law of LHG with laser intensity [18]. On the technological side an important advancement was the introduction of the pulsed supersonic gas jet technique by Kung [19], which made it much easier to experiment in the so-called windowless wavelength range, below the cut-off of LiF at $\lambda = 105$ nm. Further pioneers were Wallenstein and coworkers in the 1980's, with a large number of contributions focusing on resonance enhanced and phase-matched VUV and XUV production, particularly in noble gases [20, 21]. Still in the 1980's the group of Rhodes introduced the use of excimer lasers for the generation of VUV [22, 23]. Important reviews were written by Stoicheff [24] and by Vidal [25], two further explorers of the VUV domain.

One of the main applications of nonlinear up-conversion in gases is the possibility to generate tunable narrow-band coherent VUV/XUV radiation with a table-top set-up. However, the low efficiency of nonlinear processes in gases poses a great challenge to the development of such sources. As shown by Eq. (1.6), there are basically three possibilities to increase the LHG efficiency, namely: (i) optimum phase matching, (ii) high-intensity fundamental beam and (iii) resonant enhancement.

(i) Phase matching optimization of LHG in gases is strongly dependent on the focusing condition. In practical situations the fundamental beam has to be focused in order to achieve sufficiently high intensity in the interaction region and at the same time avoid damage on the optics by the high energy of the pump pulses. Optimum phase matching in this situation is achieved in negatively dispersive or dispersionless media. This is not in general the case for single component gases, but specific gas mixtures can be used to achieve optimum phase matching. For example, in Ref. [26] a cell containing a mixture of normally dispersive argon and negatively dispersive cadmium vapor was used to produce phase-matched VUV radiation. In general however, this phase matching condition is difficult to control when using a gas jet as nonlinear medium, which is the usual experimental situation. Moreover, since phase matching is by its nature wavelength-dependent, there are fundamental limitations when tunable radiation is used.

(ii) The production of tunable narrow-band VUV/XUV radiation via LHG requires the use of a tunable narrow-band high-intensity fundamental UV beam. The lack of primary sources in the UV can be overcome by frequency doubling intense visible pulses. Such laser source was developed in the late 1980's by Kung and coworkers [27], who were the first to combine the pulsed-dye-amplification technique with harmonic generation in gases. Due to the fast decay rate of dyes (nanoseconds for visible dyes, and even hundreds of picosecond for near-infrared dyes) the production and subsequent amplification of a laser pulse in dye cells enables the genera-

tion of energetic pulses that follow the temporal characteristic of the pump pulses. Thus, pulsed amplification of a cw tunable seeding beam by a single-mode pump laser with a smooth pulse time profile and a stable intensity, e.g., from an injection-seeded Q-switched laser, enables the generation of energetic visible pulses with a Fourier-transform limited frequency spectrum. In this way, Kung and coworkers were able to produce tunable VUV radiation with a bandwidth of 210 MHz, which they used to perform high-resolution frequency domain spectroscopy leading to the accurate determination of Isotope Shift (IS) and Hyperfine Splitting (HFS) of several levels of krypton [28]. Using the pulsed-dye-amplification technique Eikema and coworkers [29] efficiently produced narrow-band radiation at 58 nm via fifth-harmonic generation in a gas jet and accurately determined the IS between ^3He and ^4He in the ($1^1\text{S}-2^1\text{P}$) transition. This source has been used to perform accurate frequency domain spectroscopy of noble gases, as reported in Chapters 2 and 3, and molecules [30, 31, 32]. As an example, Figure 1.4 shows the laser system configuration used to perform mass resolved photoionization spectroscopy on xenon reported in Chapter 2.

For precision studies, the absolute frequency of the exciting radiation must be accurately calibrated. The frequency of the harmonics can easily be inferred from the one of the pump pulse by $\omega_q = q \times \omega_1$, where q is the harmonic order. For the specific case of a cw-seeded amplifier, the central frequency of the pump pulses can be determined by accurate metrology on the cw-seeding light. However, it is well known that frequency chirp occurs during the amplification and harmonic generation processes [33], as a consequence of the time dependence of the index of refraction. Frequency shift of tens of MHz are possible during the amplification of the visible frequency, introducing an uncertainty up to several hundredths of a wavenumber in the absolute harmonic frequency. To overcome this limitation, an original chirp compensation technique was developed by Eikema and coworkers [34], that leads to the accurate determination of the 1^1S Lamb shift in helium.

(iii) The nonlinear response of a medium, i.e., its nonlinear susceptibility, is enhanced when the pump frequency meets a (multi-photon)resonant transition. However, the production of tunable radiation via a resonant scheme is not possible using only one pump frequency, like in THG, since the resonant condition cannot be kept while tuning the pump frequency. On the other side, efficient production of tunable VUV radiation is possible using resonantly enhanced four-wave-mixing (REFWM) schemes: one fixed frequency, ω_1 , matches an atomic transition, and mixes with another tunable frequency, ω_2 , in order to generate tunable radiation. REFWM has been extensively studied in atomic vapors [35, 36, 37], molecular gases [38, 39, 40, 41] and noble gases [20, 21, 41, 42, 43]. Especially the ultraviolet two-photon transitions in noble gases have been found to be very efficient for the production of VUV radiation via REFWM.

Tunable radiation generated via REFWM using the two-photon ($4p^6 - 4p^55p[1/2]_0$) transition in krypton ($\omega_{\text{VUV}} = 2\omega_1 + \omega_2$) has been applied to accurately determine the dissociation energy of hydrogen and deuterium molecules [44, 45]. The accuracy of this measurement relies on the correct determination of the laser frequencies involved in the REFWM process. Although it is usually possible to precisely measure the visible frequency ω_2 , the value of the fixed UV frequency ω_1 , inferred from the two-photon transition frequency, may be not so accurate. For example, possible drift of ω_1 , which

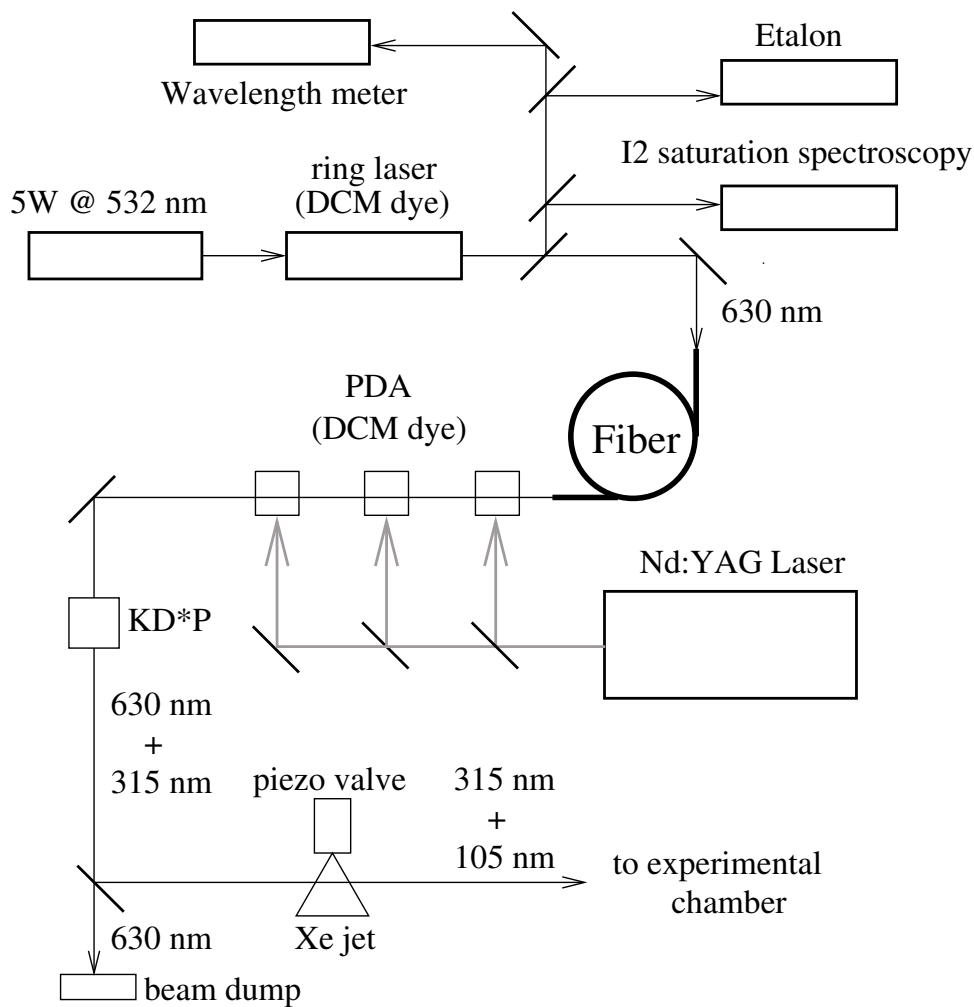


Figure 1.4. Schematic of the narrow-band VUV/XUV source developed by Eikema and coworkers [29]. In particular, this is the configuration used to perform high-resolution mass resolved photoionization spectroscopy of xenon presented in Chapter 2.

does not effect the VUV yield due to the large power broadening of the two photon transition, may be a source of uncertainty.

Recently, a laser source based on the same REFWM scheme was developed at the ETH in Zürich, yielding tunable XUV radiation with a 0.008 cm^{-1} bandwidth [46] and an absolute accuracy of 0.02 cm^{-1} limited by the drift in the UV frequency ω_1 . A modified version of this source, employing the two-photon ($4p^6 - 4p^5 5p'[1/2]_0$) transition in krypton, was used to accurately measure Rydberg series in krypton [47, 48], resulting in a new value of the ionization energy with an accuracy of 0.016 cm^{-1} (see Section 3.5). The higher frequency accuracy was obtained by a locking scheme used to stabilize the UV frequency ω_1 against the Doppler-broadened profile of a well known iodine line. If locking to a Doppler-free iodine line is used instead and chirp evaluation and correction is performed, an XUV source based on REFWM with sub- 0.001 cm^{-1} absolute accuracy might be feasible.

A new tunable laser source based on REFWM using a F_2 excimer laser (157 nm) and the tripled output of two dye lasers, and generating narrow band (0.2 cm^{-1}) XUV

radiation up to 20 eV has recently been demonstrated by Rupper and Merkt [49].

1.3 Photoionization mechanisms

Within perturbation theory, photoionization of an atom may occur via the so-called multiphoton ionization (MPI) process. When the ionization energy E is higher than the photon energy $\hbar\omega$, which is the case for noble gases exposed to the common powerful infrared lasers (Nd:YAG and Ti:Sapphire), several photons must be absorbed to ionize the atom. The ionization rate in the MPI process is given by $\sigma_n I^n$, where n is the minimum number of photons necessary to ionize the atom, σ_n is the generalized cross-section and I is the light intensity. The dependence of the generalized cross-section on the exciting frequency is in general weak, except when a multiphoton resonance is met. Then the value of the cross-section is strongly frequency dependent. Due to the high degree of nonlinearity the MPI process saturates as the laser intensity increases: the ionization rate no longer follows the usual power law as the intensity increases above a certain value called the saturation intensity. In practice, for laser pulses of given time duration τ , the saturation intensity I_s is defined as the *peak* intensity at which the probability of one atom to be ionized during the pulse approaches one. Thus, the longer τ the smaller I_s , specifically, $I_s \propto \tau^{-\frac{1}{n}}$.

Experimental investigations of MPI of gases have been carried out with laser pulses of varying time duration ranging from few to few tens of ps [50, 51, 52, 53]. The resulting saturation intensity has always been found to be in the $10^{13} - 10^{14}$ W/cm² intensity range. Closed-form solutions for the ion yield from multiphoton ionization in collisionless gases have been calculated in Ref. [54] assuming a laser beam of Gaussian spatial profile with a squared hyperbolic-secant time envelope. Integration of the ionization rate equation results in the following formula for the peak strength of the electric field at saturation for the singly-charged ion yield:

$$A_{0,s}(E, \tau) = \frac{1.8E^3}{[1.5E(2n+1)^{(2n+1)}e^{-(2n+1)}B(\frac{1}{2}, n)]^{\frac{1}{2n}}} \times \tau^{-\frac{1}{2n}}, \quad (1.11)$$

where E is the ionization energy and $B(u, v) = \Gamma(u)\Gamma(v)/\Gamma(u+v)$. Atomic units are used in Eq.(1.11) (conversion factors between atomic unit and SI systems: energy, 1 au = 4.34×10^{-18} J = 27.1 eV; time, 1 au = 2.42×10^{-17} s; electric field strength, 1 au = 5.14×10^{11} V/m). The saturation intensity can be evaluated in the SI system as

$$I_s = \frac{2n_0}{Z_0} A_{0,s}^2, \quad (1.12)$$

where $Z_0 = 377\Omega$ is the impedance of free space and n_0 is the index of refraction. For near infrared laser pulses ($\lambda \sim 1 \mu\text{m}$) of tens to hundreds of picosecond time duration the saturation intensities for noble gases ($E \sim 15$ eV) are in the range $10^{13} - 10^{14}$ W/cm², in agreement with the experimental findings [50, 51, 52, 53]. As example, Eqs. (1.11) and (1.12) give a saturation intensity of 4.9×10^{13} W/cm² for an argon atom exposed to a 320 ps pulse at 780 nm. This is in good agreement with the measured saturation intensity between 3×10^{13} W/cm² and 4×10^{13} W/cm² reported in Chapter 4

(see also Figure 1.6). The smaller value of the measured saturation intensity compared to the calculated saturation intensity can be ascribed to the presence of collisions and secondary ionization in the gas jet during the 320 ps duration of the pulse.

Ionization of an atom by an intense low-frequency light field may also occur via direct tunneling of the electron through the quasi-stationary potential barrier formed by the superposition of the atomic coulomb field and laser field. A successful species-dependent model has been developed by Ammosov, Delone and Krainov [55] (ADK-model) based on a quasi-classical ac-tunneling theory. The ADK-model provides a simple and easy to compute ionization rate equation for complex atoms and ions, which describes rather well tunneling ionization by sub-ps pulses [56].

The onset of tunneling ionization can in general be described by a dimensionless adiabaticity parameter, also known as the *Keldysh parameter* [57],

$$\gamma^2 = \frac{E}{2U_e}, \quad (1.13)$$

where E is the ionization energy, and U_e is the ponderomotive (quiver) energy of an electron in the laser field, given by

$$U_e = \frac{I}{4\omega^2}. \quad (1.14)$$

Atomic units are used in Eqs. (1.13) and (1.14). In practical units, $U_e[\text{eV}] = 9.33 \times 10^{-14} I[\text{W}/\text{cm}^2] \lambda^2[\mu\text{m}^2]$. For $\gamma^2 < 1$ ionization occurs predominantly through tunneling, while for $\gamma^2 > 1$ multiphoton ionization prevails. The dominant ionization process is then determined by the atomic ionization energy as well as by the laser wavelength. For the case of noble gases, $E \sim 15$ eV, and near-infrared lasers, $\lambda \sim 1 \mu\text{m}$, $\gamma^2 \sim 1$ for $I \sim 10^{14} \text{ W}/\text{cm}^2$. This means that within the intensity range $10^{13} - 10^{14} \text{ W}/\text{cm}^2$, MPI sets in and rapidly saturates with the on-set of tunnel ionization.

The *Keldysh parameter*, however, does not take into account the time profile of the light pulse as it refers to the instantaneous light intensity. In other words, it is a good indicator of the ionization process for step-like pulses. In reality intense pulses have a time profile envelope that can usually be approximated by Gaussian or squared hyperbolic-secant functions whose rising edge does play an important role in the ionization sequence. As shown by Lambropoulos [58], multiple ionization is likely to occur on the rising edge of a strong laser pulse and consequently “an atom can not be realistically assumed to be exposed intact to laser intensities much higher than $10^{14} \text{ W}/\text{cm}^2$ ”. This is indeed the case for pulses longer than a few picoseconds [59]. For sub-100 fs pulses, which are widely available nowadays, the *Keldysh parameter* is a good indicator of the photoionization mechanism in view of the short duration of the pulse. Therefore, tunnelling ionization dominates at intensities higher than $10^{14} \text{ W}/\text{cm}^2$ for sub-100 fs pulses.

For ultra-intense femtosecond pulses, $I > 10^{15} \text{ W}/\text{cm}^2$, the electric field is strong enough to suppress the atomic potential barrier [56] and the electron can escape over the potential barrier. The barrier-suppression ionization mechanism, also called over-the-barrier ionization, will not be discussed here since it falls outside the scope of the present thesis.

1.4 High-order harmonic generation

1.4.1 The semiclassical model

Electromagnetic emission by an atom exposed to a laser field of intensity above the *perturbative regime* cannot be described in terms of the atomic polarization, and substantial ionization may occur during the laser pulse leading to a plasma formation. In a plasma ion-electron pairs give the dominant contribution to the electromagnetic emission, which comes essentially in two forms: incoherent and coherent. Bremsstrahlung radiation in a plasma generates an isotropic incoherent continuum at short wavelength ($\lambda \leq 30$ nm). Fluorescence lines due to recombination processes are also observed. This incoherent radiation can be of high brightness which makes it suitable for technical applications. For example, plasma radiation around 13 nm is considered the most promising candidate as a next generation source for optical lithography [60]. On the other end, coherent emission is made up of distinct spectral components given by high-order harmonics of the fundamental frequency and has laser-like characteristics.

The first experimental observation of high-order harmonic generation dates back to the late 80s [51, 61, 62]. Powerful near-infrared pulses of tens of ps time duration were used and harmonics up to about the 20th order were generated. With the advent of chirp-pulsed-amplification, high-order harmonic generation was investigated also with pulses of hundreds of fs time duration [63, 64] and harmonics up to $q \sim 100$ were observed. Subsequently, using intense pulses of tens of fs and sub-10-fs time duration, harmonics with order up to several hundreds were generated [65]. In all cases a very characteristic shape is found for the harmonic spectrum: the drop of the low-order harmonics is followed by a region of almost constant harmonic strength, the *plateau*, which suddenly ends at the so-called *cutoff*.

The universal and characteristic harmonic spectrum shape can be understood in terms of a semiclassical approach, the so-called *three-step model*, developed by Corkum [66] and Kulander and coworkers [67]. The physical processes of the model are schematically presented in Figure 1.5. The first step is the ionization of the atom by the intense laser pulse. Once the electron has escaped the atom harmonic generation is determined by the dynamics of the electron-ion pair in the strong oscillating electric field. The simplifying assumption of a free electron moving in the strong laser field is made, and it is generally a good approximation to treat classically the electron motion after ionization, because of the large number of photons involved in the interaction. Assuming a zero initial velocity of the expelled electron, the total kinetic energy K of the oscillatory motion of the electron in the laser field can be expressed as

$$K = 2U_e(\cos \omega t - \cos \omega t_0), \quad (1.15)$$

where U_e is the quiver energy defined in Eq. (1.14) and t_0 is the release time of the electron. The quivering electron can basically undergo two different processes depending on t_0 : it can leave the nucleus (both directly or after scattering with it), or it can be recaptured when passing by the nucleus again. The first process leads to the photoionization of the atom, while the second process is the last step of the *three-step model*: the electron undergoes laser-assisted recombination with the parent ion and a high-energy harmonic photon is emitted. For this reason the model is often called *recollision model*.

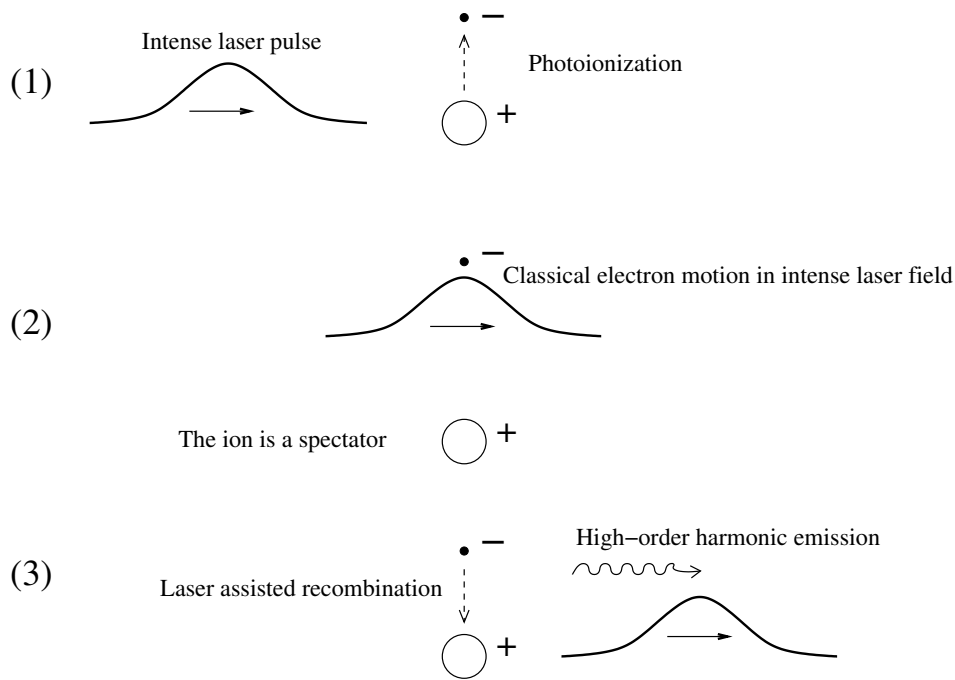


Figure 1.5. Pictorial representation of the three-step model: (1) Photoionization; (2) Classical motion of the electron in the laser field ; (3) Laser assisted recombination and subsequent emission of the harmonic radiation.

The process of ionization and recapture repeats every half optical cycle giving rise to odd harmonics. The energy of the emitted photon equals the kinetic energy of the electron plus the ionization energy of the atom. The maximum instantaneous kinetic energy of the electron at the moment of recapture, evaluated using Eq. (1.15), is $3.17U_e$ for $t_0 = 0.3T$, where T is the period of the light field. This value is in good agreement with the *cutoff* energy found in HHG experiments. The emission strength for harmonics below the cutoff energy is almost constant, generating the characteristic *plateau*.

The high-order harmonic spectrum shape has been reproduced also by theoretical calculations of the response of a single atom in an intense laser field using different approaches: non-perturbative solutions of the time-dependent Schrödinger equation [68]; approximate analytical quantum theory [69]; non-perturbative quantum electrodynamics theory [70, 71].

1.4.2 Propagation effects

None of the theoretical calculations on HHG, nor the *three-step model*, take into account the propagation effects in a multi-atom ensemble, which could influence the plateau structure and are of relevance for understanding the total harmonic yield obtained in the experiments.

Since HHG is a coherent process, the phase relation between emission generated by the atoms in different position in the medium becomes an important issue, similarly as in the LHG process. In the usual experimental conditions HHG is performed using a focused Gaussian pump beam, which interacts with an initially neutral gas that becomes rapidly photoionized by the pump pulse. In this situation there are three

relevant components of the wave vector mismatch

$$\Delta k_q \equiv qk_1 - k_q = \Delta k_q^g + \Delta k_q^a(t) + \Delta k_q^e(t), \quad (1.16)$$

where the superscripts g , a and e indicate the geometrical, atomic and electronic contribution respectively.

The time-independent geometrical wave-vector mismatch can be expressed in the following way for the two experimental situations of pump pulses focused in a gas jet (or cell) or coupled in a gas-filled hollow-core fiber [72],

$$\begin{aligned} \Delta k_q^g &= 2(1 - q)/b < 0 && \text{jet } (b \gg L), \\ \Delta k_q^g &= \frac{\lambda_1}{4\pi r^2} (u_q^2/q - qu_1^2) < 0 && \text{hollow - fiber,} \end{aligned} \quad (1.17)$$

where b is the confocal parameter of the pump beam, L is the medium length, u_1 and u_q are the propagation mode constants in the fiber for the pump and q^{th} -order harmonic respectively, and r is the fiber radius. In both cases the wave vector mismatch is negative and has the same dependence on the harmonic order, $\Delta k_q^g \propto q$ for $q \gg 1$.

The atomic contribution to the wave vector mismatch is related to the atomic dispersive contribution to the refractive index,

$$\Delta k_q^a(t) = q \frac{\omega_1}{c} (n_a(\omega_1, t) - n_a(q\omega_1, t)), \quad (1.18)$$

with $n_a(\omega, t) = n_o(\omega) + n_2(\omega)I(t)$, where n_o and n_2 are the linear and nonlinear refractive index respectively. In general, Δk_q^a is positive for $q \gg 1$ and far from atomic resonances.

If the laser intensity is sufficiently high to ionize the medium then a plasma is formed in the interaction region. The index of refraction in an ionized medium is determined by the free electrons, and, in a collisionless plasma, is given by

$$n_e(\omega, t) = [1 - (\omega_p(t)/\omega)^2]^{1/2}, \quad (1.19)$$

where $\omega_p^2(t)[\text{s}^{-2}] = e^2 N_e(t)/m_e \epsilon_0 \sim 3.18 \times 10^9 N_e[\text{cm}^{-3}]$ is the time-dependent electronic plasma frequency, which is the frequency of the collective oscillations of the electrons due to the laser radiation. Here, $N_e(t)$ is the time-dependent electron density, while e and m_e are the charge and mass of the electron. At electron densities typical in HHG experiments ($N_e(t) \ll 10^{21} \text{ cm}^{-3}$) $\omega_p \ll \omega$, for $\omega \sim 2 \times 10^{15} \text{ s}^{-1}$ ($\lambda \sim 1 \mu\text{m}$). Hence, the free electron refractive index is well approximated by

$$n_e(\omega, t) = 1 - \frac{1}{2} (\omega_p(t)/\omega)^2 < 1. \quad (1.20)$$

The corresponding time dependent wave vector mismatch, for $q \gg 1$, is given by

$$\Delta k_q^e(t) = -\frac{q\omega_p^2(t)}{2c\omega_1} < 0. \quad (1.21)$$

The ionic contribution to the refractive index, n_i , can be neglected in the phase matching evaluation because of the smaller dispersive characteristic compared to the atomic

one, $\delta_a(\omega) \gg \delta_i(\omega)$, and the ionic plasma frequency being much smaller than the electronic one ($m_i \gg m_e$).

By comparing Δk_q^g in a jet and Δk_q^e it is possible to determine the electron density above which the plasma mismatch is dominant over the geometrical mismatch. As both scale linearly with q for $q \gg 1$, this condition is independent of the harmonic order and is given by $N_e[\text{cm}^{-3}] > 7.1 \times 10^{15} (b[\text{mm}]\lambda[\mu\text{m}])^{-1}$. For $\lambda \sim 1 \mu\text{m}$ and $b \sim 10 \text{ mm}$ this density is about 10^3 times less than the typical electron density in a gas jet ionized by a pulse at the saturation intensity, $\sim 5 \times 10^{17} \text{ cm}^{-3}$, (corresponding to a fully but singly ionized gas at 15 mbar). The phase mismatch is dominated by the plasma dispersion for even moderate levels of ionization.

Theoretical analysis of the phase matching influence on HHG is difficult to perform due to the time-dependent nature of the atomic and electronic contributions. However, by invoking simple assumptions based on phenomenological characteristics of the HHG process it is possible to estimate the phase matching effect. Systematic investigations on HHG as a function of the pump pulse intensity reveal a common behavior for the high-order harmonics [63, 73]: after a fast increase in the *cutoff* region, all the harmonics in the *plateau* exhibit a power dependence with a similar exponent factor p , followed by much lower increase when ionization of the medium becomes substantial, i.e., at the saturation intensity. Typically, $5 < p < 8$ for the *plateau* harmonics [74] and $11 < p < 13$ in the *cutoff* region [75]. This behavior is shown in Figure 1.6, for the 11th and 15th harmonic generated in argon using the powerful laser system described in Chapter 4. The total photoelectron yield is also reported, and shows a saturation intensity between $3 \times 10^{13} \text{ W/cm}^2$ and $4 \times 10^{13} \text{ W/cm}^2$. At intensities smaller than I_s the 11th harmonic is well into the *plateau* and its intensity dependence is described by a power law with $p = 7$, while for the 15th harmonic, which is still in the *cutoff* region even at the saturation intensity, the exponent is $p = 11$.

Based on this typical power law intensity dependence of the plateau harmonics it is possible analytically to find an approximate solution for the propagation equation of the generated harmonics [76]. Using this model and assuming only geometrical and atomic contributions to the wave vector mismatch (neglecting the nonlinear refractive index) it can be shown that phase matching for plateau harmonics is almost independent of the harmonic order [77, 78].

At intensities higher than I_s the deleterious effect of substantial ionization on high-order harmonic generation is two-fold. First, the depletion of neutral atoms leads to a decrease in the harmonic production; an ionized medium will produce harmonics but with a much lower efficiency due to the smaller polarizability of ions. Secondly, the wave vector mismatch introduced by the free electrons dominates the other terms, even when a low degree of ionization is present, degrading the phase matching. The actual effect of substantial ionization is presented in Figure 1.6, where the much lower increase of harmonic yield with laser intensity after the saturation intensity is evident.

Another important propagation effect in HHG is the spectral distortion of the harmonics, which originates from the self-phase modulation (SPM) of the pump beam due to the time-dependent refractive index of the medium. By definition, the harmonic frequency is given by the central frequency of the frequency distribution of the pump pulse multiplied by the harmonic order. However, the intense pump pulse undergoes SFM during the propagation in the ionizing gaseous medium. As a consequence,

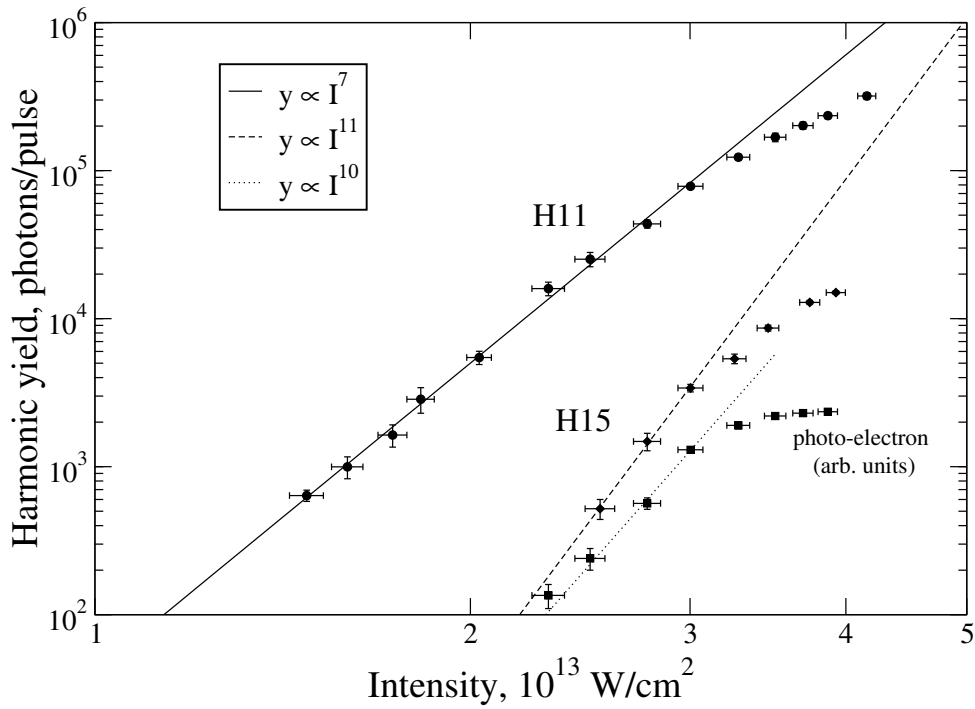


Figure 1.6. Intensity dependence of the 11th and 15th harmonics generated in argon gas jet with a pump pulse of 300 ps at 780nm (see Chapter 4). The photoelectron yield measurements indicates multiphoton ionization, $\propto I^n$ with $n=10$ (10 photons at 780nm are needed to ionize argon), with a saturation intensity between $3 \times 10^{13} \text{ W/cm}^2$ and $4 \times 10^{13} \text{ W/cm}^2$. Power law least-square fits on the harmonic data points for intensities below the saturation intensity give exponent 7 and 11 for the 11th and 15th harmonic respectively.

the frequency of the generating radiation may differ from the central frequency of the incoming pump pulse. Specifically, the frequency shift of an electromagnetic wave propagating in a medium of length L with a time-dependent index of refraction $n(t, z)$ is given by

$$\Delta\omega(t) \equiv \omega(t) - \omega_0 = -\frac{\omega_0}{c} \int^L \frac{\partial n(t, z)}{\partial t} dz = -\frac{\omega_0 L}{c} \frac{\partial n(t)}{\partial t}, \quad (1.22)$$

where, ω_0 is the original frequency of the incoming pump pulse, c is the speed of light in vacuum and the expression on the right-hand side is valid for a homogeneous medium. In an ionizing medium the major contribution to SPM is given by the time-dependent index of refraction of the plasma given by Eq. (1.20). Assuming a homogeneous plasma of length L , the frequency shift is given by

$$\Delta\omega_e(t) = \frac{Le^2}{2c\omega_0 m_e \epsilon_0} \frac{\partial N_e(t)}{\partial t}. \quad (1.23)$$

In HHG the strongest harmonic emission is achieved during the ionization of the neutral atoms (the first step of the *recollision model*). Accordingly to Eq. (1.23), the pump pulse undergoes a positive frequency shift (*blueshift*) which induces a shift of $q \times \Delta\omega_e(t)$ in the generated harmonic of order q . The frequency shift of the harmonic

radiation itself while propagating in the ionizing medium is negligible, since it is q^2 times smaller than $q \times \Delta\omega_e(t)$.

Other sources of shift in the harmonic frequency are the SPM of the pump beam due to the intensity-dependent refractive index of the neutral atoms and the so-called *dynamically induced chirp* associated with the recollision nature of HHG (see Ref. [79] and references therein). Both generate a frequency shift proportional to the variation in time of the pump pulse intensity, thus the shorter the pulse duration the larger the induced frequency excursion. A careful investigation and assessment of the frequency chirp of the high-order harmonics is important especially when the generated XUV radiation has to be used for accurate frequency-domain spectroscopy.

1.4.3 Generation of tunable coherent XUV radiation

The intrinsic coherence of the high-order harmonic generation process gives unique properties to the produced XUV radiation: its spatial, temporal and spectral characteristics follow those of the pump laser pulse. As a consequence, the XUV radiation is collimated, with a high degree of spatial coherence; a short pump pulse produces an even shorter harmonic pulse; a narrow bandwidth pump pulse produces a narrow-band harmonic pulse. Moreover, the harmonic pulse can be easily synchronized with auxiliary laser pulses to perform pump/probe experiments, and a tunable pump pulse produces tunable harmonics. These properties make HHG an ideal XUV source for high resolution spectroscopy both in the time and frequency domain.

In the following a brief review is given of works reported in the literature concerning the use of HHG as a source of radiation for spectroscopic applications. Particular attention is given to the reported values of the spectral purity ($\lambda/\Delta\lambda$) and on the tunability characteristics.

Femtosecond lasers A systematic study of the spectral bandwidth of high-order harmonics produced with a 70 fs Ti:Sapphire laser is reported in Ref. [80]. The bandwidth is found to increase from 0.11 eV, for the 7th harmonic, to 0.37 eV, for the 45th harmonic, in a gradual manner, and then to level-off at a value of 0.43 eV for the higher orders (47th-55th). The corresponding spectral purity is $\lambda/\Delta\lambda \sim 1 - 2 \times 10^2$. The tunability of the Ti:Sapphire laser (790-800 nm) allows also a short range tunability of the harmonics [81]. Tunable high-order harmonics for surface science applications from a 120 fs Ti:Sapphire laser (780-800 nm) are reported in Ref. [82], but no mention is made about the harmonic bandwidth. Measurements of the spectral shape for the 27th harmonic of a fixed frequency 140 fs Cr:LiSrAlF₆ laser results in a 0.1 nm bandwidth corresponding to a spectral purity of $\lambda/\Delta\lambda \sim 3 \times 10^2$ [83]. In Ref. [84] tunable high-order harmonics are produced using 100 fs pulses from a Ti:Sapphire amplified laser (780-820 nm). A bandwidth of the 9th harmonic of tens of meV is claimed corresponding to a spectral purity of $\lambda/\Delta\lambda \sim 3 \times 10^2$. The same source is used to demonstrate Ramsey-type spectroscopy in krypton with high-order harmonics (9th at 88 nm) produced by two identical but delayed pump pulses [85]. In this way the limitation of the large harmonic bandwidth, due to the short pulse duration, is overcome. This technique builds upon the pioneering studies on time-domain spectroscopy by Salour and Cohen-Tannoudji [86] and by Teets *et al.* [87], demonstrating the use of multiple laser pulses in controlled

sequence for high-resolution spectroscopic studies (a detailed description of Ramsey-type optical spectroscopy techniques is given by Salour in Ref. [88]). In Ramsey-type spectroscopy the final resolution is determined by both the phase stability and the time delay of the two “identical” exciting pulses. Recently, great effort is put in producing phase stabilized energetic femtosecond pulses, which would produce phase-locked time-delayed harmonics to be used in XUV Ramsey spectroscopy [89].

High-order frequency mixing Tunable XUV radiation can also be produced via high-order frequency mixing. In Ref. [90] sum and difference frequency mixing is performed between fixed frequency (790 nm) energetic pulses of 150 fs time duration and less energetic tunable (470-600 nm) pulses from an optical parametric generator. As a result tunable XUV radiation is obtained with an efficiency one order of magnitude lower than by the one-color HHG process. Continuously tunable XUV radiation is also reported in Ref. [91] mixing high-power fixed-frequency radiation (813 nm) and tunable (520-650 nm) radiation from an optical parametric generator (OPG). Mixing processes involving two OPG photons are also observed.

Optical-Parametric-Amplifiers Another way to produce tunable high-order harmonics is to use tunable pump pulses from an optical-parametric-amplifier (OPA). In Ref. [92] harmonics from a tunable OPA (1200-1550 nm) are produced up to 9th order. Due to the low energy of the pump pulses the wavelength range of the produced harmonics is limited. High-order harmonics from a tunable OPA (1100-1600nm) are reported in Ref. [93]. The short pulse duration (30fs), necessary to reach the high intensity for HHG is reflected in a broad spectral bandwidth.

Frequency shifting of the harmonics The high-order harmonics of very short laser pulses (≤ 30 fs) can be frequency shifted by controlling the harmonic generation process itself. Shift of the pump pulse frequency and thus of the generated harmonics can be achieved by controlling the free-electron density in the generating medium. A blue shift is expected due to the increase in the free-electron density during the rising edge of the pump pulse. Tunable harmonics of a 30 fs pump pulses are obtained by changing the gas jet position relative to the laser beam focus [94, 95]. In this way the effective laser intensity experienced by the gas is changed and thus the ionization rate is controlled. A tunability of few tens of nanometer is demonstrated for radiation around 10 nm, although at the expense of spectral purity. Tunable high-order harmonics of a 26 fs pump pulse are reported in Ref. [96]. Controlling energy and chirp of the pump pulses continuous, tunability of radiation around 10 nm, maintaining a constant spectral purity of $\lambda/\Delta\lambda \sim 1 \times 10^2$, is achieved. This is obtained because of an interplay of plasma blueshifting and chirp of the fundamental pulse during the HHG process with ultra short pulses.

Picosecond lasers High-order harmonic generation with a tunable (570-640 nm) 1 ps pump laser is reported in Ref. [83]. A bandwidth of 0.026 nm is reported for the 7th harmonic, corresponding to a spectral purity of $\lambda/\Delta\lambda \sim 3 \times 10^3$. A noticeable example of

Table 1.1. Comparison of performances between narrow-band XUV sources: HHG with 300 ps pulses (*Pico*) vs. state-of-the-art from synchrotron radiation (Super ACO, SU5 beam-line).

	<i>Pico</i>	Super ACO, SU5
Spectral Purity ($\lambda/\Delta\lambda$),		
@ 87nm - @ 52nm	2.8×10^5	$2.1 \times 10^5 - 1.2 \times 10^5$
Avg. photon flux (ph./s) ²	$\sim 10^5$	$\sim 10^9$ @ $\lambda/\Delta\lambda = 5 \times 10^4$
Repetition rate	10 Hz	8-100 MHz
Photons per pulse ²	$\sim 10^4$	10-100
Pulse duration	≤ 100 ps	~ 650 ps
Peak photon flux (ph./s) ²	$\geq 10^{15}$	$10^{10} - 10^{11}$
Dimensions	table-top	exp. hall + synchrotron

HHG with tunable picosecond pulses is the 70 ps laser system at the Lund Laser Center. The laser system, described in Ref. [97], consists of a distributed-feedback dye laser producing tunable pulses (700-900 nm) that are subsequently amplified in two dye-cells and a Ti:Sapphire crystal. This source was used in time-resolved spectroscopy to measure the lifetime of the $1s2p \ ^1P$ state of helium at 58.4 nm using a pump/probe technique [98]. The 13^{th} harmonic generated in krypton was used as the pump pulse, while the probe pulse was a UV pulse at 355 nm. The measured spectral bandwidth of the harmonic is 0.01 nm, corresponding to a spectral purity of $\lambda/\Delta\lambda \sim 2 \times 10^4$. This enables an excellent selectivity in the excitation process. Recently [99] a similar measurement is reported for the $1s3p \ ^1P$ state of helium at 53.7 nm using the 14^{th} harmonic generated by wave-mixing of fundamental and second harmonic in krypton. The Lund laser system is also used for time resolved photoionization spectroscopy in molecules [100] and absolute photoionization cross sections measurements [101].

Despite the fast technological advances in HHG, synchrotrons remain the “classical” sources of XUV radiation for many applications. This is due to their high brightness as well as reliable and well established operations, especially for the so-called “third generation synchrotrons” employing undulators and wigglers. However, for the specific case of narrow-band tunable XUV radiation, laser sources based on HHG are nowadays challenging the most advanced synchrotron sources. The state-of-the-art synchrotron-based narrow-band XUV source is the SU5 beamline at Super-ACO in Orsay (France) [102]. Spectral selection of the continuum synchrotron radiation is obtained by means high-resolution long focal length optics (toroidal mirrors and a spherical monochromator) resulting in a spectral purity of $\lambda/\Delta\lambda = 1.2 \times 10^5$ around 52 nm. In the future the high-resolution SU5 beamline will be transferred to the new third generation synchrotron SOLEIL [103] where a factor of 10 more XUV/VUV photons are expected to be produced maintaining the same spectral purity.

A new laser based narrow-band tunable XUV source is presented in Part II of the present thesis. This source, denominated *Pico*, is based on HHG with 300 ps near-infrared pulses. Anticipating the results that will be discussed in Chapter 5, Table 1.1 shows a comparison between the performances of *Pico* and the SU5 beamline. It has

²Available in the target region, i.e. after monochromators.

to be noted that the pulse duration of the XUV radiation generated by *Pico* is not measured. However, it is well established that the harmonic pulses are shorter than the pump pulses, and the 100 ps time duration reported in Table 1.1 is only an estimate of the upper limit. Actually, XUV pulses of tens of picoseconds can be obtained especially for the higher order harmonics. As can be seen from Table 1.1, *Pico* has excellent performances in terms of spectral purity, $\lambda/\Delta\lambda = 2.8 \times 10^5$, more than a factor two better to what is achieved at synchrotrons. As for the photon flux, the peak value for *Pico* is higher than that of the synchrotron source. Increase of the harmonic yield in the *Pico* may be pursued using a wave-mixing scheme [104] and/or gas-filled hollow fibers [4].

Part I

LHG applied to high-resolution VUV spectroscopy

Chapter 2

High-resolution photoionization spectroscopy of xenon

High-resolution spectroscopy of xenon is performed on four transitions from the $5p^6 1S_0$ ground state to the $5d'[3/2]_1$, $8d[1/2]_1$, $8d[3/2]_1$ and $7s'[1/2]_1$ excited states (jl -coupling notation) by means of 1VUV+1UV photoionization spectroscopy. Spectra of all nine stable isotopes are resolved enabling the determination of the hyperfine splittings and isotope shifts. Magnetic dipole (for both ^{129}Xe and ^{131}Xe) and electric quadrupole (for ^{131}Xe) hyperfine splitting constants are derived for all four excited states. Mass and field shift contributions to the isotope shifts are separated using King plots relative to existing accurate isotope shift values. A high field shift factor, even for the transitions in which no s -electron is involved, is deduced. From precise calibration of the transition frequencies an accurate value for the ionization energy of ^{136}Xe , $E_{3/2}^{136} = 97833.805(11) \text{ cm}^{-1}$, is derived. In addition values of the ionization energies for all other isotopes are determined.

(This Chapter corresponds to Ref. [105]: Phys. Rev A, **64** (2001) 032505.)

2.1 Introduction

High-resolution laser spectroscopy involving the ground state of noble gases requires a tunable narrow-band light source in the vacuum-ultraviolet (VUV) range because of the large energy gap to the excited states. Nowadays, the use of pulsed-dye-amplification of a tunable cw laser light source, followed by non-linear up-conversion processes, allows for the production of coherent VUV light. Such a source, in combination with the technique of 1VUV+1UV photoionization, has already been applied to spectroscopic investigations of the noble gases He, Ne, Ar and Kr [28, 34, 106, 107], in which Isotope Shifts (IS) and Hyperfine Splittings (HFS) could be measured. For He and Ar new and accurate values of the ionization energy have been deduced from these measurements. For the heaviest stable noble gas, xenon, accurate values for the VUV transitions from the ground state are missing, hence the ionization energy is less accurately known.

Here the results of high-resolution 1VUV+1UV photoionization spectroscopy in Xe are presented. Four transitions from the ground state $5p^6$ to the excited states $5d'[3/2]_1$, $8d[1/2]_1$, $8d[3/2]_1$ and $7s'[1/2]_1$ (jl -coupling notation) at 106.8, 106.1, 105.6 and 104.4 nm respectively, are investigated. Natural xenon contains nine stable isotopes with

abundances: ^{124}Xe (0.0096%), ^{126}Xe (0.009%), ^{128}Xe (1.92%), ^{129}Xe (26.4%), ^{130}Xe (4.1%), ^{131}Xe (21.1%), ^{132}Xe (26.9%), ^{134}Xe (10.4%) and ^{136}Xe (8.9%). Our setup allows to spectrally resolve all isotopes and to measure the IS in the investigated transitions. The two odd isotopes possess non-zero nuclear spin ($I^{129} = 1/2$, $I^{131} = 3/2$), inducing hyperfine splitting of the $J=1$ excited states. The hyperfine structures are fully resolved and HFS constants determined.

The investigation of the IS of heavy elements can provide insight in the electronic density at the nucleus. Previous IS measurements in a two-photon transition from the ground state of xenon [108] seem to indicate a large screening effect by the p -electrons in the closed shell.

Absolute transition frequencies are measured using a calibration procedure based on saturation spectroscopy of molecular iodine and use of an actively stabilized Fabry-Pérot interferometer. This work connects, by means of accurate frequency measurements, the energy of the ground state to the entire manifold of electronically excited states; transitions between those excited states, and their position with respect to the ionization limit, have been studied elsewhere with high accuracy. The combination of the present and existing data results in an accurate determination of isotope-dependent ionization energies in xenon.

2.2 Experiment

The experimental apparatus to generate wavelength-tunable VUV pulses is presented in detail elsewhere [107] (see also Figure 1.4); here only a brief description will be given. cw light from a tunable ring-dye-laser (Spectra Physics 380), running on DCM dye and pumped with the second harmonic of a cw Nd:YAG laser (Millennia, Spectra Physics), is amplified in a three-stage Pulse-Dye-Amplifier (PDA). The PDA, which also operates on DCM dye and is pumped by the second harmonic of an injection-seeded Q-switched Nd:YAG laser, delivers pulses with a repetition rate of 10 Hz, duration of 5 ns and energy up to 60 mJ. These pulses are then frequency doubled in a KD*P crystal, producing pulses of 8 mJ in the UV, and subsequently focused in a Xenon gas jet for third harmonic generation.

The overlapping UV and VUV light beams intersect at 90° a collimated Xenon atomic beam in the interaction region, where a $1\text{VUV}+1\text{UV}$ photoionization process is induced. On resonance the time-of-flight mass spectrometer collects the ions to be detected on an electron multiplier. The signal from each isotope is recorded with different boxcar integrators, whose gates are set at appropriate time windows. The signal-to-noise ratio is sufficient to reveal also the less abundant ^{124}Xe and ^{126}Xe isotopes, except for the case of the weakest transition to the $8d[1/2]_1$ excited state.

The absolute frequency of the cw light is calibrated by simultaneous recording of a saturated absorption spectrum of molecular iodine. The “t” hyperfine components of the I_2 lines, recently calibrated with 1 MHz accuracy (1σ) in the 595-655 nm wavelength range [109], are used as a reference. Calibration of the VUV light is accomplished taking into account the factor of 6 due to the frequency doubling and tripling. The centre frequency of the pulsed output of the PDA may undergo, because of chirp, a small net shift with respect to the seeding cw light, used for calibration. This issue, including its effect in the harmonic frequencies, has been extensively discussed elsewhere [33, 34].

From such studies it is estimated that the uncertainty in the absolute VUV frequency is less than 0.003 cm^{-1} . The chirp phenomenon does not affect the results of relative frequency measurements, such as isotope shifts and hyperfine splittings.

In addition, the transmission peaks of a Fabry-Pérot interferometer (FPI) are also recorded, in order to obtain accurate frequency markers for the cw light. The FPI is locked to a frequency-stabilized He-Ne laser, and its free spectral range of $148.9563(3)$ MHz is calibrated against the known “t” hyperfine component of two I_2 lines (P65(7-4) and P95(7-4) [109]). The FPI fringes are then translated into VUV frequency markers with a spacing of $893.7378(18)$ MHz. Spectra of the Xenon resonances, the I_2 reference spectrum and the FPI markers are stored in a computer for further analysis. The width of the xenon lines is typically 400 MHz (FWHM) in a Gaussian profile, mainly arising from the bandwidth of the VUV light and a small Doppler contribution in the crossed-beam configuration.

2.3 Results and Discussion

The four transitions investigated are indicated by their excited state configurations, namely $5d'[3/2]_1$, $8d[1/2]_1$, $8d[3/2]_1$ and $7s'[1/2]_1$. Isotopically and hyperfine resolved spectra of these states in excitation from the ground state are recorded. An example of the experimental results is given in Figure 2.1, where spectra recorded for all nine isotopes in the $7s'[1/2]_1$ transition are shown. The different noise levels in the spectra reflect the relative natural abundance of the isotopes. Since only four boxcars are used not all the isotopic lines can be measured simultaneously; hence one isotopic signal is chosen as reference and recorded in each scan to facilitate the data analysis. Figure 2.1 contains the results of three different scans, which are put together on the same frequency scale making use of the signal from the reference isotope. The FPI marks are also shown and the frequency scale is given in VUV frequency. It has to be noted that the weak peak present in the ^{130}Xe spectrum is an artefact, associated with the resonance of the highly abundant ^{129}Xe . To perform the absolute frequency calibration a long scan is usually needed to bridge the gap between the Xenon line and the nearest I_2 line. In the case of the $7s'[1/2]_1$ the gap toward the R95(10-4) line is ~ 20 GHz. In the following sections the results of the measurements are presented and discussed.

2.3.1 Hyperfine Splitting

Hyperfine splitting in an atomic energy level is due to the interaction of the magnetic and electric multipole-moments of the nucleus with the electrons and exists only for electronic configurations with angular momentum $J \neq 0$. The strongest effects arise from interactions with the magnetic dipole and the electric quadrupole moments of the nuclear charge distribution, the latter being present only for nuclear spin $I > 1/2$. When these two contributions are considered, the HFS between two adjacent hyperfine components is given by [110]

$$\Delta_{F,F-1} = AF + \frac{3}{2}BF \frac{F^2 + \frac{1}{2} - I(I+1) - J(J+1)}{I(2I-1)J(2J-1)}, \quad (2.1)$$

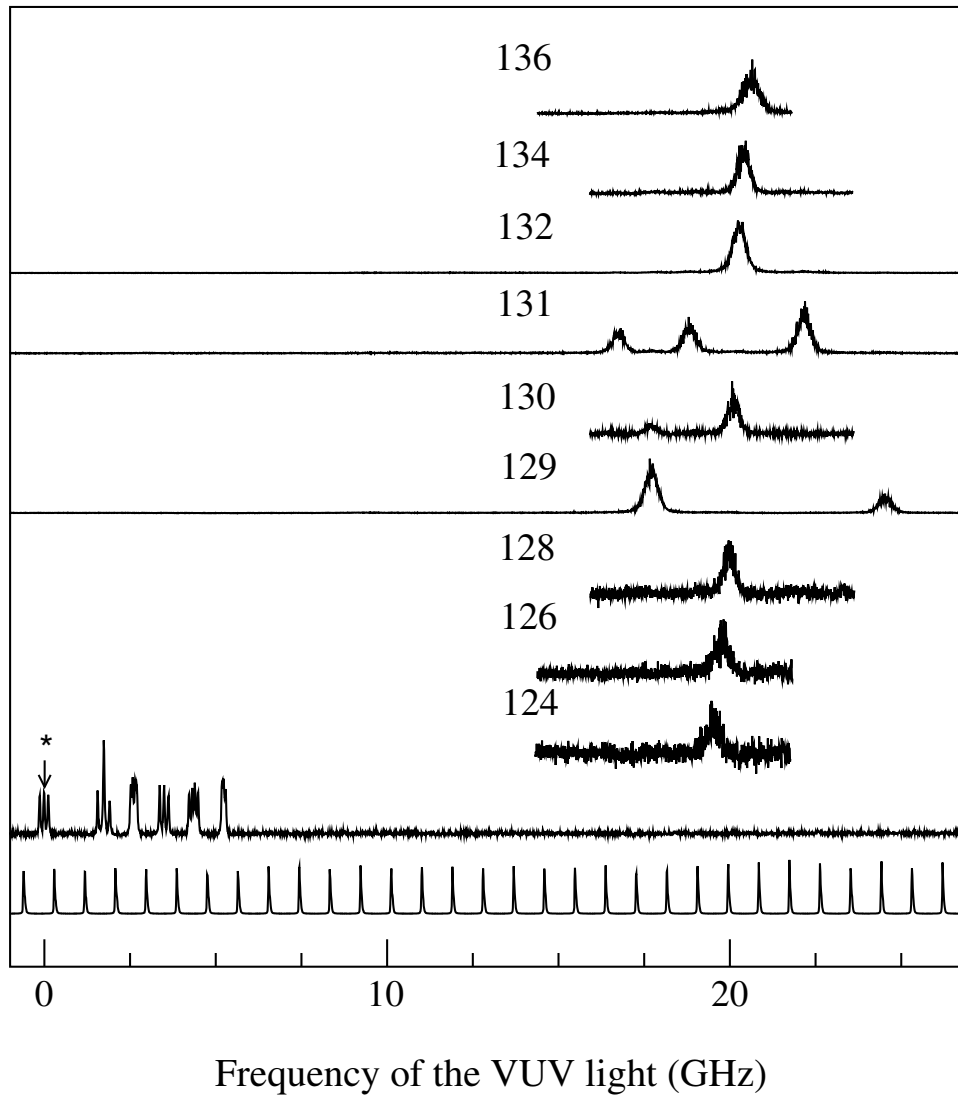


Figure 2.1. Spectra of the $(5p^6 - 7s'[1/2]_1)$ transition, for all natural isotopes of Xenon indicated by their mass number; FPI transmission peaks, from which the frequency scale has been deduced are also shown; the zero frequency has been set at the "t" hyperfine component of the R95(10-4) I_2 line (denoted by *) used for absolute frequency calibration; this zero is in fact at 2872009.06 GHz.

where F is the total angular momentum of the atom and A , B are the magnetic dipole and electric quadrupole hyperfine constants respectively. Since ground states of noble gases have $J = 0$, measured splittings directly reflect the HFS of the excited state.

The measured hyperfine splittings are presented in Table 2.1. They are averaged over 4 to 12 spectra, depending on the number of scans recorded for each individual line, while the quoted uncertainties represent the standard deviation. The individual hyperfine components are identified on the basis of the intensity rule [110], i.e. higher intensity for larger F values. From the HFS reported in Table 2.1 and using Eq. (2.1), it is possible to derive the hyperfine constants A and B , also included in Table 2.1. In the ^{129}Xe isotope there is no quadrupole term since $I^{129} = 1/2$.

Table 2.1. Results of hyperfine splitting measurements. All values are given in MHz, reported uncertainties are 1σ .

	$5d'[3/2]_1$	$8d[1/2]_1$	$8d[3/2]_1$	$7s'[1/2]_1$
$\Delta_{5/2,3/2}^{131}$	-1200(18)	328(19)	-625(30)	3336(9)
$\Delta_{3/2,1/2}^{131}$	-797(23)	398(14)	-467(20)	2063(17)
A^{131}	-493(7)	165(10)	-265(10)	1345(4)
B^{131}	26(8)	-67(6)	31(9)	-20(6)
$\Delta_{3/2,1/2}^{129}$	2486(18)	-869(9)	1369(34)	-6822(23)
A^{129}	1657(12)	-579(6)	913(23)	-4548(15)

A consistency check for the HFS measurements involves evaluation of the ratio A^{129}/A^{131} . The magnetic dipole constant A is proportional to the ratio of the nuclear magnetic moment μ and the nuclear spin, hence $A^{129}/A^{131} = \frac{\mu^{129}I^{131}}{\mu^{131}I^{129}}$. Using $\mu^{129} = -0.7768\mu_N$ and $\mu^{131} = 0.6908\mu_N$ (μ_N is the nuclear magneton) this ratio becomes $A^{129}/A^{131} = -3.373$. The values of A^{129} and A^{131} reported in Table 2.1 show that, within the error margins, the experimental ratio A^{129}/A^{131} is compatible with this value.

2.3.2 Isotope Shift

The IS of an atomic transition contains two different contributions. One is related to the finite mass of the nucleus and is commonly referred to as the Mass Shift (MS), while the other is due to the non-zero size of the nucleus and is called the Field Shift (FS) [111]. The latter is predominant in heavy elements ($Z > 60$), while the former prevails in light elements ($Z < 30$). For a medium-weight element like xenon both effects give a significant contribution.

Formally the isotope shift in an atomic transition i is the difference between the transition frequency ν_i of two isotopes with mass numbers A' and A , $\Delta_i^{A',A} = \nu_i^{A'} - \nu_i^A$. It can be expressed as [112]

$$\Delta_i^{A',A} = \Delta_{MS,i}^{A',A} + \Delta_{FS,i}^{A',A} = M_i \frac{A' - A}{AA'} + F_i \lambda^{A',A}. \quad (2.2)$$

The mass shift factor is conventionally separated into two terms, $M_i = M_{N,i} + M_{S,i}$. The first term describes the so-called normal mass shift (N), which represents the contribution of the reduced mass of the electron in the atomic system and is given to a good approximation by $\frac{m_e}{m_u} \nu_i$, where m_e , m_u are the electron mass and atomic mass unit respectively. The second term describes the specific mass shift (S) which arises from the correlated electron momenta. Its evaluation requires complicated many body atomic structure calculations.

The field shift factor F_i is proportional to the change in the total electron density at the nucleus when the atom undergoes the atomic transition i , while the nuclear parameters $\lambda^{A',A}$ is given, to a good approximation, by the change in the mean-square nuclear charge radius between isotopes.

Table 2.2. Results of isotope shift measurements, $\Delta_i^{136,A} = \nu_i^{136} - \nu_i^A$ (in MHz). Reported uncertainties are 1σ .

A	$5d'[3/2]_1$	$8d[1/2]_1$	$8d[3/2]_1$	$7s'[1/2]_1$
134	203(10)	207(12)	219(15)	213(12)
132	351(18)	384(18)	354(20)	365(18)
131	470(11)	531(23)	545(17)	492(20)
130	509(13)	557(11)	529(30)	523(24)
129	591(19)	675(14)	684(27)	678(24)
128	667(12)	747(19)	726(20)	692(22)
126	821(14)		912(20)	869(25)
124	1008(20)		1116(20)	1069(22)

The measured IS's are presented in Table 2.2. The heaviest ^{136}Xe isotope is chosen as a reference to express the isotope shifts. The reported values are averaged over 4 to 18 measurements depending on the number of scans recorded for each isotope, while errors are 1σ . In the weaker $8d[1/2]_1$ transition the two less abundant ^{126}Xe and ^{124}Xe isotopes are not observed.

For the two odd isotopes the IS's are evaluated from the centre of gravity of the measured HFS. According to the "odd-even staggering" phenomenon they do not lie midway between the two neighbouring even isotopes, but closer to the lighter one [113]. This is graphically shown in Figure 2.2, where the measured $\Delta_{8d[3/2]_1}^{136,A}$ and $\Delta_{7s'[1/2]_1}^{136,A}$ are plotted against the atomic mass number A . Figure 2.2 also shows the anomaly for ^{136}Xe , related to the neutron shell closing at $N=82$. These effects reflect the behaviour of the change in the mean-square nuclear charge radius between isotopes. In our analysis attention will be focused on an interpretation of the IS with the aim to extract information on the electronic structure of the atom. This implies that all the information on the nuclear charge distribution, contained in the nuclear parameters $\lambda^{A',A}$, will be divided out, leaving only the effect of the electronic structure, contained in the M_i and F_i factors.

In order to extract physical information from the measured IS's we perform the well known King plot analysis [111]. To do so we introduce the so-called "modified IS" defined as $\Delta_i^{A',A}$ divided by the atomic mass factor $(A' - A)/AA'$. Then, when two transition i, j are considered, it follows from Eq. (2.2) that the respective modified IS's obey the following linear relation

$$\Delta_i^{A',A} \frac{AA'}{A' - A} = \left(\frac{F_i}{F_j} \right) \Delta_j^{A',A} \frac{AA'}{A' - A} + \left(M_i - \frac{F_i}{F_j} M_j \right). \quad (2.3)$$

When the modified IS's of the two transitions, belonging to the same isotope pair, are plotted one against the other (King plot) the slope S and intercept P deduced from a linear least-square fit give respectively $S = (F_i/F_j)$ and $P = (M_i - (F_i/F_j)M_j)$. It is worth to notice that if $\Delta_j^{A',A}$ are known then, through Eq. (2.3), it is possible to evaluate

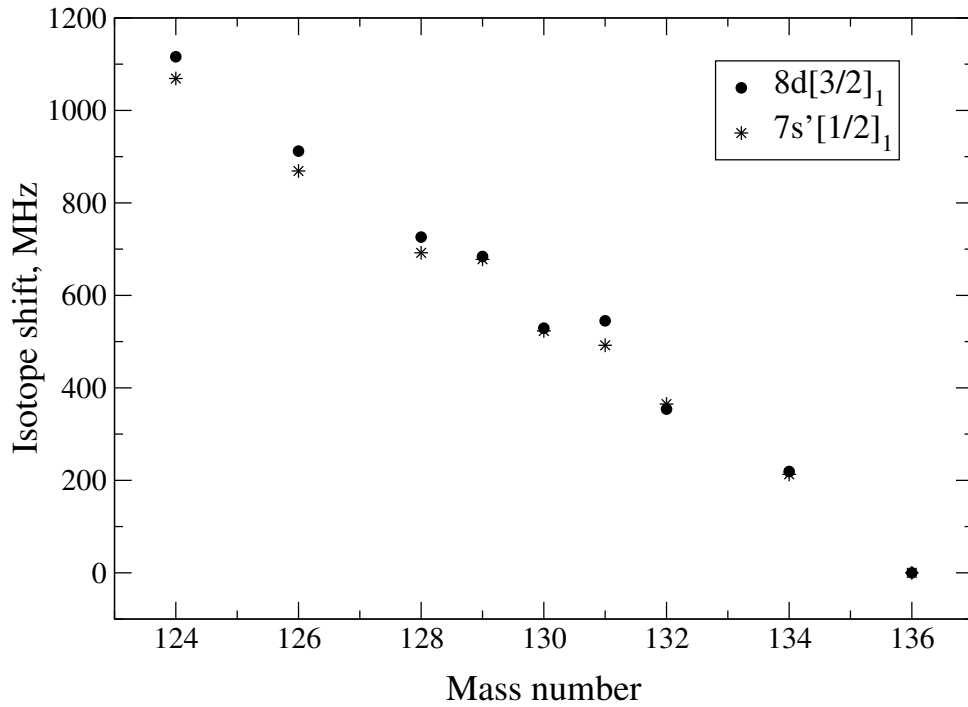


Figure 2.2. Measured isotope shift as function of the mass number, for the $8d[3/2]_1$ and $7s'[1/2]_1$ transitions. The experimental uncertainty is about 20 MHz.

$\Delta_i^{A',A}$ for all isotope pairs once they are known at least for two isotope pairs.

To take the maximum advantage from our data we perform King plots relative to the modified IS's in the $(6s[3/2]_2 - 7p[5/2]_3)$ transition at 467nm ($j=467$) measured by Schneider [114]. These data are very accurate, with an uncertainty less than 1 MHz, and cover all the natural isotopes of xenon. As an example, in Figure 2.3 the "modified $\Delta_{7s'[1/2]_1}^{136,A}$ vs modified $\Delta_{467}^{136,A}$ " plot is shown along with the straight line resulting from a weighted linear least-square fit in which the statistical errors on our data are used as weight. Such a fit is performed for every transition and the results are presented in the first two rows of Table 2.3 where the reported uncertainty arises from the fit procedure.

From King plots absolute values of the isotope shift factors can not be extracted unless they are known for one of the transitions, see Eq. (2.3). The main result of our IS measurements follows from the relative F_i/F_{467} values obtained; a high value for the field shift factors is deduced even for those transition in which no s -electron is involved. This is consistent with the result of the first IS measurement in a transition involving the ground state of Xenon as performed by Plimmer *et al.* [108]. They measured the IS in the two-photon transition between the ground state and the $6p[1/2]_0$ excited state, and deduced a value for $F_{6p[1/2]_0}/F_{467}$ of -1.207(11). This effect is ascribed to an increase in the electron density at the nucleus that results from the removal of a $5p$ -electron from the closed shell configuration, thereby strongly decreasing the screening of the inner s -electrons.

In order to give an estimate of the F_i and M_i factors for the investigated transitions we use the values of the isotope shift factors given by Schneider for the 467nm transition [114] (see also Ref. [115]). The F_{467} factor is evaluated using the relation

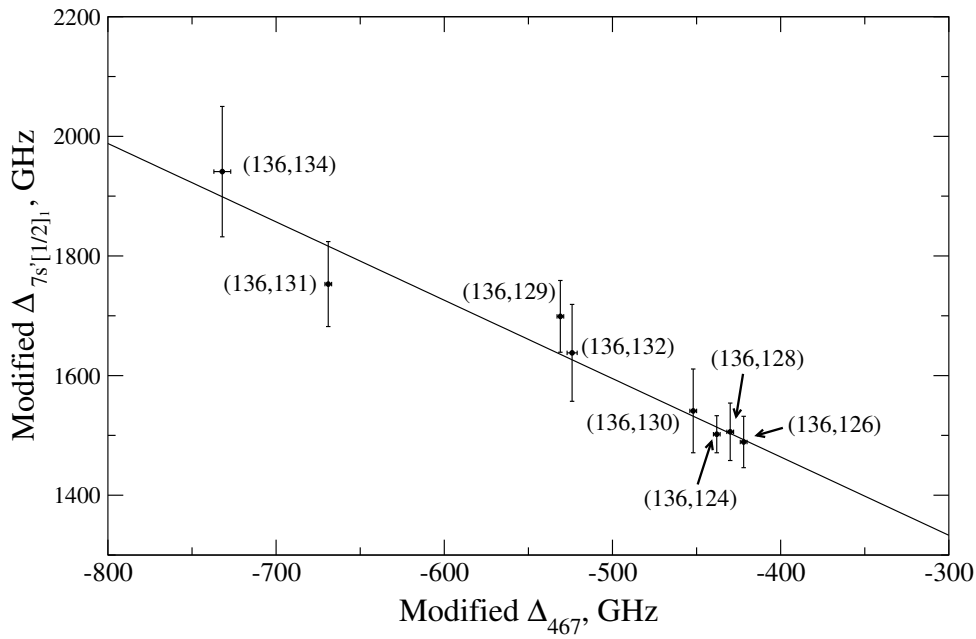


Figure 2.3. King plot between $\Delta_{7s'[1/2]_1}^{136,A}$, measured in the present work, and $\Delta_{467}^{136,A}$, reported in [114]. The isotope pair is specified for each point; the straight line is the result of a weighted linear least-squares fit.

Table 2.3. Result of King plots: $S_i = F_i/F_{467}$ and $P_i = M_i - (F_i/F_{467})M_{467}$; the absolute values of F_i and M_i are obtained using the estimate $F_{467} = 2.06 \text{ GHz fm}^{-2}$ and $M_{467} = -158(91) \text{ GHz}$ reported in [114].

	$5d'[3/2]_1$	$8d[1/2]_1$	$8d[3/2]_1$	$7s'[1/2]_1$
S_i	-1.12(15)	-0.94(26)	-1.48(23)	-1.31(23)
P_i (GHz)	950(71)	1211(130)	927(107)	940(112)
F_i (GHz fm ⁻²)	2.31(32)	1.94(54)	3.05(47)	2.70(47)
M_i (GHz)	1127(126)	1360(161)	1161(176)	1147(168)

$F_{(ns-n'p)} = \frac{\pi a_0^3}{Z} |\Psi(0)|_{ns}^2 \cdot \beta \cdot f(Z)$ [111], where a_0 is the Bohr radius, $|\Psi(0)|_{ns}^2$ the non-relativistic ns -electron density at the nucleus, β the screening factor, for which a value 1.16 follows from an Hartree-Fock calculation on the $6s$ configuration, and $f(Z)$ the relativistic correction ($f(54)=11.37 \text{ GHz fm}^{-2}$). The quantity $\frac{\pi a_0^3}{Z} |\Psi(0)|_{ns}^2$ is estimated with two methods involving both the Goudsmit-Fermi-Segrè formula and the magnetic hyperfine splitting constant, from which $F_{467} = 2.06 \text{ GHz fm}^{-2}$ is deduced. Based on empirical methods, in particular related to critically evaluated data on the Ba chain, Schneider estimates the specific mass shift to be $-56(10) \text{ MHz}$ for the (136,134) isotope pair, from which $M_{467} = -158(91) \text{ GHz}$ is obtained. An estimate for the absolute values of F_i and M_i factors pertaining to the four transitions investigated here, are given in the last two rows of Table 2.3. However it has to be pointed out that in general there is not a unique and reliable estimate for the specific mass shift (see [112, 115]), conse-

Table 2.4. Absolute calibration of transition frequencies from the ground state (values in cm^{-1}). The first and second rows denote the reference Xe isotope and the I_2 reference line. ν^{I_2} is the frequency of the “t” hyperfine component of this I_2 line, $\Delta\nu^{A_{ref},I_2}$ the measured frequency difference between the reference xenon isotope line and this “t” component in the VUV frequency scale, $\nu^{A_{ref}}$ is the absolute frequency of the Xenon line for the reference isotope. In the last row values from Yoshino and Freeman [116] are given.

	$8d[1/2]_1$	$8d[3/2]_1$	$7s'[1/2]_1$
A_{ref}	136	136	132
I_2	P30(7-4)	P68(8-4)	R95(10-4)
ν^{I_2}	15704.88007(3)	15780.92844(3)	15966.65174(3)
$\Delta\nu^{A_{ref},I_2}$	-1.2617(12)	-0.08839(57)	0.67629(61)
$\nu^{A_{ref}}$	94228.0187(32)	94685.4822(30)	95800.5867(30)
From [116]	94228.02(20)	94685.47(20)	95800.70(20)

quently the value of M_{467} , and those of M_i reported in Table 2.3, have to be interpreted with caution. In contrast the values obtained for the F_i factors are fairly reliable since the method used to evaluate the field shift factor for $(ns - n'p)$ transitions is generally accepted.

2.3.3 Absolute Calibration

Absolute calibration of the resonance frequency is performed on three transitions, $8d[1/2]_1$, $8d[3/2]_1$, $7s'[1/2]_1$, for which the results are reported in Table 2.4. The frequencies of the “t” hyperfine component of the I_2 lines, ν^{I_2} , are taken from the new atlas of reference lines [109]. The measured values for the frequency difference between the reference Xe isotope line and the “t” component of the I_2 calibration line, $\Delta\nu^{A_{ref},I_2}$, are given on a VUV frequency scale (see Figure 2.1). These are averaged values from 5 to 8 measurements, depending on the number of spectra recorded; the uncertainties represent 1σ . The absolute frequency for the reference Xe isotope line is obtained as $\nu^{A_{ref}} = \Delta\nu^{A_{ref},I_2} + 6 \times \nu^{I_2}$, where the factor 6 reflects the fact that the I_2 saturated absorption lines are measured with the fundamental frequency. The uncertainty in $\nu^{A_{ref}}$ is due to the experimental errors in $\Delta\nu^{A_{ref},I_2}$ plus a possible contribution due to frequency chirp arising in the PDA. This is estimated to be less than 0.003 cm^{-1} [33, 34] and is the main source of error in the absolute calibration. Previous results from classical absorption spectroscopy [116] are reported for comparison in the last row of Table 2.4. However, here no isotope is specified since the individual isotope lines were not resolved. The present results are fully consistent with previous data and increase the accuracy by almost two orders of magnitude.

From the absolute calibration of the $8d[1/2]_1$ transition it is possible to derive a new and more accurate value of the ionization energy of ^{136}Xe . Knight and Wang [117] performed laser spectroscopy of the $nf[3/2]_1$ ($n > 24$) Rydberg series in Xe, resulting in an ionization limit of $21637.02(1) \text{ cm}^{-1}$ from the $6s'[1/2]_0$ level. A value of the ionization energy of $E_{3/2} = 97833.81(10) \text{ cm}^{-1}$ was reported as well, based on the value of the

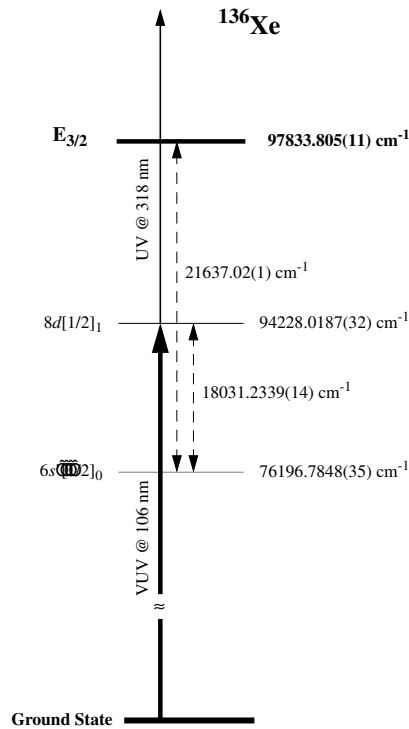


Figure 2.4. Schematic of the energy levels involved in the evaluation of the ionization energy of ^{136}Xe ; the continuous arrows represent the VUV and UV photons used in the spectroscopic measurements reported in this work, from which the energy of the $8d[1/2]_1$ level has been determined; the dashed arrows indicate the energy separations reported in the literature: first the energy separation between the $6s'[1/2]_0$ and $8d[1/2]_1$ levels from Ref. [118] is used to evaluate the energy of the $6s'[1/2]_0$ level and then the ionization energy is estimated using the ionization limit from the $6s'[1/2]_0$ level reported in Ref. [117].

energy of the $6s'[1/2]_0$ level of $76196.79(10) \text{ cm}^{-1}$. However, from the high precision interferometric measurements on enriched ^{136}Xe sample by Humphreys and Paul [118], an energy separation between $6s'[1/2]_0$ and $8d[1/2]_1$ levels of $18031.2339(14) \text{ cm}^{-1}$ can be deduced. This value, combined with the absolute calibration of the energy of the $8d[1/2]_1$ level in ^{136}Xe , gives an energy of the $6s'[1/2]_0$ level of $76196.7848(35) \text{ cm}^{-1}$. Finally, a value for the ionization energy for ^{136}Xe of $E_{3/2}^{136} = 97833.805(11) \text{ cm}^{-1}$ results. The energy levels involved in the evaluation of the ionization energy are schematically shown in Figure 2.4.

It has to be pointed out that in the experiment of Knight and Wang [117] isotopic lines were not resolved, so that, to validate the present result, an estimate has to be given of the IS in the transitions measured. Using the results reported by Jackson and Coulombe [119] of $\Delta_{(6s'[1/2]_0-5f[3/2]_1)}^{136,130} = -84(9) \text{ MHz}$, an upper limit of 0.003 cm^{-1} for the IS between ^{136}Xe and ^{130}Xe in the transitions studied in Ref. [117] can be estimated. This shift does not affect the result on the ionization energy of ^{136}Xe at the present level of accuracy.

Another relevant fact that can be deduced from data reported in the literature is

Table 2.5. Summary of the isotope-dependent ionization energies $E_{3/2}^A$. The first column gives the ionization energy of ^{136}Xe ($E_{3/2}^{136}$) in cm^{-1} , with uncertainty of 0.011cm^{-1} , while the others give the $\Delta_{(GS-6s'[1/2]_0)}^{136,A}$ (in 10^{-3}cm^{-1}). From these data the isotope-dependent ionization energies can be evaluated as $E_{3/2}^A = E_{3/2}^{136} - \Delta_{(GS-6s'[1/2]_0)}^{136,A}$.

$E_{3/2}^{136}$	134	132	131	130	129	128	126	124
97833.805	9.0	15.0	21.7	21.2	27.2	28.4	35.5	44.0

the IS between the ground state (GS) and the $6s'[1/2]_0$ excited state, from which an estimate of the isotope-dependent ionization energies can be derived. To do so the following identity is used:

$$\Delta_{(GS-6s'[1/2]_0)}^{A',A} = \Delta_{(GS-6p[1/2]_0)}^{A',A} - \Delta_{(6s[3/2]_1-6p[1/2]_0)}^{A',A} + \Delta_{(6s[3/2]_1-6s'[1/2]_0)}^{A',A}. \quad (2.4)$$

The values of the first term on the right hand side are given by Plimmer *et al.* [108], while for the second term values were measured by Jackson and Coulombe [120]. To evaluate the third term, values reported also in Ref. [120] for the *IS*'s in ($6s'[1/2]_0 - 7p[3/2]_1$), ($6s[3/2]_1 - 7p[3/2]_1$), ($6s'[1/2]_0 - 6p'[3/2]_1$) and ($6s[3/2]_1 - 6p'[3/2]_1$) transitions are used to derive two sets of values for $\Delta_{(6s[3/2]_1-6s'[1/2]_0)}^{A',A}$. These are consistent within the error margins and the weighted mean is assumed. However, no direct evaluation of the IS in the ($GS - 6s'[1/2]_0$) transition is possible for ^{124}Xe , ^{126}Xe , ^{129}Xe and ^{131}Xe , since no measurements were reported for these isotopes in Ref. [120]. Nevertheless a King plot with respect to the 467nm transition allows to evaluate $\Delta_{(GS-6s'[1/2]_0)}^{A',A}$ also for these isotopes.

A summary of the results on the isotope-dependent ionization energies is given in Table 2.5. In the first column the ionization energy of ^{136}Xe is reported. In the others the evaluated $\Delta_{(GS-6s'[1/2]_0)}^{136,A}$ are given in units of 10^{-3}cm^{-1} , with uncertainty of $0.4 \times 10^{-3} \text{cm}^{-1}$. If the isotope shifts in the ($6s'[1/2]_0 - nf[3/2]_1$) transitions are considered (see above), the $\Delta_{(GS-6s'[1/2]_0)}^{136,A}$ values give an estimate of the ionization energy differences with an accuracy of about 0.003cm^{-1} . In view of this, the isotope-dependent ionization energies can be estimated as, $E_{3/2}^A = E_{3/2}^{136} - \Delta_{(GS-6s'[1/2]_0)}^{136,A}$.

2.4 Conclusions

In this Chapter, results of high-resolution VUV-laser spectroscopy of xenon are presented. Tunable narrow-band VUV pulses near 105nm wavelength are used to investigate transitions from the ground state to four excited states, $5d'[3/2]_1$, $8d[1/2]_1$, $8d[3/2]_1$ and $7s'[1/2]_1$ by two-step ionization spectroscopy. A time-of-flight mass spectrometer allows to resolve the transitions of all nine stable isotopes; isotope shifts and hyperfine splittings can be measured. Values for the hyperfine splitting constants are derived for the ^{129}Xe and ^{131}Xe isotopes. Using King plots field shift and mass shift

contributions are separated. The field factor turns out to be high, even when no s -electron is involved in the transition. This result confirms observations made by Plimmer *et al.* [108], that the removal of a p -electron from the ground state's closed shell configuration strongly increases the electronic density at the nucleus.

For three of the transitions an absolute frequency calibration is also performed. This results in a two orders of magnitude higher accuracy for the absolute energies of the investigated levels compared with previous measurements. A new value for the ionization energy of ^{136}Xe is derived with an accuracy of about one order of magnitude better than the previous value. Finally, using isotope shift measurements reported in literature, isotope-dependent ionization energies for all Xe isotopes are derived for the first time.

Chapter 3

High-resolution photoionization spectroscopy of krypton

Accurate spectroscopy of krypton is performed on five transitions from the $(4p^6) \ ^1S_0$ ground state to the $5d[1/2]_1$, $6s[3/2]_1$, $5p[1/2]_0$, $5p[3/2]_2$ and $5p[5/2]_2$ excited states (jl -coupling notation) by means of 1VUV+1UV and 2UV+1UV resonance enhanced photoionization. Isotope shifts of all six stable isotopes are determined, and a King plot analysis indicates a large field shift factor even for transitions in which no s electron is involved. Absolute frequency calibration is performed on three transitions, leading to a novel determination of the excited state energies of Kr with an accuracy of $\sim 0.0013 \text{ cm}^{-1}$. A value for the ionization energy of ^{86}Kr , $112914.516(14) \text{ cm}^{-1}$, is derived along with ionization energies for all even isotopes³. The ac Stark effect on the two-photon transition to the $5p[1/2]_0$ excited state is investigated. For light intensities up to $\sim 260 \text{ MW/cm}^2$ a linear shift of $0.75(48) \text{ Hz(W/cm}^2)^{-1}$ is observed, while at higher intensities the line exhibits a sub-linear shift and an asymmetric broadening. Consequences of the results obtained for the $5p[1/2]_0$ state on resonance-enhanced narrow-band XUV/VUV generation are discussed.

(This Chapter corresponds to Ref. [121]:J. Phys. B, **35** (2002) 1071. Figure 3.1 and Section 3.5 have been added.)

3.1 Introduction

The level structure of the noble gas atoms displays manifolds of relatively closely packed electronically excited states separated by 10 eV or more from a single electronic ground state (1S_0), without any fine or hyperfine structure. Optical spectroscopy, with classical methods, and laser spectroscopy, using the presence of one or more metastable levels, has allowed for precision experiments within the excited state manifolds. The ionization energies, with respect to the lowest lying excited states, were accurately determined through extrapolation of the Rydberg series; as examples we refer to laser spectroscopic work on the Rydberg series in krypton by Yoon and Glab [122] and in xenon by Knight and Wang [117]. Thus, a single accurate measurement of a transition frequency involving the 1S_0 ground state, yields a value of the ionization energy of the atom. However, a complication is the production and calibration

³A more recent and accurate determination of the ionization energy of krypton is discussed in Section 3.5.

of narrow-band radiation at the wavelengths required, which all fall in the vacuum-ultraviolet (VUV) and extreme-ultraviolet (XUV) domain. Such studies have recently been performed on noble gas atoms using XUV/VUV laser sources based on nonlinear up-conversion of wavelength-tunable and narrow-band laser pulses in the visible range.

Eikema *et al.* [34, 123] performed photoionization spectroscopy on the ($1^1S - 2^1P$) transition in He at 58 nm, measuring the ^3He - ^4He isotope shift (IS), the ac Stark shift and determining an accurate value of the transition frequency. From this value the ground state Lamb shift and an improved value of the ionization energy were obtained. A similar study on the two lowest resonance lines in neon near 74 nm was performed as well [106]. Velchev *et al.* [107] measured IS's and the absolute frequency of the ($3p^6 - 3p^54s'[1/2]_1$) transition in Ar, also leading to an improved value for the ionization energy. Trickl *et al.* [28] performed high-resolution photoionization spectroscopy of Kr in transitions from the ground state to several *ns* Rydberg levels. Transition frequencies, IS's, hyperfine splittings (HFS's) and lifetimes were measured, and accurate values for the excited state energies were deduced. In Chapter 2 measurement of IS's, HFS's and transition frequencies of 4 transitions in Xe in the VUV range are reported, from which isotope dependent ionization energies were derived. King plot analysis [111] on the IS data revealed a large field shift factor, i.e. a big increase in the electron density at the nucleus during the transition; this phenomenon was ascribed to the removal of a *p* electron from the closed shell ground state configuration. In the case of xenon it was demonstrated by Plimmer *et al.* [108] that the energy gap between the ground state and the manifold of electronically excited states could be bridged in two-photon excitation using cw-lasers; in the latter study no absolute calibration was performed of the transition frequency.

In this Chapter we report on 1VUV+1UV and 2UV+1UV photoionization spectroscopy on 5 transitions from the ground state of krypton. One-photon excitation is performed to the $5d[1/2]_1$ and $6s[3/2]_1$ excited states (*jl*-coupling notation) while $5p[1/2]_0$, $5p[3/2]_2$ and $5p[5/2]_2$ levels are investigated with two-photon excitation. Natural Kr gas is composed of six isotopes: ^{78}Kr (0.35%), ^{80}Kr (2.3%), ^{82}Kr (11.6%), ^{83}Kr (11.5%), ^{84}Kr (57.0%) and ^{86}Kr (17.3%). The odd ^{83}Kr is the only isotope with non-zero nuclear spin ($I=9/2$), inducing a hyperfine structure on lines involving states with non-zero electronic angular momentum. Isotope shifts are measured for all transitions and a King plot analysis indicates the effect of a large field shift factor, as in the case of xenon. Accurate absolute energies are determined for the $5d[1/2]_1$, $6s[3/2]_1$ and $5p[1/2]_0$ excited states, leading to a determination of excited state energies of krypton at the 40 MHz accuracy level. This result, combined with data reported in the literature, enables us to estimate the ionization energies for all even isotopes.

Accurate spectroscopy of the $5p[1/2]_0$ excited state is of particular interest, since the two-photon ($4p^6 - 4p^55p[1/2]_0$) transition at 212.55 nm has been found to be very efficient for the production of XUV and VUV tunable radiation via resonance enhanced third-harmonic generation and sum/difference frequency mixing in a Kr jet [42, 43]. Using this resonance-enhanced sum-frequency mixing scheme Balakrishnan *et al.* [45] produced tunable XUV-radiation, which was applied in a determination of the dissociation energy of the hydrogen molecule. Hollenstein *et al.* [46] built a tunable XUV laser source with a 0.008 cm^{-1} bandwidth based on this krypton resonance. Here we

report on the ac Stark effect of the $(4p^6 - 4p^55p[1/2]_0)$ transition. Results show a linear shift of the line at low light intensity and a sub-linear shift with asymmetric line profile at high intensity. The accurate analysis of the intensity effects on the transition frequency in this two-photon resonance bears relevance for the studies in which the tunable XUV/VUV output radiation is used in precision spectroscopy.

3.2 Experimental setup and procedure

3.2.1 1VUV+1UV photoionization spectroscopy

The experimental apparatus used to perform 1VUV+1UV photoionization spectroscopy is discussed elsewhere [105, 107] (see also Figure 1.4); here only a brief description is given. The primary light source is a cw-tunable ring-dye-laser (Spectra Physics 380) running on Rhodamine (Rh) 6G dye and pumped by a 5W frequency-doubled diode-pumped Nd:YVO₄ laser (Spectra Physics Millennia). The cw visible light is coupled into a single-mode polarization-maintaining fibre, whose output (typically 250 mW) seeds a pulsed-dye-amplifier (PDA). The PDA contains three amplifier stages pumped by the second harmonic of an injection-seeded Q-switched Nd:YAG laser (Quanta Ray, GCR-5), running at 10Hz repetition rate, and delivering a maximum of 770 mJ/pulse at 532 nm. The 5 ns pulses from the PDA are frequency doubled in a KD*P crystal to generate UV radiation. The UV pulses (up to 30 mJ) are subsequently focused by a 25 cm focal length lens in a xenon gas jet where VUV coherent radiation is produced via third-harmonic generation. In a differentially-pumped chamber the overlapping VUV and UV beams perpendicularly intersect a collimated Kr atomic beam. The ions produced by resonant 1VUV+1UV photoionization are detected by an electron multiplier. A time-of-flight mass spectrometer is used to separate the signals for different isotopes, which are collected with boxcar integrators with gates set at the appropriate time windows. The recorded spectra are stored in a computer for further analysis. The wavelengths of the visible and VUV radiation needed to excite the $5d[1/2]_1$ and $6s[3/2]_1$ states are collected in Table 3.1, where the dyes used in the laser system are also included. Absolute frequencies in the VUV range are calibrated by performing metrology on the cw-seed input of the PDA, using a molecular iodine (I₂) saturation setup, and a temperature and pressure stabilized confocal Fabry-Pérot interferometer (FPI). The “t” hyperfine components of I₂ lines have been recently calibrated in the 571-655 nm wavelength range [109, 124] with 1 MHz accuracy (at 1σ), and give a very dense reference grid. The free spectral range (FSR) of the FPI, determined using the “t” component of the P(11) 16-1 and R(18) 16-1 I₂ lines as references, is 148.858(26) MHz with observed day-to-day variation that falls within the experimental error margin. The FPI transmission peaks are recorded during the scans, giving accurate frequency markers for the VUV radiation.

The VUV frequency scale is based on the metrology in the visible range after multiplication by a factor of 6. However, due to chirp effects in the amplification process, the center frequency of the pulsed output of the PDA may undergo a small net shift with respect to the seeding cw light. This issue has been the subject of several studies [125, 126, 127]. The origin of chirp is time-dependent gain in the amplification process, and its magnitude depends upon the dye used and the wavelength with respect to the

Table 3.1. Summary of experimental conditions; λ_{vis} and $\lambda_{VUV/UV}$ denote the wavelength of the primary cw visible and VUV or UV exciting radiation respectively (depending on the photoionization scheme used); in the last column the dyes used in the laser systems are reported.

photoionization scheme	excited state	λ_{vis} (nm)	$\lambda_{VUV/UV}$ (nm)	Dyes: Ring - PDA
1VUV+1UV	$5d[1/2]_1$	578.0	96.3	Rh 6G - Rh B
	$6s[3/2]_1$	600.6	100.1	Rh 6G - Rh 101
2UV+1UV	$5p[1/2]_0$	637.8	212.6	DCM - DCM
	$5p[3/2]_2$	644.4	214.8	DCM - DCM
	$5p[5/2]_2$	650.1	216.7	DCM - DCM

maximum of the dye curve. In high-precision pulsed spectroscopy the chirp effect is the main source of systematic error, typically 0.003 cm^{-1} , and techniques have been developed to overcome it. Eyler *et al.* [33] performed precision 2UV+1UV photoionization spectroscopy of the ($EF \leftarrow X$) transition in H_2 , reducing the chirp shift below the 10 MHz level using a particular mix of DCM and Rh 610 dyes. This technique, however, is applicable only to the very special case in which the transition to be investigated lies in a wavelength range where opposite chirp effects cancel the overall shift. Eikema *et al.* [34] developed a technique to actively compensate the chirp effect by applying a phase modulation on the seeding light at the input of the PDA. They were able to significantly reduce the chirp shift, leaving a residual effect on the resonance position below the 10 MHz level. The PDA used in the present experiment is the same as the one used by Eikema *et al.* [34], but without the anti-chirp compensation part.

3.2.2 2UV+1UV photoionization spectroscopy

2UV+1UV photoionization spectroscopy is performed using the same experimental apparatus as described in the previous section. The wavelengths needed to perform two-photon excitations and the used dyes are also reported in Table 3.1.

Tunable UV radiation around 215 nm is generated by tripling the visible output of the PDA, typically 60 mJ/pulse at full pump power. The schematic of the frequency tripling unit is shown in Figure 3.1. First type-I second harmonic generation is performed in a KD*P crystal, then sum-frequency mixing between fundamental and second harmonic beams takes place in a BBO crystal cut for type-I mixing. A zero-order half-wave plate, with axis set at 45° with respect to the vertical axes, is used to rotate by 90° the polarization of the visible radiation leaving the polarization of the second harmonic unchanged (in fact rotated by 180°). In this way type-I mixing takes place in the BBO crystal, and third harmonic radiation is generated. The third-harmonic radiation is separated from the fundamental and the second harmonic using two dichroic mirrors, leaving 1 mJ/pulse useful energy in the UV.

In this experiment the UV beam, with or without focusing by a lens, intersects the Kr atomic beam in the interaction chamber and a two-photon resonant three-photon ionization process takes place. In the spectroscopic measurement involving

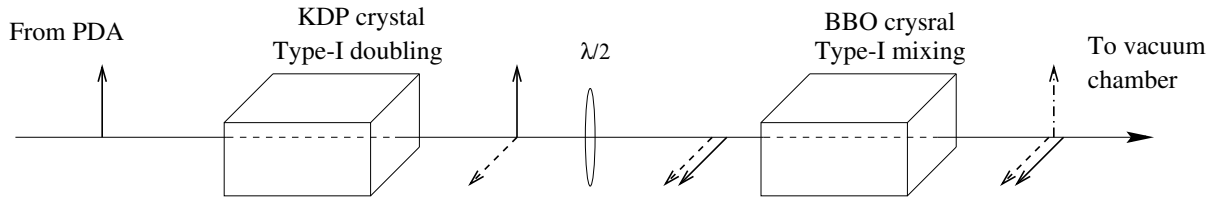


Figure 3.1. Schematic of the frequency tripling unit. The arrows represent the different wavelength polarization directions: continuous, fundamental; striped, 2nd harmonic; dotted/striped, 3rd harmonic.

two-photon excitation the UV-pulses are used in an unfocused geometry. Only for the measurements of the ac Stark effect a 1 meter focusing lens is used to increase the power density in the interaction region.

3.3 Experimental results and discussion

The five investigated transitions are denoted by their excited state configurations, namely $5d[1/2]_1$, $6s[3/2]_1$, $5p[1/2]_0$, $5p[3/2]_2$ and $5p[5/2]_2$. Typical experimental results are presented in Figure 3.2, where recorded spectra of the $5p[5/2]_2$ two-photon excitation and $5d[1/2]_1$ one-photon excitation are shown. Since three boxcars are used several scans are needed to cover the entire manifold of stable isotopes. The spectrum of the most abundant ^{84}Kr is recorded in every scan as a reference, and is used to put all the isotopic spectra on the same scale. The attainable signal-to-noise ratio allows for the observation of even the less abundant ^{78}Kr and ^{80}Kr isotopes. The etalon markers, and I_2 hyperfine line used for absolute frequency calibration of the $5d[1/2]_1$ transition, are also shown. The horizontal axis represents the actual transition frequency, i.e. VUV and 2UV frequency for one-photon and two-photon excitation respectively, while the origin is set at the second etalon fringe.

The recorded lines are fitted with a gaussian profile and the resulting full-widths at half maximum (FWHM) are ~ 400 MHz and ~ 350 MHz for 1VUV+1UV and 2UV+1UV photoionization experiments respectively. The line-widths predominantly reflect the band-width of the exciting radiation. The residual Doppler effect gives a minor contribution in the crossed beam configuration.

3.3.1 Isotope Shift

The isotope shift in an atomic transition i is defined as $\Delta_i^{A',A} = \nu_i^{A'} - \nu_i^A$, where ν_i^A denotes the transition frequency of the isotope with mass number A . For isotopes with nonzero nuclear spin I and atomic levels with nonzero angular momentum J , hyperfine splittings have to be considered. In the present experiment spectral lines of krypton are studied, pertaining to transitions from the ground state, which has $J = 0$. The hyperfine components directly reflect the excited state hyperfine structure, with states of different total angular momentum F . In this case the frequency shift between the line of an isotope of atomic mass number A' with zero nuclear spin, and the “ F ”

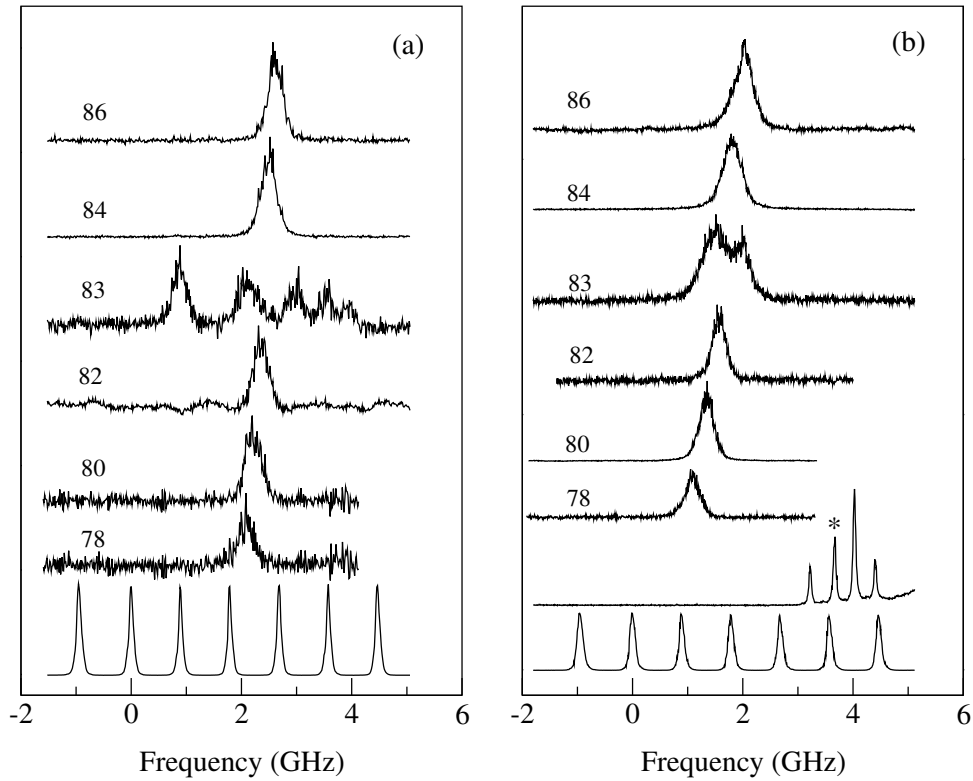


Figure 3.2. Photoionization spectra of Kr resonances for all stable isotopes: (a) two-photon excitation of the $5p[5/2]_2$ state with UV radiation at 216.7 nm in an unfocused geometry; the five hyperfine components of ^{83}Kr are resolved, with their F -value decreasing (from $13/2$ to $5/2$) with increasing frequency. (b) one-photon excitation of the $5d[1/2]_1$ state with VUV radiation at 96.3 nm; the three hyperfine components of ^{83}Kr are not resolved in this transition. In both graphs the etalon markers are scaled to the actual excitation energy; in (b) also the I_2 -saturation spectrum of the $P(11)16-1$ line is shown, with the “t” hyperfine component denoted by (*). The spurious weak modulation present in the ^{82}Kr -trace in graph (a) is noise introduced by the boxcar.

hyperfine component of an isotope with atomic mass number A and $I \neq 0$, is given by

$$\Delta_{i,F}^{A',A} = \nu_i^{A'} - \nu_i^A - \mathcal{A} \frac{C}{2} - \mathcal{B} \frac{\frac{3}{4}C(C+1) - I(I+1)J(J+1)}{2I(2I-1)J(2J-1)}, \quad (3.1)$$

where \mathcal{A} and \mathcal{B} are the magnetic dipole and electric quadrupole HFS constants of the excited state respectively, and $C = F(F+1) - I(I+1) - J(J+1)$. ν_i^A represents the transition frequency to the center of gravity of the hyperfine structure.

The measured isotope shifts relative to ^{84}Kr are presented in Table 3.2 for all five transitions. The values reported are averaged over several scans; the uncertainty is the standard deviation. For the isotope ^{83}Kr , with nonzero nuclear spin ($I=9/2$), the IS is evaluated relative to the center of gravity of the hyperfine structure. In the $5p[1/2]_0$ transition no HFS is present since $J = 0$, and $\Delta_i^{84,83}$ is measured directly. The individual hyperfine components are identified on the basis of the intensity rule [110], i.e. higher line intensity for larger F values. Due to laser band-width the resolution is

Table 3.2. Summary of results on IS measurements, $\Delta_i^{84,A} = \nu_i^{84} - \nu_i^A$ (in MHz); reported uncertainties are 1σ ; the claimed uncertainty in the values from [28, 128] is about 6 MHz.

transition	86	83	82	80	78
$5d[1/2]_1$	-206(15)		226(10)	475(15)	709(15)
from [128]	-207				
$6s[3/2]_1$	-112(15)	91(14)	157(10)	284(15)	425(15)
from [28]	-132	21	116	230	384
$5p[1/2]_0$	-138(15)	88(17)	138(17)	311(16)	426(15)
from [128]	-141		150	306	445
$5p[3/2]_2$	-130(15)	83(16)	148(13)	295(14)	435(17)
from [128]	-132		147	294	438
$5p[5/2]_2$	-123(15)	95(15)	150(13)	303(15)	430(15)
from [128]	-132		141	291	429

not always sufficient to resolve the hyperfine structure completely, and typically only the strongest component with the highest F value is fully resolved. For the $5d[1/2]_1$ transition not a single hyperfine component is resolved (see Figure 3.2(b)); moreover, signal from the ^{82}Kr isotope leaks into the mass-83 channel, obscuring the hyperfine components further. For example, the high-frequency tail of the $F=11/2$ component in Figure 3.2(a), corresponds to the ^{82}Kr line. For the $5p[3/2]_2$ and $6s[3/2]_1$ transitions $\Delta_i^{84,83}$ is evaluated via Eq. (3.1) using the measured $\Delta_{5p[3/2]_2,13/2}^{84,83} = 1083(14)$ MHz and $\Delta_{6s[3/2]_1,11/2}^{84,83} = 786(10)$ MHz, in combination with hyperfine constants reported in the literature [28, 129]. Only for the $5p[5/2]_2$ transition the hyperfine structure is sufficiently resolved to enable an evaluation of the hyperfine constants (see Figure 3.2(a)). A least-squares fit applied to Eq. (3.1) using measured values for $\Delta_{5p[5/2]_2,F}^{84,83}$ ($F = 13/2, 9/2, 7/2, 5/2$), gives $\mathcal{A} = -155.6(1.2)$ MHz and $\mathcal{B} = -428(25)$ MHz, which are compatible with the values $\mathcal{A} = -156.49(8)$ MHz and $\mathcal{B} = -407.7(13)$ MHz reported in reference [129].

Isotope shift data reported in the literature are also presented in Table 3.2 for comparison. The present results are compatible with the values reported by Kaufman [128], who systematically analyzed isotope shift data of krypton from interferometrically measured lines, and included some values of Trickl *et al.* [28]. For the $6s[3/2]_1$ transition there is a discrepancy between our results and those of Ref. [28], especially for the ^{83}Kr isotope. To underline the consistency of our results it has to be noted that the latter data for the $6s[3/2]_1$ transition were not included in the analysis of Kaufman [128].

The isotope shift of an atomic transition has two contributions, the mass shift, due to the finite mass of the nucleus, and the field shift, which arises from the nonzero volume of the nucleus [111]. The latter is predominant in heavy elements, while the former prevails in light elements. Formally the IS in a transition i can be expressed as [112]

$$\Delta_i^{A',A} = \Delta_{MS,i}^{A',A} + \Delta_{FS,i}^{A',A} = M_i \frac{A' - A}{AA'} + F_i \lambda^{A',A}, \quad (3.2)$$

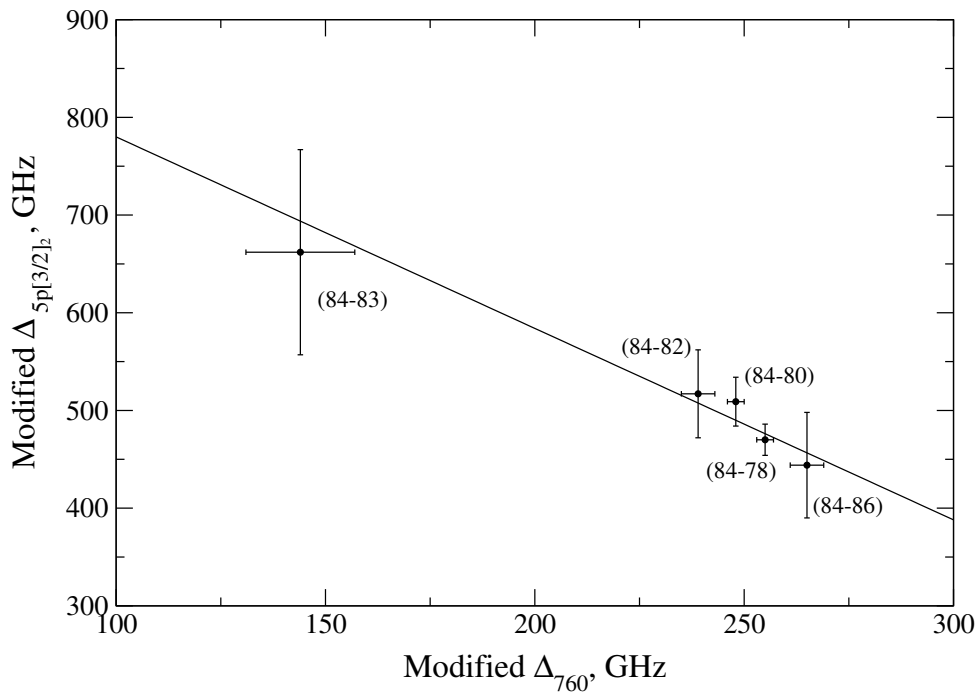


Figure 3.3. King plot of the IS in the $5p[5/2]_2$ transition, as measured in the present experiment, versus the IS in the $(5s[3/2]_2 - 5p[3/2]_2)$ transition at 760 nm [129]; the isotope pair is specified for each point and the straight line is the result of a weighted linear least-squares fit.

where M_i and F_i are the so-called mass and field shift factors respectively, and the nuclear parameters $\lambda^{A',A}$ represent, to a good approximation, changes in mean-square nuclear charge radii between isotopes. The field shift factor is proportional to the change in the total electron density at the nucleus, and can be calculated using two different semi-empirical approaches based on the magnetic hyperfine structure and the Goudsmit-Fermi-Segrè formula [110], respectively. Evaluation of the mass shift factor requires complicated many body atomic structure calculations; alternatively an estimate can be given by a combined analysis with muonic isotope shift data.

To extract physical information on the electronic structure of the atom from the present isotope shift measurements, the so-called King plot analysis is performed [105, 111]. To do so the “modified IS”, defined as $\Delta_i^{A',A} \times AA' / (A' - A)$, is introduced. When the modified IS of two transitions (i, j) are plotted against each other (King plot) the points lie in a straight line, with a slope equal to the ratio of the field shift factors, (F_i/F_j) , and an intercept equal to $[M_i - (F_i/F_j)M_j]$. In this way, if the mass and field shift factors are known for the transition j , they can be evaluated also for the transition i . King plots are produced here using the IS of the $(5s[3/2]_2 - 5p[3/2]_2)$ transitions at 760 nm ($j = 760$) measured by Cannon and Janik [129] with an accuracy of about 1 MHz. As an example the King plot for the $5p[5/2]_2$ transition is presented in Figure 3.3, along with a straight line from a weighted linear least-squares fit. The results of King plot analyses are presented in Table 3.3 for four transitions. Since the IS on the $5d[1/2]_1$ transition for the ^{83}Kr isotope is not measured, the King plot does not give significant results, so there are no data reported for this transition. The second

Table 3.3. Results of the IS analysis; the second and third column contain the result from a weighted linear least-squares fit on the King plots; the value of the mass and field shift factors reported in the last two columns are obtained using $F_{760} = -0.605(30)$ GHz/fm² and $M_{760} = 172(17)$ GHz from [130, 131].

transition	(F_i/F_{760})	$[M_i - (F_i/F_{760})M_{760}]$ GHz	F_i GHz/fm ²	M_i GHz
$6s[3/2]_1$	-2.04(83)	986(208)	1.23(50)	635(252)
$5p[1/2]_0$	-1.35(95)	821(254)	0.82(57)	589(302)
$5p[3/2]_2$	-1.06(95)	751(238)	0.64(57)	569(289)
$5p[5/2]_2$	-1.96(89)	976(225)	1.19(54)	639(272)

and third column contain values from the weighted linear least-squares fit on the King plots. In the last two columns an estimate of F_i and M_i is given, based on values of F_{760} and M_{760} reported in the literature. Both Keim *et al.* [130] and Schuessler *et al.* [131] have estimated the field and mass shift factors, using a semi-empirical approach and muonic IS data respectively. Their weighted averages are $F_{760} = -0.605(30)$ GHz/fm² and $M_{760} = 172(17)$ GHz. The highest field shift factor is found for the $6s[3/2]_1$ transition, as expected in an excitation from a p to an s orbital. The large uncertainty in the slope (F_i/F_{760}) hampers physical interpretation of the IS analysis for the $5p[1/2]_0$ and $5p[3/2]_2$ transitions. However, there is an indication, especially for the $5p[5/2]_2$ transition, for a high field shift factor also for transitions from the ground state which do not involve any s electron. This effect is analogous to what was observed in xenon [105, 108], and is ascribed to an increase in the electron density at the nucleus, that results from the removal of a $4p$ electron from the closed shell configuration, thereby strongly decreasing the screening of the inner s electrons.

It is noted, that a King plot analysis of the data for the ($5s[3/2]_2 - 5p[3/2]_2$) 760 nm transitions *versus* the data for the $6s[3/2]_1$ transition reported by Trickl *et al.* [28] yields a slope of about +2.7. The sign is opposite to that derived from the present data, and it would indicate a decrease in the electron density at the nucleus. This appears to be not realistic since the excitation is from a p to an s orbital.

3.3.2 Absolute frequency calibration

Absolute frequency measurements are performed on the transitions $5d[1/2]_1$, $6s[3/2]_1$ and $5p[1/2]_0$, which lie close (i.e., within the scanning range of the ring-dye laser) to a calibrated I₂-line. The main source of systematic uncertainty on the absolute calibration of the transition frequency is the chirp effect in the amplification processes. This effect is estimated to give an uncertainty up to 100 MHz and is sensitive to the specific experimental conditions, especially on the dye used and the wavelength setting of the PDA. The position of the resonant lines were measured for different pump powers for the PDA. For all the investigated transitions it is found that at high pump power (770 mJ/pulse at 532 nm) the transition frequency is red-shifted compared to low pump power (220 mJ/pulse) measurements. This implies that the laser frequency is shifted

Table 3.4. Summary of the ^{86}Kr excited state energy calibrations for three transitions; the second column lists the iodine line used for calibration, the third column shows the measured level energy of the state, and in the last column the difference between our results and the values reported by Kaufman and Humphreys [132] are given.

state	I ₂ line	ν_i^{86} cm ⁻¹	$(\nu_i^{86} - \nu_{i,KH}^{86})$ cm ⁻¹
5d[1/2] ₁	P(11)16-1	103801.8002(12)	-0.0559
6s[3/2] ₁	P(55)12-2	99894.0528(14)	-0.0553
5p[1/2] ₀	R(63)7-4	94092.8673(13)	-0.0563

upward, and the average shift amongst the three transitions is found to be 109 MHz with a standard deviation of about 40 MHz. Of particular interest is the result obtained for the 5d[1/2]₁ transition measurement, in which the PDA is running at 578 nm, with the same dye (Rh B) and concentrations as those used by Eikema *et al.* [34]. Eikema *et al.* [34] developed a technique to actively compensate the chirp effect, and measured a downward shift in the tenth harmonic of the PDA radiation up to 90 MHz when the anti-chirp system was active. We find a shift between high and low PDA pump power measurements of about 66 MHz on the sixth harmonic. If the shift measured by Eikema *et al.* [34] is linearly scaled to the sixth harmonic, a value of 54 MHz is found. Hence, the present assessment of the chirp effect is consistent with the findings of reference [34] and a residual shift of about 10 MHz is left. In the error budget we include, however, a chirp-induced contribution of 30 MHz as a conservative estimate. It has to be noted also that Eikema *et al.* [34] performed measurements of the chirp for various wavelengths. Figure 9 of reference [34] shows that the wavelength dependence of the chirp in the range 577-585 nm is below the 5 MHz level, supporting the estimate of the chirp-induced shift in the present experiment.

Another source of systematic error in the absolute transition frequency calibration originates in the Doppler effect. The crossed beam configuration ensures a low residual Doppler shift, whose value is estimated to be below 20 MHz.

The results of the excited state energy calibrations for the isotope ^{86}Kr performed at low PDA pump power, and the I₂-lines used as references, are presented in Table 3.4. The values of ν_i^{86} reported are the averages over several scans in which the I₂-line and the ^{86}Kr -line are recorded together. The reported uncertainties are the combination of the statistical standard deviation, a residual chirp of 30 MHz, a Doppler uncertainty of 20 MHz, and a small contribution from the uncertainty in the free spectral range of the FPI. In the last column the difference between our result and the values reported by Kaufman and Humphreys [132], $\nu_{i,KH}^{86}$, are shown. Kaufman and Humphreys [132] reported the level energy of several Kr excited states with an internal consistency of 0.0001 cm⁻¹, and an absolute accuracy of 0.15 cm⁻¹. The average value of $(\nu_i^{86} - \nu_{i,KH}^{86})$ is -0.0558 cm⁻¹ with a standard deviation of 0.0005 cm⁻¹ (15 MHz). The small standard deviation may be taken as a reflection of the high relative precision of our measurements. Also, it is an indirect evidence of the small chirp-induced shift since the three krypton lines are measured using different dyes.

Taking into account the possible systematic shift due to both chirp and Doppler effects, a correction of $-0.0558(13) \text{ cm}^{-1}$ on the energy values given by Kaufman and Humphreys [132] is proposed here. This results in a calibration of the excited state energies of Kr to the 0.0013 cm^{-1} level of accuracy. This correction is not entirely consistent with the value $-0.0679(61) \text{ cm}^{-1}$ suggested by Trickl *et al.* [28], who calibrated three VUV-transitions in Kr with a laser system based on a PDA, although both corrections point in the same direction and are of the same order of magnitude. Trickl *et al.* [28], however, measured the absolute frequency of the PDA seeding light with respect to Doppler broadened I_2 absorption lines with an uncertainty of 0.001 cm^{-1} (30 MHz), and a +9 MHz shift of their PDA output was assumed without critical discussion. In view of this we claim that our result should be adopted instead, since our standard deviation is more than an order of magnitude smaller.

The new, accurate values of the excited state energies allows for an evaluation of the isotope dependent ionization energy, E . Yoon and Glab [122] studied krypton Rydberg series excited from the $5p[3/2]_{1,2}$ states, and reported a value of $E = 112914.500(14) \text{ cm}^{-1}$, where the uncertainty in the initial state energies, corrected according to the suggestion by Trickl *et al.* [28], is not considered. When our correction on the energy level values is included instead, then 0.012 cm^{-1} must be added to this value. Moreover, Yoon and Glab [122] performed spectroscopy using natural krypton, in which ^{84}Kr is by far the most abundant isotope, without resolving any isotopic structure. If we assume that the lines they observed are attributed mainly to the ^{84}Kr isotope, then the shift on the $5p[3/2]_{1,2}$ state energies between ^{86}Kr and ^{84}Kr , $\sim 0.004 \text{ cm}^{-1}$ [128], must also be accounted for. In view of these considerations an estimate for the ionization energy of ^{86}Kr , $E^{86} = 112914.516(14) \text{ cm}^{-1}$, can be given. From this value, ionization energies for the other even isotopes can also be deduced making use of the data reported by Kaufman [128] for the differences of the ionization energies between even isotopes, $E^{n,n-2} \sim 0.008 \text{ cm}^{-1}$. Finally, it has to be noted that the present estimate of the isotope dependent ionization energies for krypton is consistent with the isotope independent value of $112914.50(2) \text{ cm}^{-1}$ adopted by Klar *et al.* [133] after a critical discussion on the data reported in the literature.⁴

3.3.3 ac Stark effect

The ac Stark effect in an atomic transition arises from the perturbation of the atomic states by a strong time-dependent electro-magnetic field, for example a high intensity laser pulse. An investigation on the ac Stark effect of the two-photon $5p[1/2]_0$ transition is performed measuring the ^{84}Kr isotope 2UV+1UV photoionization spectra, and the reference R(63)7-4 I_2 line, for different powers of the UV laser pulses. A $f=1 \text{ m}$ UV grade fused silica lens is used to increase the UV power density in the interaction region where the beam waist is located. The UV beam diameter at the lens is $\sim 3 \text{ mm}$, and in the interaction region it is $\sim 90 \mu\text{m}$ (assuming a Gaussian spatial beam profile), resulting in a power density of about 2.6 GW/cm^2 at 1 mJ/pulse energy. A conservative estimate of the uncertainty on the actual power density of 50% is assumed, related to possible hot spots in the beam. The confocal parameter of the focused beam is about 6

⁴A more recent and accurate determination of the ionization energy of krypton is discussed in Section 3.5.

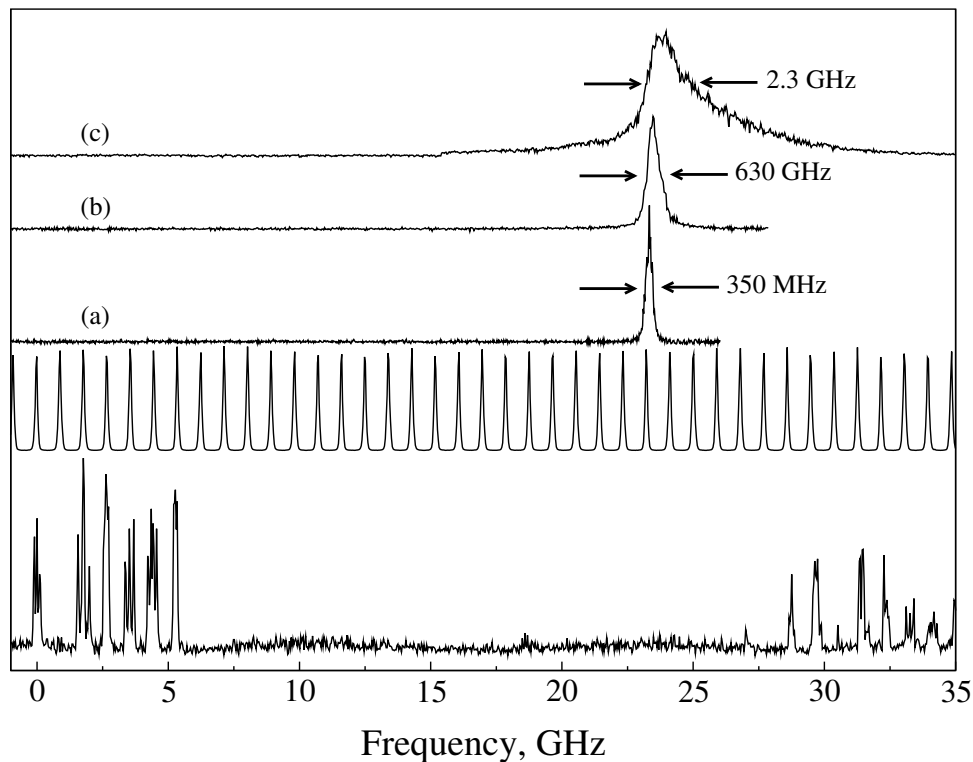


Figure 3.4. Photoionization spectra of the two-photon $5p[1/2]_0$ transition for ^{84}Kr measured at different power densities: (a) $\leq 0.2 \text{ MW/cm}^2$ (b) $\sim 260 \text{ MW/cm}^2$, (c) $\sim 2.6 \text{ GW/cm}^2$; the R(63)7-4 I_2 line (on the left) and the etalon markers are also shown; the frequency scale is the actual transition frequency and the zero is set at the “t” component of the reference I_2 line.

cm, much larger than the diameter of the krypton beam in the interaction region which is of the order of a few millimetres. This justifies the assumption of a plane-wave analysis with nearly constant intensity in the interaction volume. When the focusing lens is not used an upper limit of the power density in the interaction region of about 2 MW/cm^2 at 1 mJ/pulse energy can be estimated for a collimated UV beam.

In Figure 3.4, typical spectra recorded at different UV pulse energies are shown along with the etalon markers and the I_2 line. The frequency scale is the actual transition frequency, i.e. six times the PDA frequency, relative to the “t”-component of the R(63)7-4 I_2 line. Trace (a) is recorded without the focusing lens and at low PDA pump power, resulting in a UV energy of 0.1 mJ/pulse ($\leq 0.2 \text{ MW/cm}^2$); trace (b) is obtained under the same conditions as trace (a) but using the focusing lens ($\sim 260 \text{ MW/cm}^2$); trace (c) is the spectrum recorded using the lens and high PDA pump power (1 mJ/pulse UV energy, $\sim 2.6 \text{ GW/cm}^2$). The spectrum of trace (c) is corrected for a chirp-induced shift of 146 MHz to be consistent with the other traces (see discussion above). The ^{84}Kr line is measured for various UV pulse energies, using various neutral density filters. The line exhibits a symmetric broadening and a net shift to the blue for power densities up to $\sim 260 \text{ MW/cm}^2$. The full-width at half-maximum of the line measured at $\sim 260 \text{ MW/cm}^2$ is $\sim 630 \text{ MHz}$, compared to 350 MHz measured at low pulse energy without using the focusing lens.

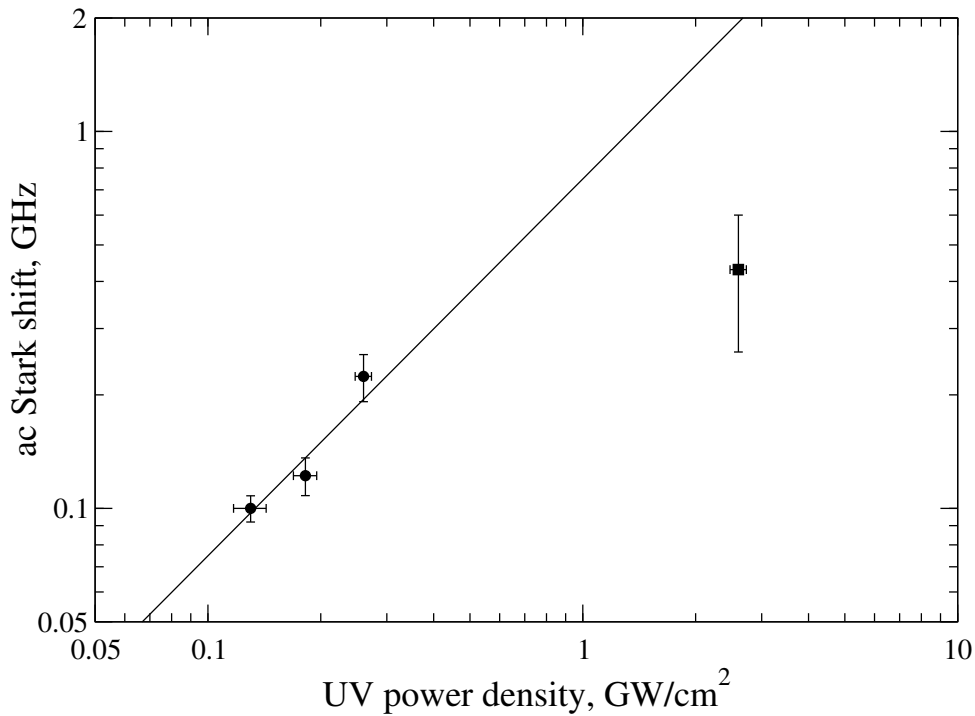


Figure 3.5. Measured ac Stark shifts on the $(4p^6 - 4p^55p[1/2]_0)$ two-photon transition in krypton as a function of UV power density; the circles are the low power density data which indicate a linear shift and the straight line is the result of a weighted linear least-squares fit on these data; the triangle is the sub-linear high intensity shift.

In Figure 3.5 the measured ac Stark shifts are presented in a logarithmic plot. The straight line is the result of a linear least-squares fit on the low UV energy data (circles); the origin is set at the unperturbed transition frequency. The fit yields a slope of $0.75(48) \text{ Hz}(\text{W}/\text{cm}^2)^{-1}$, where 50% uncertainty on the actual power density is considered, and an intercept of $23.377(44) \text{ GHz}$, which is compatible with the value $23.374(9) \text{ GHz}$ obtained without using the lens, i.e. with power density $\leq 0.2 \text{ MW}/\text{cm}^2$ (trace (a) in Figure 3.4). The high energy data point (square) represents the peak position of trace (c) in Figure 3.4, and indicates a sub-linear shift at high UV power density. This is consistent with the result of Camparo and Lambropoulos [134], who performed a Monte Carlo simulation on the ac Stark effect of a two-photon transition assuming a stochastic single-mode light field. At higher laser intensities the resonance shows an asymmetric profile, with a long tail toward higher frequency, i.e. in the direction of the ac Stark shift, and a FWHM of about 2.3 GHz. This is also predicted from ac Stark effect calculations [134, 135, 136], and is due to the temporal variation of the actual field intensity during a laser pulse.

3.3.4 Consequences for narrow-band XUV/VUV generation via two-photon resonance in Kr

The advantageous use of two-photon resonances in Kr and Xe to enhance the generation of XUV/VUV radiation has been investigated and implemented in spectro-

scopic applications by various groups [42, 43, 45, 46]. Several orders of magnitude increase in the XUV/VUV yield is obtained if one of the lasers is tuned to resonance in a four-wave mixing scheme, and the $5p[1/2]_0$ resonance has proven to be the most efficient [42]. Particularly for the application of narrow-band radiation in precision spectroscopy, the exact calibration of the two-photon resonances is of importance.

One important application of this scheme has been pursued by the Stoicheff group [45], determining the dissociation energy of hydrogen. They measured the resonance frequency of the $5p[1/2]_0$ two-photon transition by monitoring resonance-enhanced third-harmonic generation (THG) at 70.9 nm, and reported a value of $94093.00(4) \text{ cm}^{-1}$, measured with a UV power density of $8 \times 10^8 \text{ W/cm}^2$. From our result on the ^{86}Kr transition frequency and the ac Stark shift, we derive a value for this energy of 94092.89 cm^{-1} at the reported UV power density. A conservative estimate of the uncertainty in this value is 0.02 cm^{-1} , where a small contribution of $\sim 0.005 \text{ cm}^{-1}$ from the isotopic composition of natural krypton is also included. Hence, a correction of -0.11 cm^{-1} has to be applied to the calibration of the krypton resonance as well as on the dissociation limit of the hydrogen and deuterium molecule.

Recently also the Merkt group [46] performed frequency calibration on the same transition by monitoring the resonance-enhanced THG yield. They observed a line at 94092.91 cm^{-1} , calibrated using the Doppler broadened I_2 -reference standard. The UV power density in their experiment can be estimated as $4 \times 10^9 \text{ W/cm}^2$, based on the reported pulse energy (50 μJ) and duration (15 ns), focal length of the used lens (16 cm) and assuming a beam diameter at the lens of about 4 mm. We derive a value for the energy of $94092.90(2) \text{ cm}^{-1}$ at this power density, which agrees very well with the calibration based on the THG yield. Also the line-width reported in Ref. [46], $\sim 0.12 \text{ cm}^{-1}$ (3.6 GHz), is compatible with the ac Stark broadening measured in the present experiment.

Third-harmonic generation and resonant-enhanced multiphoton ionization are processes which may give rise to different calibration results. Phase-matching plays a role in THG and may influence the peak position of the line, as well as does the competition with resonant-enhanced multiphoton ionization. Also, in our crossed beam setup we perform spectroscopic measurements at low densities in the collision-free regime of a skimmed atomic beam, while THG takes place close to the valve of a freely expanding jet where collisions are present. So, a comparison between frequency calibrations based on the two different techniques is not straightforward. Analogous considerations apply also to the ac Stark shift measured by the Stoicheff group, $2.6(1.1) \text{ Hz (W/cm}^2)^{-1}$, which is not completely compatible with our finding, although of the same order of magnitude.

An additional feature is of importance in the application of two-photon resonance-enhanced XUV generation. As implicitly demonstrated in the experiment of the Stoicheff group, but not explicitly documented, the resonance also acts as a wavelength selective element. The XUV-output in Ref. [45] allowed for measuring hydrogen resonances at a resolution of 0.25 cm^{-1} , while the bandwidth of the laser at 425 nm (before frequency doubling) was already 0.2 cm^{-1} . Clearly the bandwidth of the XUV radiation is narrower than the convolution of the bandwidth of the incident lasers, when accounting for doubling and two-photon excitation.

A delicate interplay between the wavelength selection, ac Stark effect, isotopic com-

position, competition between ionization and XUV production, and the collisional effects on the macroscopic nonlinear susceptibility will determine the exact centre frequency and bandwidth of the XUV radiation generated. Future research, that can establish the dependencies on these parameters and conditions is required.

The application of electromagnetically-induced transparency to enhance the efficiency in this wave-mixing scheme is another feature of interest. Dorman *et al.* [137] measured high conversion efficiency in a four-wave-mixing scheme via the $(4p^6 - 4p^55p[1/2]_0)$ two-photon resonance in Kr, enhanced by electromagnetically-induced transparency. The result was obtained by tuning a second laser in resonance with the $(5p[1/2]_0 - 5s[1/2]_1)$ transition at 759 nm, inducing transparency of the medium at the $(4p^6 - 4p^55s[1/2]_1)$ transition with a resonant wavelength of 123.6 nm. Dorman *et al.* [137] also suggested future investigation of the process with narrow-band UV light.

3.4 Conclusions

Accurate one-photon VUV and two-photon UV resonantly enhanced photoionization spectroscopy is performed on five transitions from the ground state of krypton. Using a time-of-flight mass-spectrometer, spectroscopic information on all stable isotopes is obtained. King plot analyses on the isotope shifts indicate high field-shift factors, even for those transitions in which no *s* electron is involved. This reveals a large screening effect of the closed shell *p* electrons on the inner *s* electrons, as already shown for xenon.

Absolute frequency calibration is performed for three transitions. A correction of $-0.0558(13) \text{ cm}^{-1}$ to the excited state energy values reported by Kaufman and Humphreys [132] is suggested. The excited state energies of krypton are determined with an accuracy of about 40 MHz. This result, combined with data reported in the literature, leads to a determination of the ionization energies for all even isotopes.

The ac Stark effect on the two-photon $(4p^6 - 4p^55p[1/2]_0)$ transition is also investigated. A linear shift of $0.75(48) \text{ Hz}(\text{W}/\text{cm}^2)^{-1}$ is found for power densities up to $260 \text{ MW}/\text{cm}^2$. At higher light intensity the line exhibits a sub-linear shift and an asymmetric broadening with a long tail in the direction of the frequency shift.

Finally, consequences of accurate transition frequency calibration for resonance-enhanced narrow-band XUV/VUV generation are discussed. Further investigations are needed to establish the influence of the experimental conditions on the exact central frequency of the XUV/VUV yield, in particular when the generated radiation is used in precision spectroscopy.

3.5 Appendix: new determination of the ionization energy of krypton

The ionization energy of noble gases is determined as a limit to a Rydberg series. The Rydberg level energies of those atoms are usually determined by accurate frequency spectroscopy of transitions from a metastable state. To obtain an absolute value of the Rydberg series limit the level energy of the starting metastable state is added to

Table 3.5. Summary of the ionization energy of krypton reported in the literature, as given in [47]. The new value determined in [47] is also reported for comparison.

Original values cm ⁻¹	Values corrected as recommended in Section 3.3.2 cm ⁻¹	References
112915.2	112914.43	Moore 1952 [138]
112914.6(1)	112914.6(1)	Yoshino and Tanaka 1979 [139]
112914.47(3)	112914.414(30)	Delsart <i>et al.</i> 1981 [140]
112914.40(3)	112914.412(30)	Sugar and Musgrove 1991 [141]
112914.41(2)	112914.422(20)	Bounakhla <i>et al.</i> 1993 [142]
112914.50(3)	112914.512(30)	Yoon and Glab 1994 [122]
112914.441(16)	112914.441(16)	Hollenstein <i>et al.</i> 2003 [47]

the measured Rydberg series limit, and the final uncertainty is usually limited by the accuracy on the level energy of the metastable state. In Section 3.3.2 an accurate determination of the energy interval between the ground state, 1S_0 , and several excited states of krypton is reported, which allows for a new determination of the level energies of krypton with an accuracy of 0.0013 cm^{-1} . Thanks to this measurement an accurate value of the ionization energy $112914.516(14) \text{ cm}^{-1}$ is given assuming the Rydberg series limit obtained by Yoon and Glab [122] by pulsed laser spectroscopy from the $5p[3/2]_{1,2}$ states. Unfortunately, for krypton there exists no accurate determination of the Rydberg series limit based on cw laser spectroscopy. This was for example the case for the argon atom where the group of Hotop [143] performed highly accurate cw laser spectroscopy from the $4p[5/2]_3$ level; these results, combined with measurement of a VUV transition using laser [107], led to an accurate value of the ionization energy.

Recently, Hollenstein *et al.* [47] pointed out a discrepancy between various values of the ionization energy of krypton reported in the literature as summarized in Table 3.5. It has to be noted that the value $112914.516(14) \text{ cm}^{-1}$ given in Section 3.3.2 is inconsistent with the other values of the first column in Table 3.5. Note that the value reported by Yoshino and Tanaka [139] is not effected by the new energy level values given in Section 3.3.2 since it is determined from a single-photon VUV absorption spectrum.

In order to clarify this inconsistency, Hollenstein *et al.* [47] carried out an independent determination of the ionization energy of krypton measuring directly the Rydberg level energies by accurate single-photon VUV spectroscopy from the ground state. They used a broadly tunable narrow-band VUV source [46], and found a value of $112914.441(16) \text{ cm}^{-1}$ for the ionization energy of ^{86}Kr . The value reported by Yoon and Glab [122] is still inconsistent with the value by Hollenstein *et al.* [47]. This explains also the inconsistency of the ionization energy value of $112914.516(14) \text{ cm}^{-1}$ reported in Section 3.3.2.

Part II

A novel setup for narrow-band HHG

Chapter 4

Laser system

In this chapter a novel laser system delivering high-energy pulses in the near-infrared region is presented. The pulses are nearly Fourier transform limited (time-bandwidth product of 0.48), providing narrow-band radiation (~ 1.5 GHz), with an energy of 225 mJ and 10 Hz repetition rate. The pulse duration of 320 ps covers the intermediate region between Q-switched and mode-locked lasers, and provides high peak powers. The nearly Gaussian beam profile, with a beam quality factor of $M^2 = 1.2$, enables tight focusing, reaching intensities exceeding 5×10^{13} W/cm². The system operation is demonstrated near 780 nm, however the tunability extends over the range 700 - 970 nm. The laser system is suitable for high-order harmonic generation in the extreme-ultraviolet region for high-resolution frequency domain spectroscopy.

(This Chapter corresponds to Ref. [144]: Rev. Sci. Instrum. **74** (2003) 32.)

4.1 Introduction

The majority of modern high peak power pulsed laser sources is based on the concept of Q-switching and mode-locking. The most commonly used Q-switched lasers, the Nd:YAG laser and a variety of excimer lasers, generate powerful pulses with typical durations of 5-15 ns. These sources are often employed for pumping secondary, tunable pulsed lasers. Despite the advances in solid state and semiconductor laser technology, dyes in solution are still widely applied as gain media in such tunable lasers. As a consequence of their typical excited state lifetime of about 1 ns, pulsed dye lasers have an excellent trigger stability, with respect to the Q-switched laser, within a fraction of the pulse duration. Mode-locked lasers have typical pulse durations below 50 ps. Recent developments utilize Kerr-lens mode-locking in Ti:Sapphire (Ti:Sa) producing pulses as short as 5 fs. Such radiation sources have a wide range of applications in many areas of science, specifically in high-order harmonic generation and X-ray production.

The present paper describes an alternative laser source developed from the point of view achieving narrow-band and tunable extreme ultraviolet (XUV) radiation as a tool for frequency domain spectroscopy. Four-wave mixing with nanosecond laser pulses in gaseous media has become a well-established technique and in the past decade several groups have demonstrated the generation of Fourier-transform (FT) limited nanosecond pulses in the XUV-domain with on-line applications in spectroscopy [27,

34, 46]. Although Eikema *et al.* [34] succeeded in generating 5th harmonic at wavelengths as short as 58 nm with FT-limited nanosecond pulses, the photon yield remained below 10⁵ photons per pulse. Further up-scaling of nanosecond pulses towards higher energies, in order to obtain the peak intensities required for efficient 5th and 7th harmonics generation, is hardly feasible. Furthermore such highly energetic pulses would fully ionize the gaseous medium used for harmonic generation, which would leave no harmonic conversion yield. On the other hand it has been demonstrated that at intensities above 10¹³ W/cm² the so-called plateau of high-harmonics is reached [68]. Initially, studies on the plateau region were performed with non-tunable mode-locked laser pulses at typical durations of 50 ps [51]; meanwhile, with the production of energetic pulses at sub-10 fs durations, harmonics at $n \sim 100$ have been demonstrated [145]. However, such sources have an intrinsically broad frequency spectrum (~ 100 nm).

From the perspective of XUV frequency spectroscopy with higher resolution than that achievable with synchrotron sources, where the limiting bandwidth is at 1 cm⁻¹ [146], the range of intermediate pulse durations between the typical Q-switched and mode-locked lasers is of interest. An XUV source with sub-cm⁻¹ bandwidth can be developed on the basis of high-order harmonic generation, provided that FT-limited pulses of 100-500 ps duration and peak intensities higher than 5×10^{12} W/cm², are produced. One successful approach is that of a distributed feed-back dye laser (DFDL), which in principle produces wavelength-tunable sub-ns pulses with FT-limited bandwidth [147, 148]. The tunability of a DFDL-system is intrinsically complicated in view of the fact that its wavelength is determined by the creation of a periodic intensity modulation in the gain medium. At the Lund Laser Centre, an XUV-laser source was constructed [97] based on harmonic generation using the amplified output of a DFDL-system, emitting tunable pulses of about 50 ps duration. Even though the laser pulses at the fundamental wavelength were claimed to be FT-limited, the XUV-bandwidth was 30 cm⁻¹, more than an order of magnitude beyond the FT limit [97]. This system generates harmonics on the plateau at wavelengths as short as 35 nm and is routinely used for spectroscopic investigations [149].

Our work focuses on an alternative method for producing pulses in this intermediate temporal domain. In a series of studies it has been shown that the FT-limited output of frequency-doubled Q-switched Nd:YAG lasers can be temporally compressed from 5-6 ns to 300 ps with conversion efficiencies of 90%, using the stimulated Brillouin scattering (SBS) process in a liquid [150, 151, 152]. Here we demonstrate that it is possible to convert fixed-frequency, compressed pulses from a Q-switched Nd:YAG laser into wavelength-tunable pulses using a travelling-wave pulsed-dye-amplifier (PDA). Near-infrared dyes in solution are used as a gain medium in the PDA. Wavelength-tunable pulses of 300 ps duration are produced and subsequently amplified in a Ti:Sa amplifier, yielding output energies of 225 mJ/pulse at 10 Hz repetition rates. The physical characteristics of this laser system are described in terms of frequency bandwidth, pulse duration and spatial beam quality. The properties are such, that under focusing conditions, peak intensities higher than 10¹³ W/cm² can be produced. Therefore, the pulses produced by the laser system are well suited for applications involving higher-order harmonic generation in the plateau region, thus providing a potential coherent source of sub-cm⁻¹ bandwidth XUV-radiation with wavelengths as short as 35 nm.

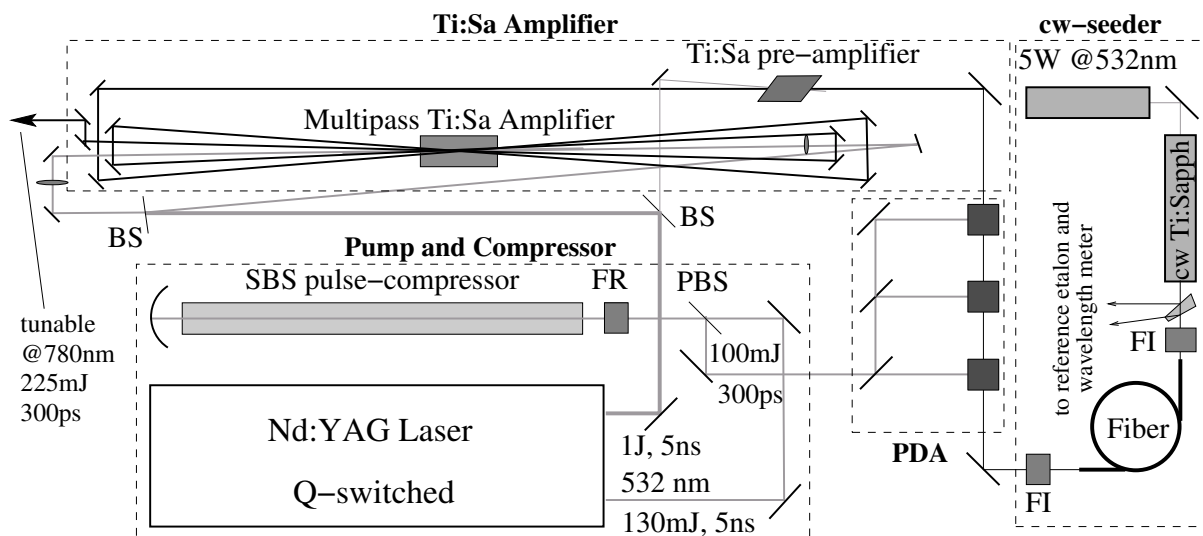


Figure 4.1. Schematic diagram of the laser system; FI: Faraday isolator; BS: beam splitter; PBS: polarizing beam splitter; FR: Fresnel Rhomb.

4.2 Laser system

A schematic diagram of the laser system is shown in Figure 4.1. The primary source is a cw Ti:Sa ring-laser pumped by a solid-state cw laser, delivering narrow-band tunable radiation in the near-infrared (Sec. 4.2.1). Its output is transmitted through a short, polarization-maintaining single-mode fiber to seed a three-stage pulse-dye-amplifier (Sec. 4.2.2), pumped by 300 ps FT-limited pulses from the compressed secondary output of an injection seeded, Q-switched and frequency-doubled Nd:YAG laser (Sec. 4.2.3). Compression of the pump laser is achieved by stimulated Brillouin scattering in a water cell [152].

After dye amplification, pulses of ~ 300 ps duration and energy of 2 mJ are obtained and further amplified in two Ti:Sa crystals pumped by the main frequency-doubled output of the Nd:YAG laser (see Sec. 4.2.4). At the output of the amplification chain, nearly FT-limited pulses of 320 ps, with energy of 225 mJ and tunable around 780 nm are produced.

4.2.1 cw-seeder

The fundamental frequency of the laser system is provided by a cw Ti:Sa ring-laser (Coherent 899-21) pumped by a frequency-doubled diode-pumped Nd:YVO₄ laser (Spectra Physics Millennia 5 W). Wavelengths within the Ti:Sa range are generated with 550 mW power and 1 MHz bandwidth. Continuous single-mode scanning spans up to 30 GHz. While the experiments described here are performed around 780 nm, the tunability of this fundamental seed source covers the range 700-970 nm.

Two auxiliary beams are created from the main laser beam using a glass wedge. One is sent to a wavelength-meter (Burleigh WA-20) for on-line absolute frequency monitoring, while the other is sent to a reference etalon for relative frequency mea-

surements.

The laser beam transmitted through the wedge passes through a Faraday isolator and is launched into a short (1 m) polarization-maintaining single-mode fiber (3M FS-PM-4611). The optical isolator ensures that light, reflected from the input-tip of the fiber, is not coupled back into the ring-laser, thereby disturbing its frequency stabilization. The fiber decouples the alignment of the cw ring laser from that of the PDA, hence increases stability of operation, and additionally serves as spatial filter ensuring a TEM₀₀ seed-beam. At the output of the fiber, another Faraday isolator is placed to prevent damage of the output-tip of the fiber from possible counter-propagating amplified spontaneous emission radiation arising when the PDA is not well seeded, e.g. during the alignment of the pump beams. The light transmitted through the isolators and single mode fiber, typically 250 mW, is used for seeding the three-stage pulse-dye-amplifier.

4.2.2 Pump and compressor

The pump laser of the system is an injection seeded, Q-switched Nd:YAG laser (Quanta Ray GCR-330) operating at 10 Hz repetition rate. The main frequency-doubled output of the Nd:YAG laser delivers 5 ns pulses at 532 nm with an energy of 1 J and is used to pump the Ti:Sa amplifier. The left-over of the fundamental infrared radiation from the Nd:YAG laser is frequency-doubled in a second crystal, where pulses of 130 mJ at 532 nm are produced. These pulses are compressed down to 300 ps and used to pump the PDA.

The beam from the secondary output of the Nd:YAG laser passes through a thin-film polarizer used as a high-power polarizing beam-splitter (PBS). After a Fresnel rhomb the horizontally polarized beam is transformed into a circular polarization state and enters a Brillouin cell filled with water. A concave mirror, of 10 cm focal length, placed behind the cell focuses the light back into the water. In the focal plane a phase-conjugate back-reflected Stokes pulse is generated, which is amplified by stimulated Brillouin scattering along the counter-propagating input pulse. This gives rise to temporal compression towards pulse duration corresponding to the lifetime of acoustic phonons in the liquid. For water at wavelength of 532 nm, the lower limit is 300 ps, which is reached routinely if the pump energies are sufficiently high (for more details on the SBS pulse compression see Ref. [152]). The SBS-pulses are separated taking advantage of their polarization. The SBS process does not conjugate the polarization state of the light, hence, after passing through the Fresnel rhomb again, the polarization is orthogonal to the input one and is reflected by the PBS. At the output of the SBS compressor, pulses with energy of 100 mJ are obtained. The Stokes SBS-pulses are red-shifted by ~ 7 GHz with respect to the pump pulses; this has no effect on the output frequency of the tunable PDA system, since the compressed pulses are only used for creating a population inversion in the gain medium.

4.2.3 Pulsed-dye-amplifier

A crucial issue for the design of the present laser system is the conversion of the compressed pump pulses into pulses tunable in wavelength and with pulse duration simi-

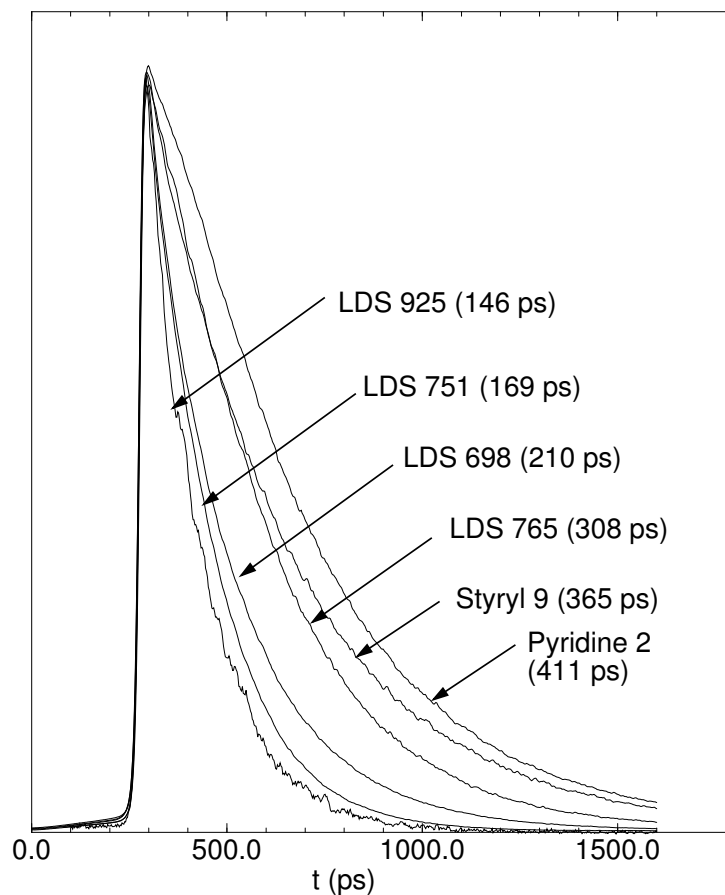


Figure 4.2. Fluorescence decay curves for various near-infrared dyes dissolved in methanol at their typical concentrations as used in dye lasers. The measurements were performed by excitation with a femtosecond pump pulse at 530 nm and fluorescence was detected by a picosecond fluorescence streak camera. The experimentally determined decay times are specified for each curve.

lar to that of the pump. In a setup employing traveling-wave amplification the excited state lifetime of the gain medium must be of the same order or smaller than the pump pulse duration. The excited state lifetime of some near-infrared dyes, for which the gain curves overlap with the Ti:Sa gain curve, are measured by monitoring the fluorescence after femtosecond (100 fs at 530 nm) pulse excitation. The fluorescence signal is recorded with a fluorescence streak camera having temporal resolution better than 3 ps. The dyes are dissolved in methanol at typical concentrations used in dye lasers, i.e. 100 mg/l (the LDS dyes are obtained from Exciton, whereas the Styryl-9 and Pyridine-2 dyes are obtained from Radiant Dyes). For some dyes, measurements at different concentrations are performed to verify if stimulated emission would reduce the excited state lifetime, but no such effects are found. The possibility to measure dispersed fluorescence by the fluorescence streak camera is employed to verify whether the specific wavelength in the fluorescence channel affects the lifetimes. Such effects are not found except in the case of LDS-925 dissolved in methanol. This liquid emits fluorescence in a window around 925 nm with a typical response of 150 ps, but additionally a minor channel of yellow fluorescence is observed with a decay time of 1-2

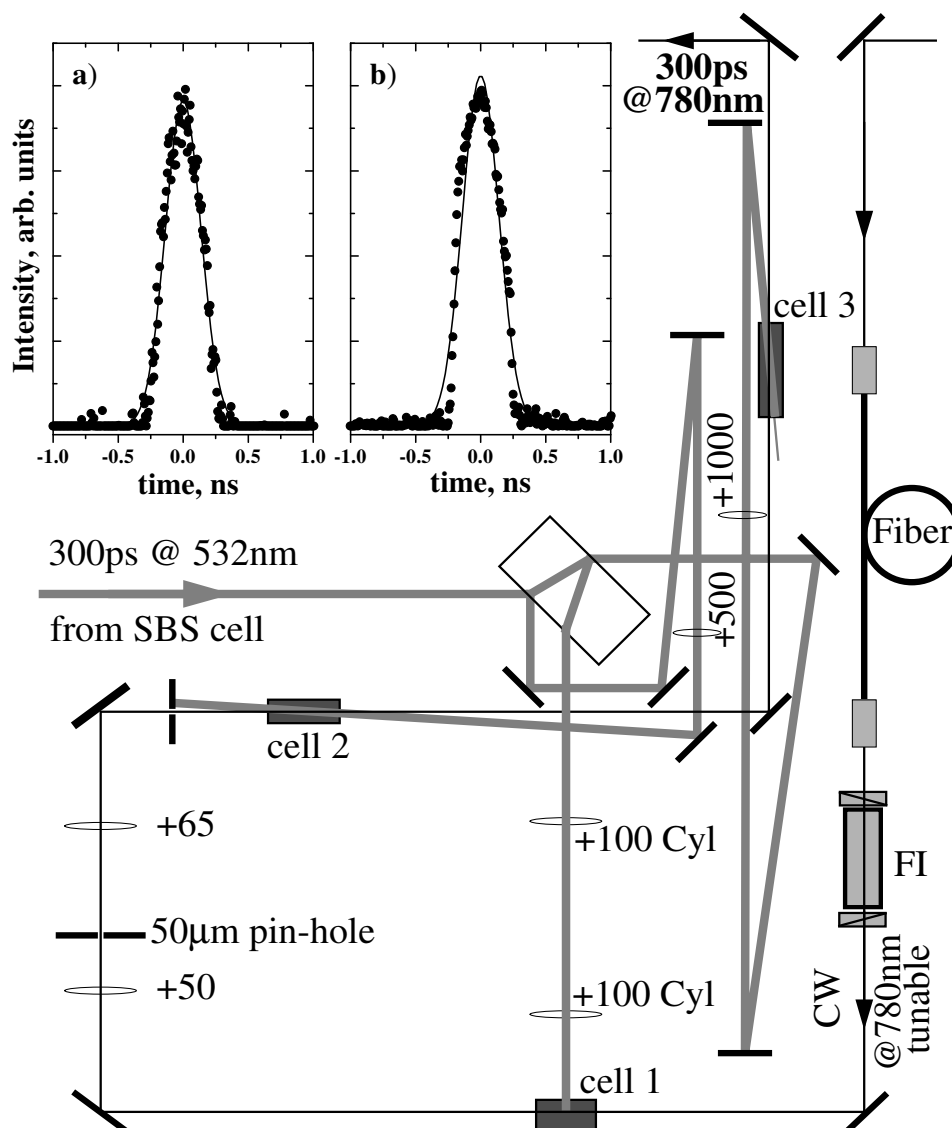


Figure 4.3. Detailed scheme of the PDA setup. In the inset the typical temporal profile of the pump pulse (a), $\text{FWHM}=320(20)$ ps, and PDA output pulse (b), $\text{FWHM}=330(20)$ ps, are shown.

ns. This phenomenon is not further investigated. Finally, for the case of LDS-751 dye the dependence of the lifetime on the solvent is studied. With the use of propylene-carbonate the decay time is found 25% longer and with ethanol it is 40% longer than for methanol. The experimentally determined fluorescence decay curves are shown in Figure 4.2. The six dyes cover the Ti:Sa gain range from 680 to 970 nm. All investigated near-IR dyes exhibit an excited state lifetime of 150-400 ps, hence they are suitable for producing pulses of 300-400 ps duration in a traveling-wave amplifier setup pumped by the SBS-compressed pulses at 532 nm.

The PDA setup, shown in detail in Figure 4.3, consists of three dye cells. The first cell of the amplifier chain (139 mg/l LDS 765 in methanol) is transversally pumped by 4% of the pump power. The emerging pulses are spatially filtered and then amplified in two consecutive amplification cells (39 mg/l), both longitudinally pumped in direc-

tion opposite to the seed-beam. This design has the advantage that the gain increases along the propagation direction of the seed-beam. Such a geometry also reduces the amount of spontaneous emission. The pump beams are focused such that their beam diameters match those of the seed-beam in the cells. The second amplifying cell is pumped by 4% of the pump power, while the remaining 90 mJ pumps the last cell. In the geometrical layout of the PDA special care must be taken to match the timing of the pump and the IR pulse generated in the first cell, in view of the rather short duration of the pulses (~ 10 cm spatial length) and the short excited state lifetime of the dye.

In the inset of Figure 4.3 the typical temporal profile of the pump pulse (a) and output pulse (b) of the PDA are shown. These measurements are performed using a streak camera (Hadland IMACON 500-20 ps), and result in 320(20) ps full-width half-maximum (FWHM) pulse duration for the compressed pumping pulses and 330(20) ps for the PDA output pulses. The alignment of the PDA is optimized on maximum output power, measured at the final output, about 10 m away from the last dye cell. Monitoring the beam in the far field, the contribution of the amplified spontaneous emission is minimized, and a good spatial beam quality is obtained. Typical energy of the PDA output pulses is about 2 mJ, without correcting for the reflection and absorption losses of the Ti:Sa crystals.

4.2.4 Ti:Sapphire amplifier

The Ti:Sapphire amplifier consists of two stages: a single-pass pre-amplifier followed by a multi-pass amplifier. The laser beam from the main output (5 ns, 1 J) of the powerful Nd:YAG laser is split into two parts by a 90/10 beam-splitter, providing two pump channels of approximately 900 mJ for the multipass-amplifier, and 100 mJ for the single-pass pre-amplifier.

The crystal in the pre-amplifier is longitudinally pumped and Brewster-cut to avoid reflection losses. It is mounted in a brass holder, and the rectangular cross-section of the crystal allows for a good direct-contact cooling from four sides. The timing of the pump and seed beams is not so critical as for the PDA. The ~ 3 μ s life time of the Ti:Sa excited state provides enough room for time delay between the seed and pump pulse on a time-scale of a few tens of nanoseconds. In the practical realization of the pre-amplifier the pump-pulse arrives 13.6 ns before the seed-pulse, as measured with a fast photodiode. Direction and size of the pump beam are optimized to achieve maximum amplification. The typical pulse energy after the pre-amplifier is ~ 6 mJ, corresponding to an amplification factor of about three.

The power amplifier of the laser system is a 4 pass Ti:Sa amplifier in a mono-planar geometry. The crystal is a high-damage threshold, high-quality laser rod. It has cylindrical shape, with length and diameter of 10 mm. The plane parallel faces are broad-band anti-reflection coated in order to minimize reflection losses, at both pump and seed wavelengths. The crystal holder is a massive brass cylinder. Thermal contact is ensured by a copper cylindrical ring which hosts the crystal and is nested into the brass holder. The holder is temperature stabilized with an active water cooling system and the typical working temperature is 20°C. The crystal is longitudinally pumped from both sides. The main pump beam is divided with a 50/50 beam splitter into two beams that are focused by two lenses (focal length = 1 m) to have diameter at the crystal of

about 8 mm. A time delay of ~ 5 ns is introduced between the two pump pulses in order to avoid their interference inside the crystal. Pulses of 225 mJ are obtained from the four-pass amplifier, corresponding to an amplification factor of about 38.

4.3 Characterization of the laser system

In this section the characteristics of the high-energy output pulses of the laser system are presented. In Sec. 4.3.1 the pulse time duration and the frequency bandwidth of the pulses are characterized. In Sec. 4.3.2 the spatial quality of the output beam is evaluated.

4.3.1 Temporal and frequency characteristics

The time duration of the pulses is measured with a fast photodiode in combination with a 1 GHz oscilloscope (Tektronix TDS 680B, 5Gs/s). The result of a single shot measurement for a selected short pulse is shown in Figure 4.4. The impulse response function (IRF) of the detection system, measured with 100 fs pulses, is also shown in the inset of Figure 4.4. Due to the slow response of the detection system a deconvolution procedure is necessary to extract the actual pulse time profile from the measured curve. Assuming Gaussian pulses, the convolution of the IRF and the pulse temporal profile is calculated, with the FWHM of the Gaussian as the only parameter. In Fig. 4.4, the solid line curve is obtained with a FWHM of 300 ps for the time profile of the pulse. The average pulse duration of the powerful infrared pulses, estimated on the basis of several single shot measurements, is 320(20) ps.

The frequency bandwidth of the pulses is measured using a solid etalon with a free spectral range (FSR) of 21 GHz and finesse 25. The output of the laser system, attenuated using several neutral density filters, is sent through the etalon, while scanning the cw Ti:Sa ring-laser. The transmission of the etalon, measured with a fast photodiode in combination with a boxcar integrator, is shown in the lower trace of Figure 4.5 (open circles). The transmission through the reference etalon (FSR=7.5 GHz) of the cw light from the ring Ti:Sa laser (upper trace of Figure 4.5) is measured simultaneously, and gives the relative frequency scale. To evaluate the frequency bandwidth of the pulse a Gaussian spectral profile is assumed, and the transmission of the etalon is calculated convoluting the transmittance of the etalon, i.e. the Airy function, with a Gaussian profile with the FWHM as a parameter. The dashed and dotted curves on Figure 4.5, are the results of the calculations assuming a FWHM of 1.8 and 1.2 GHz respectively. The FWHM of the spectral density of the pulse is estimated to be 1.5(3) GHz. The product of the FWHM's of the temporal and spectral profiles of the powerful infrared pulses is about 0.48, hence demonstrating that the pulses are close to the FT limit (in which case the product is 0.44).

Since the amplified beam is intended for use in high-resolution frequency-domain spectroscopic studies the value of the central frequency of the pulses is of importance. The absolute frequency of the cw-seed laser is accurately measurable by comparison to stabilized etalon fringes and reference standards. The saturated iodine spectrum produces an accuracy of 1 MHz (1σ). [124, 153] Although its use has not yet been es-

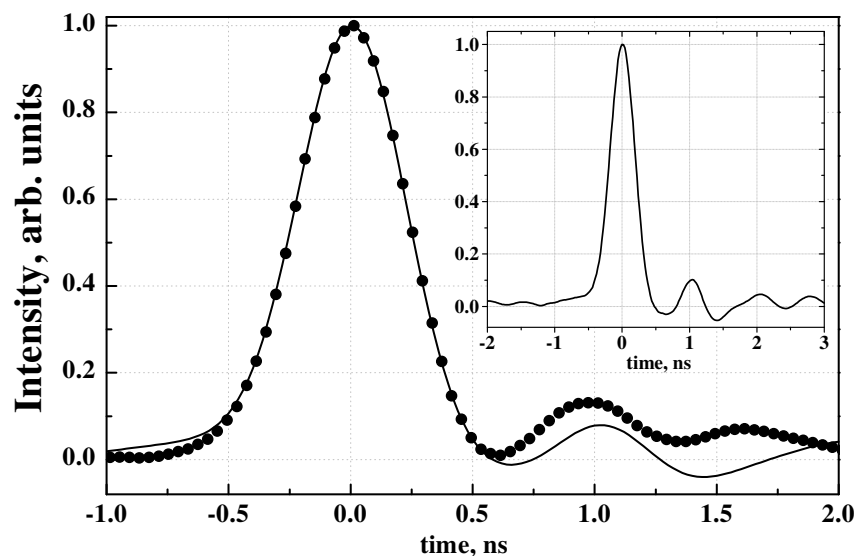


Figure 4.4. Measurement of the time duration of the amplified infrared pulses. The dots are the experimental points measured using a fast photodiode and a 1 GHz oscilloscope; the solid line is the convolution of a Gaussian profile (FWHM=300 ps) and the impulse response function of the detection system (shown in the inset).

established for the entire tuning range of the Ti:Sa laser, the I_2 saturated reference standard can be used up to 830 nm. As it is known from several studies on traveling-wave dye-amplifiers, the amplified pulses can undergo a net frequency shift with respect to the seeding light [34, 125, 127] (chirp shift). The origin of such effect is the time dependence of the gain during the amplification process, and its magnitude depends on the dye used and the wavelength position with respect to the maximum of the dye curve. In high-precision pulsed spectroscopy the chirp shift, typically on the order of 30 MHz in the visible, is the main source of systematic error. In the systems investigated in Ref.s [34, 125, 127] pulse durations were in the range 5-15 ns, and the increased peak intensities in the present system may give rise to larger frequency offsets.

The chirp shift in the laser system presented here is evaluated by simultaneously measuring the transmission through an etalon of both the seeding cw light and the amplified pulses, while scanning the Ti:Sa ring laser. The etalon (FSR = 21 GHz) used is the same one employed to measure the frequency bandwidth of the pulses. Due to the high peak intensity of the pulsed light, the two signals can not be monitored with the same photo-detector; a beam splitter is used to divide the beam transmitted through the etalon. One beam is further attenuated and sent to a fast photodiode which, in combination with a boxcar averager, measures the transmitted intensity of the pulses. The intensity of the other beam is monitored with a slow photodiode, whose signal is gated 100 μ s before the arrival of the laser pulses, thus measuring only the contribution of the cw light intensity. The frequency shift is measured at each stage of the amplification chain. It is found that the PDA induces a blue-shift in the

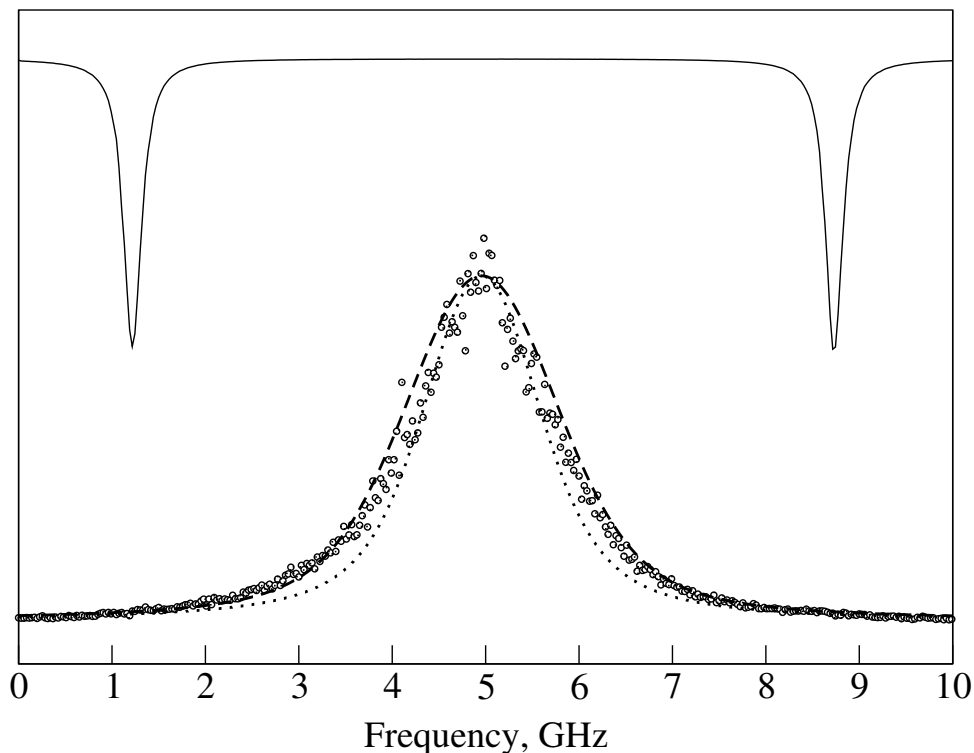


Figure 4.5. Spectral bandwidth of the powerful infrared pulses. In the lower part the transmission of the pulses when scanned through a peak of an etalon ($FSR=21$ GHz) is shown (open circles); the dashed and dotted curves are the convolution of the Airy function with a Gaussian profile with FWHM of 1.8 and 1.2 GHz respectively. In the upper part the transmission of the seeding light through a reference etalon ($FSR=7.5$ GHz) is depicted (inverted).

pulses on the order of 80 MHz, and that the amplification processes in the Ti:Sa crystals do not add any significant chirp shift. It has to be noted that these measurements are performed at a wavelength around 780 nm using LDS 765 dye in the PDA. The frequency shift could be different, even in sign, for different wavelength and dyes. However, on-line measurement of the frequency shift using the etalon is feasible, and is implemented in the system.

4.3.2 Spatial beam quality

The evaluation of the spatial beam characteristics of the powerful near-infrared pulses is of particular interest in view of their use for high-order harmonic generation. The so-called plateau of the efficiency in high-order harmonic generation in a gas jet is reached for peak intensities above 10^{13} W/cm², that can be obtained by focusing with a lens, providing the spatial quality of the pulses is sufficiently good.

The spatial distribution of the laser beam is recorded using a CCD camera (Hitachi VK-M98E). The power of the beam is attenuated with neutral density filters to avoid saturation of the camera. In Figure 4.6 (a), the beam profile at the output of the Ti:Sa amplifier at full amplification is shown. The beam has an oval shape with horizontal FWHM of 7 mm and vertical one of about 5 mm. The flat top maximum, is an indica-

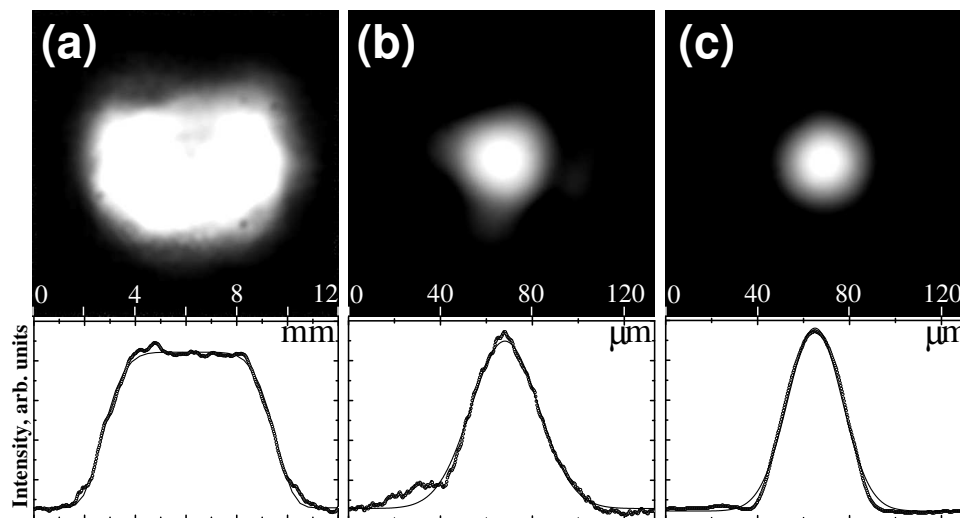


Figure 4.6. Spatial beam profiles: (a) unfocused amplified beam, FWHM=6 mm; (b) focused amplified beam ($f=20$ cm), waist=41 μm ; (c) focused cw-seeding beam ($f=20$ cm), waist=33 μm .

tion of saturation during the amplification process. By comparing the transversal beam profiles after each amplification stage we conclude that the spatial non-uniformity is induced in the main Ti:Sa amplifier. When focused with a lens of focal length $f=20$ cm, the beam has distinct vertical and horizontal foci separated by ~ 200 μm . The beam spatial distribution at the intermediate position between the vertical and horizontal foci is imaged with an objective, and shown in Figure 4.6 (b). The spot is quite symmetric with a waist $w_0=41$ μm , at the $1/e^2$ -level of the maximum intensity. The calibration of the spatial dimensions is performed using as reference two wires of 50 and 90 μm . In the lower part of Figure 4.6 (b) a Gaussian fit is performed on the transverse profile of the beam. After integration of the spatial beam profile distribution in the focus, a peak intensity of 5.2×10^{13} W/cm² is deduced, for pulses with 225 mJ of energy and 320 ps time duration. In Figure 4.6 (c) the focal spot of the seed beam is shown for comparison.

To investigate the focusing capabilities of the high-energy pulses, the beam propagation factor M^2 is estimated; M^2 is equal to 1 for a perfect Gaussian beam. When the beam is focused by a lens the M^2 factor can be evaluated, to a good approximation, using the expression $(\pi w_0 w_L)/(4\lambda f)$, [154] where w_L is the beam diameter at the lens. Assuming $w_L \sim 6$ mm, the M^2 factor of the amplified beam is estimated to be approximately 1.2. Although the focusing capabilities of the present laser beam are worse than that of a perfect Gaussian beam, power densities above 10^{14} W/cm² are feasible in case of focusing with lenses of focal lengths shorter than 15 cm. With this characteristic the present laser source is suitable to perform high-order harmonic generation in the plateau region⁵.

⁵The value of M^2 reported in Ref. [144] was overestimated by a factor of 2.

Chapter 5

Narrow-band high-order harmonic generation

Production of extreme ultraviolet (XUV) radiation by high-order harmonic generation is demonstrated to yield unprecedented spectral purity of $\lambda/\Delta\lambda = 2.5 \times 10^5$ at wavelengths covering the entire range 40-100 nm. Tunability and sub-cm⁻¹ bandwidth of the harmonics are demonstrated in recordings of the He (*1s4p*) and Ar (*3p⁵3d'*) resonance lines at 52.2 and 86.6 nm. Frequency shift of the harmonics due to chirp-induced phenomena are investigated and found to be small, resulting in a frequency accuracy of about 5×10^{-7} in the XUV-domain.

(This Chapter corresponds to Ref. [155]: Phys. Rev. Lett. **91** (2003) 163901. Figures 5.4, 5.5 and Section 5.5 have been added.)

5.1 Introduction

A key feature of the non-linear optics in the non-perturbative regime, i.e. at field intensities above 10^{13} W/cm², is the generation of a *plateau* of nearly equally intense harmonics of odd order extending to a certain *cutoff* point. An explanation for these experimental features is provided by the semi-classical and intuitive re-collision model in which the high field response is considered in three consecutive steps [66]: first the atom is ionized, then the expelled electron accelerates in the laser field and finally it recombines with the parent ion radiating one harmonic photon. The universal cutoff in high-order harmonic generation (HHG) processes exists at $E + 3.17 U_p$, with E the ionization potential of the atoms and $U_p = e^2 E^2 / 4m_e \omega_0^2$ the mean kinetic (ponderomotive) energy of a quasi-free electron quivering in the laser field in the neighborhood of the ionic core. Alternatively, non-perturbative calculations with the assumption of single-atom response (macroscopic effects ignored) confirmed results on the *plateau* and *cutoff* [68]. The characteristic features were found in early experimental studies, where laser pulses of tens of ps were used [61], as well as in studies, where fs pulses were used, giving rise to higher order harmonics (see e.g., Ref. [64]). Current activities in HHG research aim at the production of coherent short-wavelength radiation with special characteristics, that cannot be achieved by alternative sources. At the one end is the strive for attosecond pulses [156], at the other is the production of coherent light in the XUV-domain, down to x-rays in the water window [145]. The use of hollow-core fibers was shown to induce strongly enhanced harmonic yields at specific orders [4] and at the same time a greatly improved spatial coherence of the XUV output [157].

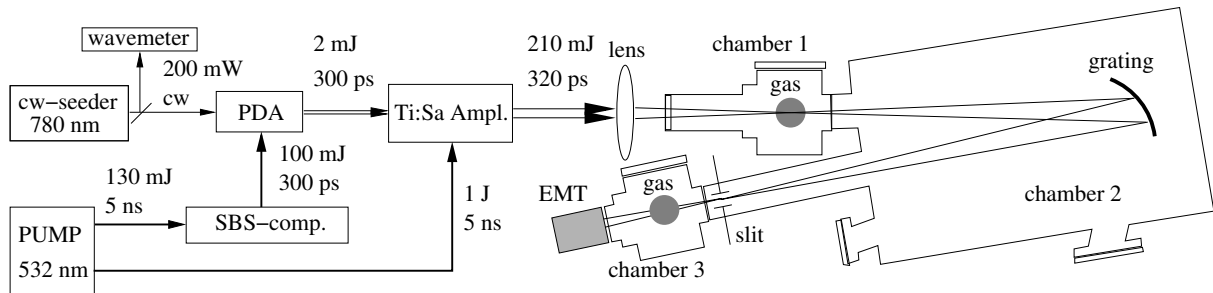


Figure 5.1. Schematic of the experimental set-up. The vacuum chambers are differentially pumped, and have a common background pressure of 2×10^{-7} mbar.

For frequency-domain spectroscopic applications the temporal coherence or spectral bandwidth of the radiation is of crucial importance. In the regime of low-order harmonics (in the perturbative regime at field intensities below 10^{12} W/cm²) coherent XUV radiation with a spectral purity of $\lambda/\Delta\lambda > 10^7$ has been demonstrated, with the use of Fourier-transform (FT) limited nanosecond pulsed lasers, for 5th harmonic [34] and for resonance-enhanced wave-mixing [46]. In contrast to these studies, in the nonperturbative regime of HHG the focus has sparsely been on achieving continuous tunability of the output radiation or on reducing the spectral purity. A noteworthy exception is a picosecond setup at Lund, producing coherent and continuously tunable XUV-radiation in the range 35-100 nm at a spectral purity of $\lambda/\Delta\lambda \sim 10^4$ [97]. That source was used to perform two-color pump-probe experiments on the $1s2p$ and $1s3p$ transitions in He at 58 and 54 nm, revealing accurate values of lifetimes and absolute photoionization cross-sections [99]. As an alternative to laser-based harmonic sources, some state-of-the-art third generation synchrotron beam lines, equipped with coherence improving undulators and high-resolution monochromators, achieve spectral purity of $\lambda/\Delta\lambda \sim 10^5$ [102, 146].

Here, we extend for the first time the HHG-regime to pulses of 300 ps duration, and demonstrate experimentally *plateau* harmonics with unprecedented bandwidth, resulting in a spectral purity of $\lambda/\Delta\lambda \sim 2.5 \times 10^5$. The high degree of coherence is combined with continuous tunability and full coverage of the wavelength range 40-100 nm. The basic concept lies in the use of well-characterized, energetic, FT-limited, wavelength-tunable laser pulses of 300 ps duration for harmonic conversion on the *plateau*. Such laser pulses are established in a novel design optical system, where compression via stimulated Brillouin scattering (SBS) is responsible for providing the 300 ps pulses, rather than mode-locking. The setup is displayed in Figure 5.1. The core of the laser system, described in detail in Chapter 4, is a three-stage traveling-wave pulsed-dye-amplifier (PDA) transforming fixed-wavelength pulses at 532 nm into FT-limited tunable pulses (bandwidth ~ 1.5 GHz) in the near-infrared wavelength range. The PDA is seeded with the light of a continuous wave (cw) Ti:Sa ring laser and its output is further amplified in Ti:Sa amplifiers. Since the frequency of the seed laser determines the frequencies further on in the optical system, its advantageous wavelength tunability performance holds for the entire setup and, via the harmonics, for the generated XUV output. Pulses of 210 mJ with 320 ps duration and 10 Hz repetition rate are produced. The performances of the laser system are demonstrated around 780 nm using LDS 765 dye in the PDA, but its operation can be extended to the entire Ti:Sa

range (700-970 nm).

5.2 Experiment and results

High-order harmonics are generated in a gas jet (Ar and Kr are used) produced with a piezo-electric valve mounted on a translational stage in a vacuum chamber. The fundamental laser pulses are focused in the jet with a 20 cm focal length lens to a spot of 40 μm in diameter, corresponding to a peak intensity of $5 \times 10^{13} \text{ W/cm}^2$. The harmonics are separated by a spherical normal incidence Au-coated grating with 1 m radius of curvature (Spectrogon, 1200 grooves/mm). The grating is used in a constant-deviation configuration (deviation angle= 11°) and the harmonics are selected with a 1mm slit. The intensity of the XUV radiation is measured with an electron multiplier tube (Electron Tubes, Model 642/2EMB).

In Figure 5.2(a) the harmonic spectrum for Ar, with 3 Bar backing pressure and the laser focused at $D=1.5 \text{ mm}$ below the valve orifice, is shown. The absolute number of harmonic photons generated per pulse, reported in Figure 5.2(b), is evaluated using the theoretical grating efficiency, the EMT first dynode (BeCu) quantum efficiency and the detector gain as specified by the manufacturers⁶. The data of Figure 5.2(b) must be considered with some caution since the reflectivity of the gold-coated grating as well as the quantum efficiency of the detector drop sharply at 40 nm. Nevertheless it may be concluded that the *plateau* of the harmonics followed by a sudden *cutoff*, the key feature of HHG, is reproduced in the present study employing much longer pulses than previously.

The harmonic photon yield is about the same as in the HHG studies employing pulses of about an order of magnitude shorter duration but same peak intensity [51, 97]. Actually, higher photon yield is expected since the peak intensity is sustained for an extended period. However, multiphoton ionization is expected to greatly reduce the neutral atom density during the 300 ps long pulse thus reducing the harmonic conversion efficiency. To evaluate the degree of ionization measurements of the photo-electron yield as a function of the laser intensities are performed. The photo-electrons are collected using a grid with positive potential placed under the gas jet, while the laser intensity is controlled using a half-wave plate in combination with a thin-film polarizer. Preliminary measurements in argon indicate an increase of the photo-electron yield for intensities up to $I \sim 3 \times 10^{13} \text{ W/cm}^2$, as shown in the inset of Figure 5.2(b). A fit on these data points indicates a power-law dependence, i.e. $\propto I^n$, with $n_{exp} = 9.6(0.5)$, which agrees with the value $n_{theo} = 10$ expected for multiphoton ionization (10 photons at 780 nm are necessary to ionize argon, $E(\text{Ar})=15.76 \text{ eV}$). At higher intensities, $I > 3 \times 10^{13} \text{ W/cm}^2$, saturation in the photo-electron yield is found. The high degree of ionization on a time-scale within the duration of the laser pulse, limits the duration of the harmonically produced XUV pulse and hence its photon yield. This cut in the time-domain would cause a broadening in the frequency domain beyond the expected bandwidth for an harmonic of a FT-limited pulse, but experimentally this additional broadening is found to be small (see below).

⁶See Section 5.5 for technical details on the measurement of the absolute number of harmonic photons.

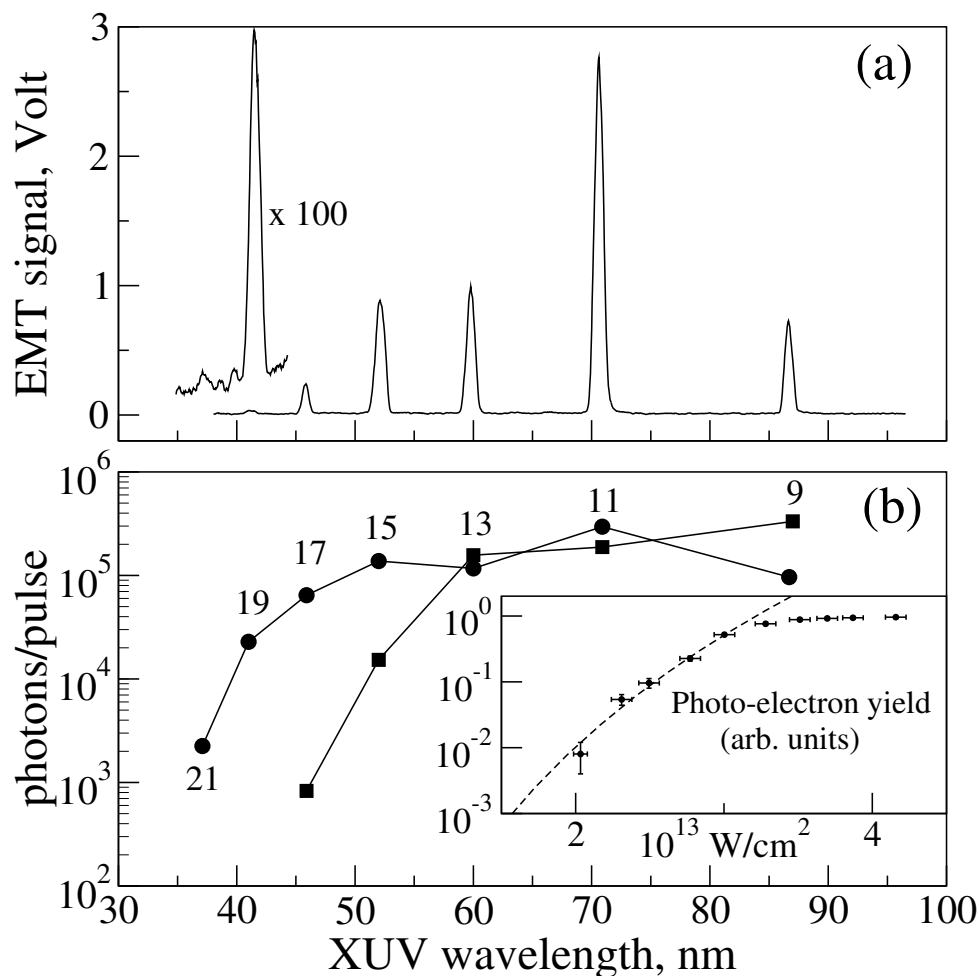


Figure 5.2. High-order harmonic generation: spectrum of the harmonics generated in argon (a); absolute harmonic yield in argon (circles) and krypton (squares) (b). The inset in figure (b) shows the photo-electron yield in argon as a function of the laser intensity: the points are the experimental data, while the dashed line is the result from a weighted power law fit performed on the lowest data points.

To investigate the frequency domain characteristics of the high-order harmonics, and also to demonstrate their applicability and continuous tunability, absorption spectroscopy is performed on known narrow atomic transitions. Using these as a ruler, the absolute frequency and the bandwidth of the XUV radiation can be deduced. Absorption is performed in a differentially pumped vacuum chamber using a pulsed jet expansion, set perpendicularly to the XUV beam in order to minimize Doppler effects. The density in the absorbing gas jet was kept such that 20-40 % peak absorption was measured. Two atomic transitions with extremely well-known transition frequencies are used: ($3p^6 1S_0 \rightarrow 3p^5 3d' [3/2]_1$) in Ar at 86.7 nm to probe the 9th harmonic generated in Kr ($\lambda_{fund}=780$ nm); ($1s^2 1S_0 \rightarrow 1s^1 4p^1 P_1$) in He at 52.2 nm to probe the 15th harmonic generated in Ar ($\lambda_{fund}=783$ nm). The frequencies of the resonance lines are taken at 3458611.6(1.5) GHz for ($3p^6 1S_0 \rightarrow 3p^5 3d' [3/2]_1$) in argon [158] and 5740807.0(1) GHz for ($1s^2 1S_0 \rightarrow 1s^1 4p^1 P_1$) in helium [159]. The level energies of argon reported by Minnhagen [158] have been confirmed by accurate laser spectroscopy

for the ($3p^6\ ^1S_0 \rightarrow 3p^54s'\ [1/2]_1$) transition at 105 nm [107]. The ionization energies of several excited states of helium calculated by Drake [159] are in agreement with experimental values within 100 MHz [34]. The present investigation is the first laser-based and sub-Doppler absorption measurement on the $4p$ resonance line of He.

5.3 Discussion

5.3.1 Absolute frequency of the harmonics

Absorption spectra in the XUV are recorded by scanning the cw ring-Ti:Sa laser, whose frequency ν is on-line monitored on a calibrated wavemeter (Atos, Lambdameter) with an absolute accuracy of 100 MHz. In principle the relation $\nu_q = q \times \nu$ gives the frequency of the q^{th} harmonic ν_q . In Figure 5.3 the absorption spectra of the argon and helium lines are shown for two valve-focus distances, $D=5$ mm and $D=1.5$ mm, which corresponds to different gas densities. The narrowest harmonics spectra are observed at $D=5$ mm, full width at half maximum 15 and 30 GHz for the 9^{th} and 15^{th} harmonic respectively. At first inspection the observed absorption resonances match the predicted frequencies extremely well, indicating that nearly exact harmonics are generated. However, the small shifts from center frequency are reproducible and significant, due to the accurate metrology performed. The central frequency of the argon transition is blue-shifted by 10 GHz, while for the helium transition no shift is observed. The spectra obtained with $D=1.5$ mm (higher gas density in harmonic conversion zone) show broadening, a few GHz additional blue-shift for the argon transition, and a few GHz red-shift for the helium transition. The observed shifts are attributed to frequency chirp, as a result of self-phase modulation of the fundamental radiation due to dynamic nonlinear susceptibility and ionization of the medium, as well as other effects inherent to the HHG process (see e.g., Ref. [96]); shifts of $> 1\%$ are typical with fs pulses at intensities of 10^{15} W/cm² [64]. In the present experiment, where longer pulses and lower intensities are employed, the chirp effect is extremely small, allowing to use HHG for precision spectroscopy in the XUV-domain.

If the chirp-induced shift effects are monitored, the absolute uncertainty in the XUV frequency calibration can, after correction, be brought to the GHz level. Frequency chirp in the amplification chain of the NIR laser system, which is measured at 80 MHz in the fundamental [144] and causing an additional shift of up to 1 GHz in the harmonic, should also be accounted for. Incorporating these frequency shifts and correcting for them, by measuring reference standards as in the present example, will allow for future spectroscopic applications employing high-order harmonics at an absolute accuracy of a few GHz, corresponding to a relative accuracy of about 5×10^{-7} .

5.3.2 Bandwidths of the harmonics

The observed widths in the recording of spectral lines, $\Delta\nu_{9,obs} = 15$ GHz for $3d'$ in Ar and $\Delta\nu_{15,obs} = 30$ GHz for $4p$ in He, can be used to estimate the bandwidth of the harmonics. Although absorption is recorded in a free-jet the Doppler width is reduced, but not to a negligible extent. Residual Doppler broadenings of 3 GHz for argon and 15 GHz for helium are estimated for an effusive thermal atomic beam with 40° opening

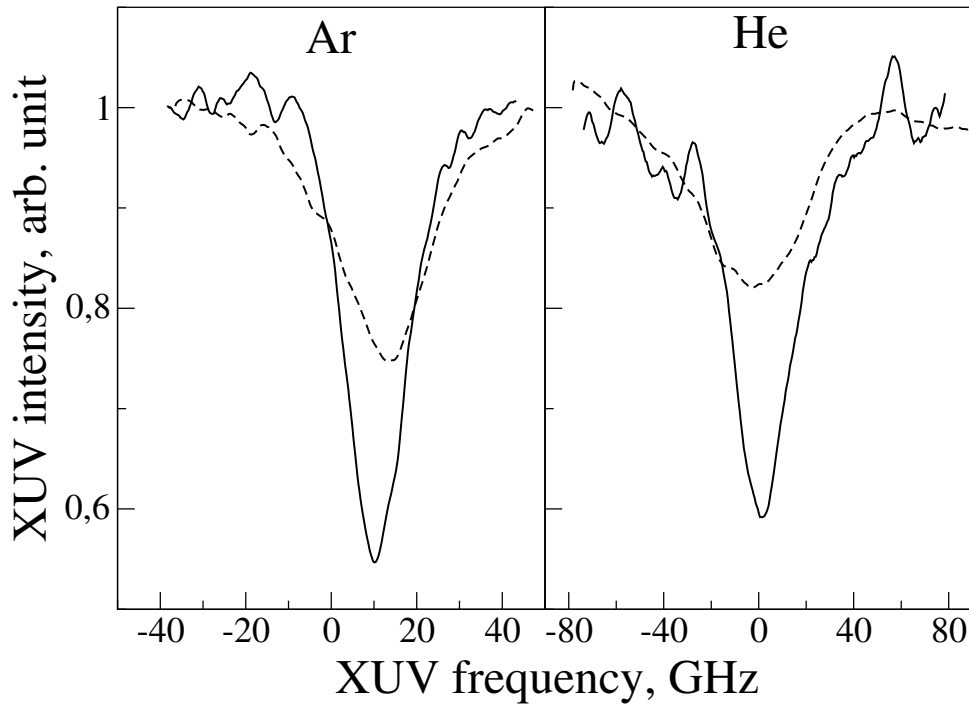


Figure 5.3. High-order harmonic spectra: on the left the spectrum of the ($3p^6S_0 \rightarrow 3p^53d'[3/2]_1$) argon transition at 86.7 nm measured with the 9th harmonic generated in krypton; on the right the ($1s^2S_0 \rightarrow 1s^14p^1P_1$) helium transition at 52.2 nm measured with the 15th harmonic generated in argon. The dashed and solid lines corresponds to measurements $D=1.5$ mm and $D=5$ mm respectively. Zero-points on the frequency axes are 3458611.6(1.5) GHz for Ar and 5740807.0(1) GHz for He.

angle, which is typical for a General Valve Series-9 pulsed solenoid valve. The effect of the XUV beam divergence is negligible. Deconvolution of residual Doppler width yields a bandwidth of $\Delta\nu_9 = 13$ GHz for the 9th, and $\Delta\nu_{15} = 20$ GHz for the 15th harmonic. In both cases this corresponds to a resolving power of $\lambda/\Delta\lambda=2.5 \times 10^5$ and the bandwidth is well below the cm^{-1} level. The expected width for the harmonics based on measurements of the width of the fundamental $\Delta\nu$ can be estimated under the assumption of a Gaussian frequency profile ($\Delta\nu_q = \sqrt{q} \times \Delta\nu$), which was measured for the frequency profile of the fundamental [144] with a width $\Delta\nu \sim 1.5$ GHz; from this we estimate for the 9th - 15th harmonics a bandwidth of 6-10 GHz. This is a factor of two lower than actually observed. The additional broadening of the harmonics is attributed to frequency chirp effects.

5.3.3 Tunability of the harmonics

Experiments are demonstrated here for fundamental wavelengths at 780-783 nm, but in principle the entire Ti:Sa tuning region of 700-970 nm can be used. In fact only the range 735-950 nm is necessary for full coverage over the 40-100 XUV region, while using successive harmonics. An example of the tunability of the XUV radiation generated with the present set-up is given in Figure 5.4 where the harmonic yield in argon is shown when the fundamental wavelength is tuned in the range 750-795 nm. The

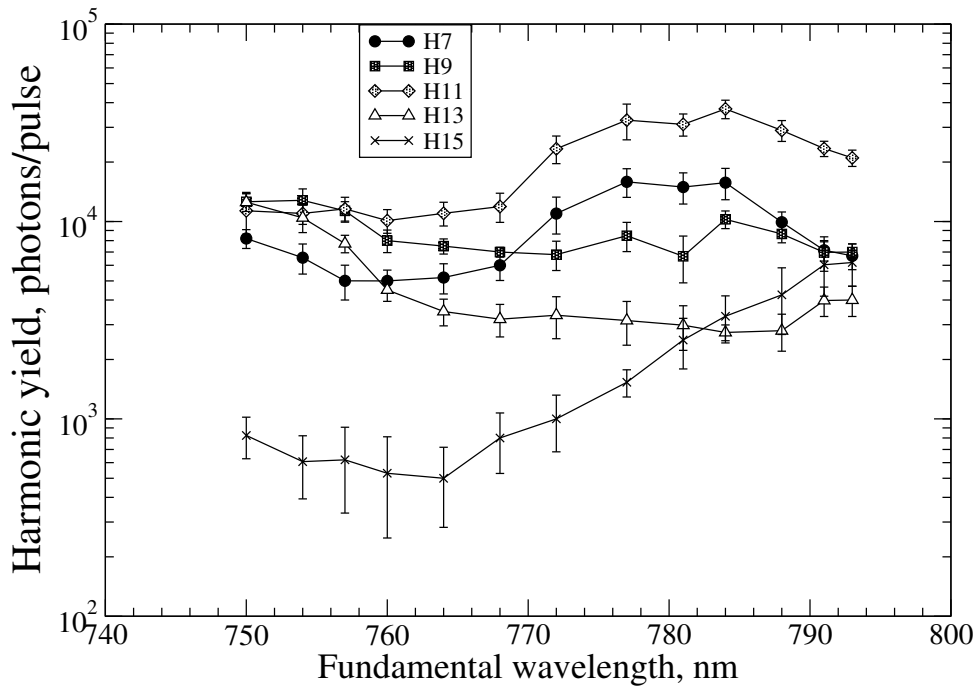


Figure 5.4. Example of the tunability of the XUV radiation generated with the present set-up: HHG yield in argon when the fundamental wavelength is tuned in the range 750-795 nm. The focal intensity is kept constant at $3.2 \times 10^{13} \text{ W/cm}^2$ while changing the wavelength.

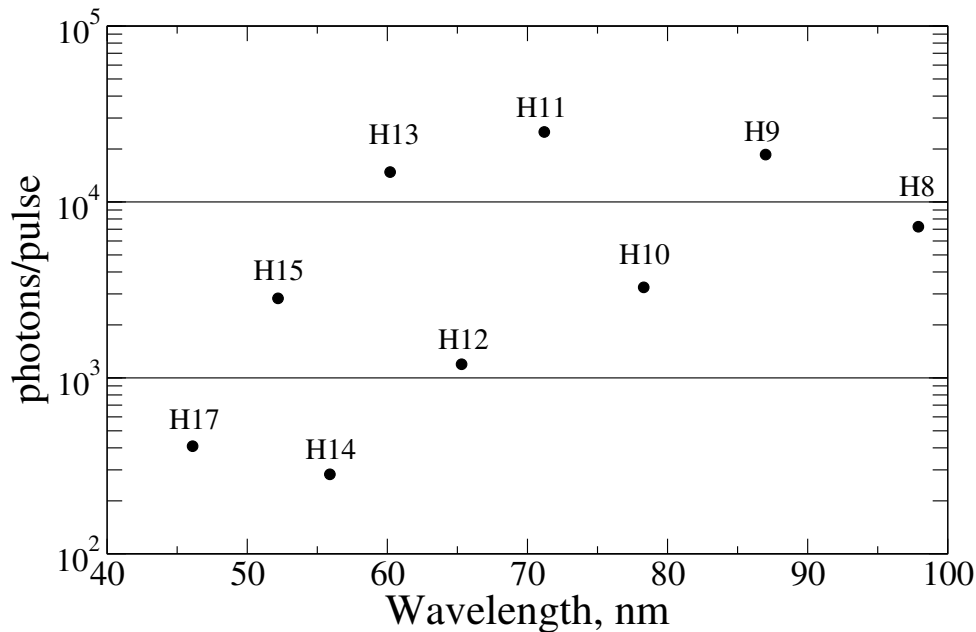


Figure 5.5. Even high-order harmonics: wave-mixing in argon of fundamental (780nm, $3.9 \times 10^{13} \text{ W/cm}^2$) and second-harmonic (390nm, $\sim 10^{13} \text{ W/cm}^2$). The second harmonic beam is produced in a 1 cm long BBO crystal, and is crossed-polarized with the fundamental one.

actual limitation in the tuning range is due to the combined effect of the response of the LDS 765 dye used in the PDA and the reflectivity of the mirrors used in the cw Ti:Sa ring laser. The behaviour of the HHG efficiency as a function of the fundamental

wavelength is reproducible and may be due to the presence of resonances and/or different phase-matching conditions between the harmonics during the HHG process in argon. A systematic investigation of this phenomenon is in progress.

In addition we have experimented with the use of even harmonics by implementing a frequency-doubling stage before the harmonic conversion in a jet. By this means we successfully produced 8th (via a wave-mixing scheme involving both fundamental and frequency-doubled output) and 10th harmonics, albeit at a slightly lower intensity, see Figure 5.5.

5.4 Conclusions

In conclusion, narrow-band continuously tunable XUV laser radiation, based on HHG is demonstrated. An unprecedented spectral purity $\lambda/\Delta\lambda$ of 2.5×10^5 , covers the entire 40-100 nm region with continuous tunability. The HHG conversion efficiency of the present source is small when compared with efficiencies of 10^{-5} - 10^{-7} achieved using fs-pulses and phase-matching in gas-filled hollow fibers [4, 157]. The use of a hollow fiber to improve the harmonic yield will be considered in future for the present setup. Chirp shift effects in HHG with 300 ps FT-limited pulses are quantified, and it is shown that a frequency accuracy of 5×10^{-7} is achieved in the XUV domain. This brings HHG into the realm of high resolution XUV spectroscopy.

5.5 Appendix: determination of the number of XUV photons

In this Appendix the method used to determine the absolute number of XUV photons produced in the HHG experiment is presented. The detection system is schematically shown in Figure 5.6. After being dispersed and selected with a diffraction grating, the high-order harmonic pulses are detected by an electron multiplier tube (EMT). The signal is acquired by a gated boxcar averager (SRS, model SR250) and stored in a personal computer (PC). The laser system, the detection system and the acquisition system are synchronized by a pulse generator (SRS, model DG535).

The EMT (Electron Tubes, model 642EM) converts the XUV photons into electrons by the photoelectric effect of the first metal (BeCu) dynode. The electron bunch is then amplified in a chain of 17 additional dynodes and collected at the anode. An

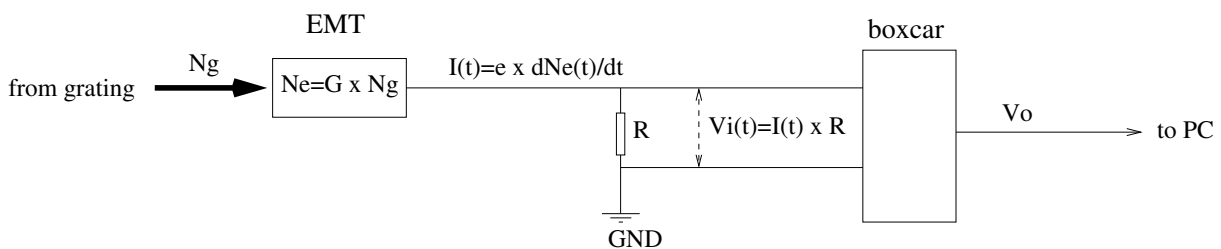


Figure 5.6. Schematic of the XUV detection system.

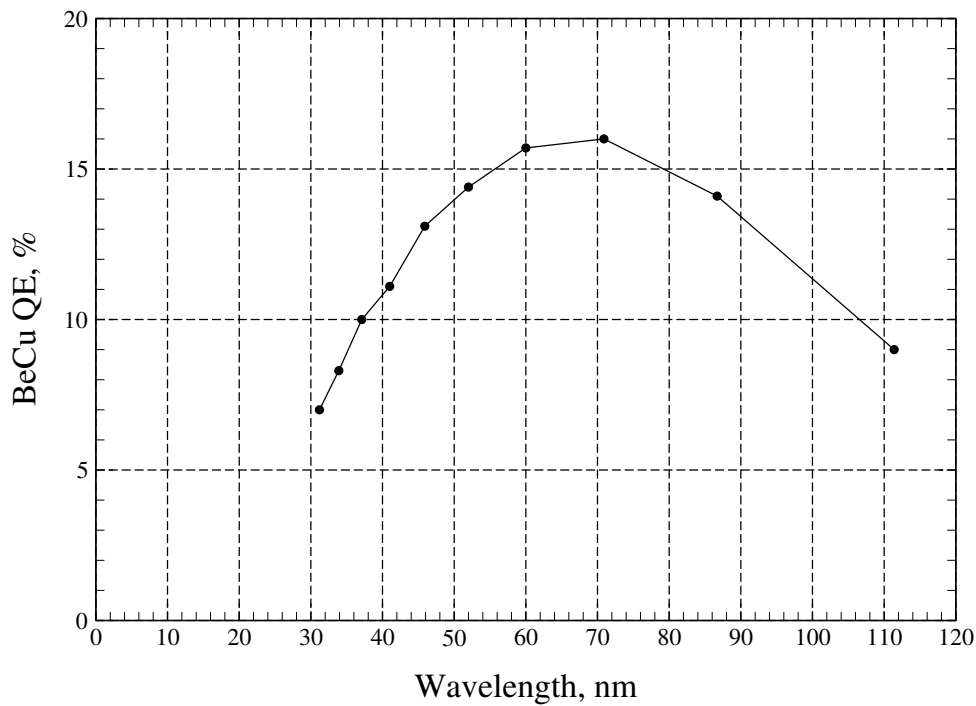


Figure 5.7. Quantum efficiency for the photoelectric effect in BeCu.

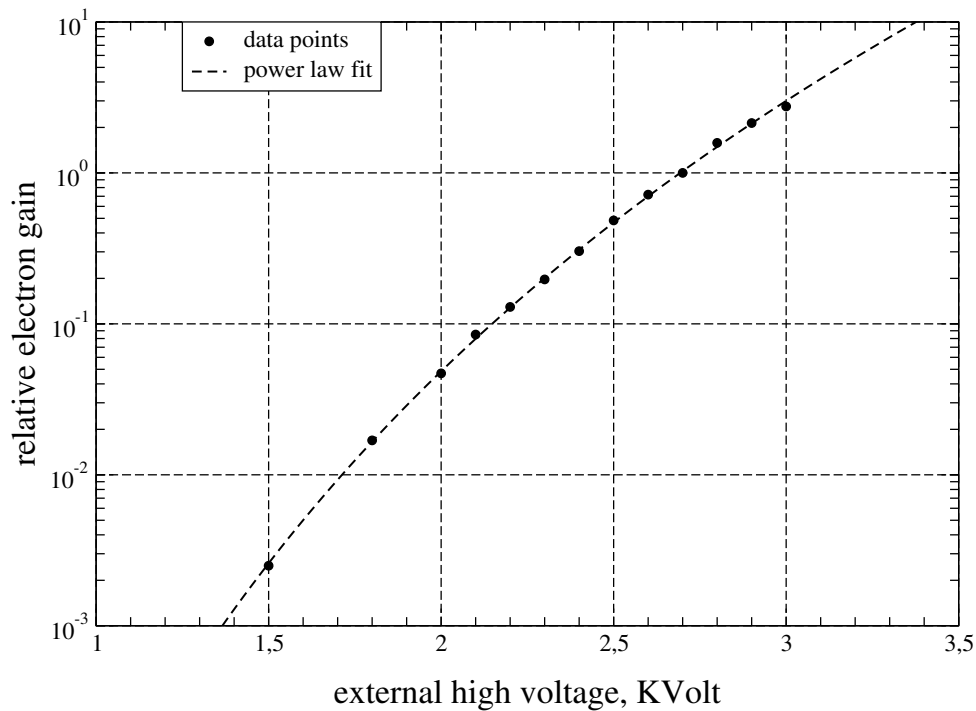


Figure 5.8. Calibration of the EMT: filled circles, measured relative electron gain, $G_{el}(V)/G_{el}(2.7kVolt)$; dashed line, power law least-squares fit.

externally applied high voltage, V , and a voltage divider provide constant tension between the dynodes. The gain coefficient of the EMT $G(\lambda, V)$, defined by the relation $N_e(\lambda, V) = G(\lambda, V) \times N_g(\lambda)$, where $N_g(\lambda)$ is the number of photons per pulse for the

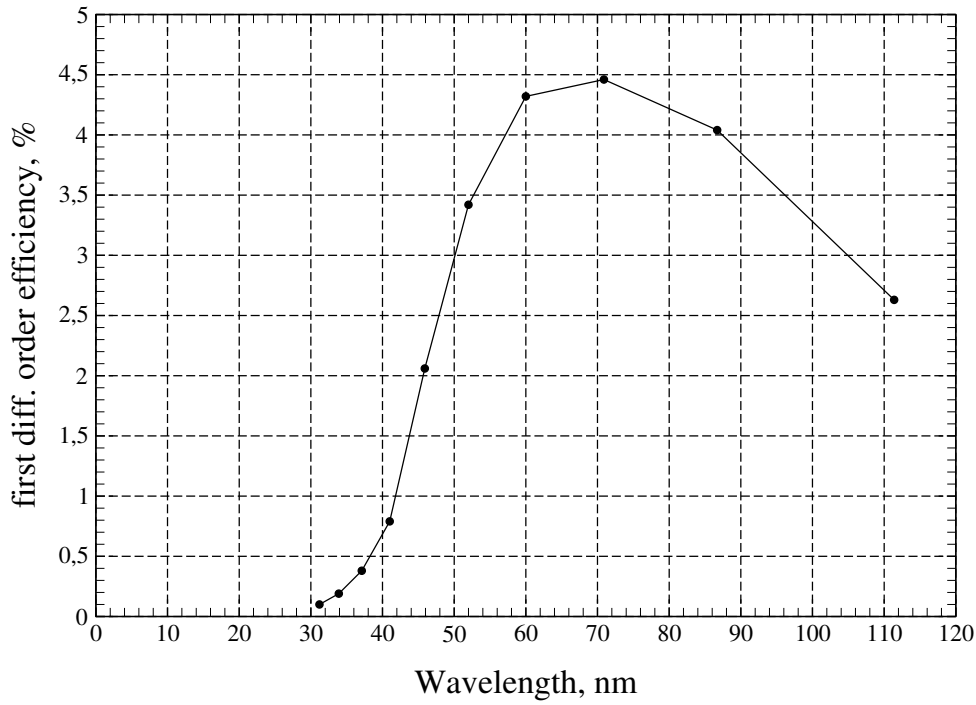


Figure 5.9. Efficiency of the first diffraction order of the normal incidence gold coated grating as specified by the producer.

selected harmonic of wavelength λ . N_e , the number of electrons collected at the anode, is given by the product of the quantum efficiency of the dynode metal $QE(\lambda)$ and the electron gain of the dynode chain $G_{el}(V)$. The quantum efficiency of BeCu as reported in the Electron Tube catalog, is reproduced in Figure 5.7. Every EMT is provided by the manufacturer with a gain calibration, which allows to estimate the electron amplification factor for an external voltage of 2.7 kV. The voltage dependence of the electron gain can then be measured relative to $G_{el}(2.7kV)$. For the actual EMT used for the measurements reported in this Chapter, $G_{el}(2.7kV) = 2.9 \times 10^6$. The measured relative electron gain, $G_{el}(V)/G_{el}(2.7kV)$, is shown in Figure 5.8, along with a power law least-square fit on the data points. From the fit, an electron gain $G_{el}(V) = 120 \times V^{10.2}$ is deduced.

The output current from the EMT is given by $I(t) = e \frac{dN_e(t)}{dt}$, where e is the (negative) electron charge and $N_e(t)$ is the electric pulse envelope, i.e. $N_e = \int_{-\infty}^{+\infty} \frac{dN_e(t)}{dt} dt$. The voltage generated across a 50Ω resistor, $V_i(t) = R \times I(t)$, is fed into the gated boxcar averager, whose dc output is the average of the input voltage in the gated time interval, ΔT ,

$$V_o = \frac{A}{\Delta T} \int^{\Delta T} V_i(t) dt, \quad (5.1)$$

where A is an amplification factor determined by the sensitivity of the boxcar. If the time interval ΔT is longer than the actual electron pulse time duration, then

$$V_o = \frac{eAR}{\Delta T} \int_{-\infty}^{+\infty} \frac{dN_e(t)}{dt} dt = \frac{eARQE(\lambda)G_{el}(V)}{\Delta T} N_g(\lambda). \quad (5.2)$$

To evaluate the total high-order harmonic photons generated in the gas jet, the

efficiency of the gold coated grating has to be taken into account. The wavelength dependent efficiency of the first diffraction order, $D(\lambda)$, as specified by the producer is plotted in Figure 5.9. The drastic decrease of the efficiency around 30 nm reflects the behavior of the reflectivity of the gold layer at normal incidence.

The absolute number of XUV photons generated in the HHG process, $N_p(\lambda)$, is given by

$$N_p(\lambda) = K(V, \lambda) \times V_o, \quad (5.3)$$

where the conversion factor,

$$K(V, \lambda) = \frac{\Delta T}{eARQE(\lambda)G_{el}(V)D(\lambda)}, \quad (5.4)$$

contains only known quantities. This estimate of $N_p(\lambda)$ is accurate within one order of magnitude due to the high number of quantities involved. Finally, it has to be noted that Eq.s (5.3) and (5.4) represent a conservative estimate of the actual number of harmonic photons generated, since the decrease with time of the performances of the EMT is a well known phenomenon in our laboratory and the grating coating gets visibly degraded after a period of use even under vacuum.

Chapter 6

High-resolution investigation of frequency chirp in HHG

In this chapter high-resolution studies of frequency chirp phenomena in HHG are reported. Due to these chirp effects the central frequency of the generated harmonic pulses may deviate from the expected value (integer multiple of the central frequency of the fundamental pulse). There are several possible sources of chirp in HHG: self-phase modulation of the fundamental pulse interacting with the gaseous medium, frequency chirp in the fundamental pulse and single-atom effects predicted by the recollision model of HHG. In the present investigation with 300 ps fundamental pulses it is demonstrated that self-phase modulation due to ionization of the gaseous medium during HHG is the major source of frequency chirp, leading to a blueshift of the central frequency of the harmonic pulses. This plasma effect is linearly dependent on the gas density. However, redshifted harmonics are also observed at low gas densities. This phenomenon may be ascribed either to plasma-dynamics effects or to chirp in the fundamental pulse. Possible experiments to investigate the origin of the frequency redshift are suggested. It is demonstrated that condition of a specific gas density can be revealed where the blueshift and the redshift compensate, producing shift-free harmonics.

6.1 Introduction

An outstanding issue in HHG, which has attracted attention in recent years, is the investigation and control of the frequency spectrum of the harmonic radiation. HHG is a coherent process and the frequency characteristics of the generated harmonics are determined by the interplay of several factors: the original frequency chirp of the fundamental pulse, the self-phase modulation of the fundamental pulse interacting with the generating medium and the intrinsic chirp phenomenon in the HHG process. Chirp is here defined as the variation of the instantaneous frequency during an optical pulse. These phenomena give rise to a broadening of the harmonic frequency spectrum as well as an effective shift in the central frequency of the harmonics, ν_q , with respect to the multiples of the fundamental frequency, $q\nu_1$. Such shifts in harmonics were first experimentally observed by Macklin *et al.* [160] and by Wahlström *et al.* [63].

The assessment of chirp-induced shifts is important in many applications in physics and chemistry when the harmonic output, preferably narrow-band and tunable, is being used as a spectroscopic tool. The chirp process in HHG is found to depend

largely on the specific conditions in the interaction region: intensity and duration of the laser pulses, gas density, single-atom response of the medium, as well as the degree of plasma formation and the energy of the electrons produced via multi-photon and tunneling ionization. When ultra-short pulses are used, the harmonics broaden or split into distinct peaks so that individual harmonics overlap and smear, even to the extent that they wash out into a short wavelength continuum [161, 162]. In a recent experimental study the phenomenon of chirp was demonstrated to be applicable for making an ultra-short pulsed laser source tunable at its harmonic frequencies ν_q [96].

It is possible to make a distinction between single-atom *versus* collective effects contributing to chirp in HHG, where the former are dominant for very short laser pulses ($\tau < 100$ fs) and the latter dominate for longer pulses ($\tau > \text{few ps}$) or for shorter pulses with intensities beyond the saturation intensity. The collective effects are related to self-phase modulation (SPM) of the fundamental pulses induced by the sudden change of the refractive index during the laser-matter interaction. This can be due both to the intensity-dependent nonlinear refractive index of neutral atoms or molecules (Kerr-effect) and to the time-dependent refractive index of the free electrons in a plasma. The single-atom effect is related to the intensity-dependent phase of the electric dipole moment induced by the intense light pulse, as predicted by the quantum mechanical description of HHG based on the strong-field approximation (SFA) model [163, 164]. There is a fundamental distinction between collective and single-atom effects: the former induces a shift on the harmonic frequency that is density-independent, while the latter is strongly density-dependent.

The effect of self-phase modulation in an intense laser pulse interacting with a gas is a well known phenomenon. SPM due to the Kerr-effect of neutrals gives rise to a redshift in the rising edge and a blueshift in the falling edge of the pulse. When the laser intensity is high enough to photoionize the gas, a plasma is formed and the index of refraction is dominated by free electrons as described by Yablonovitch [165]. The increase in the free electron density occurring during the laser pulse induces a frequency blueshift. It should be noted that SFM occurs at the fundamental frequency ν_1 and then effects the harmonic frequency ν_q via the relation $\nu_q = q\nu_1$. When relatively long pulses are used ($> \text{few ps}$), the plasma dynamics starts to play an important role. Free electrons can escape the focal region [166] or recombine with ions, thus leading to a decrease in the electron density during the laser-plasma interaction and hence contribute to a frequency redshift.

An experimental investigation of the chirp due to the single-atom effect in harmonic generation, also referred to as nonadiabatic or dynamic chirp, was performed by Shin *et al.* [167, 168] uncovering its dependence on various parameters. It was found experimentally that the effect of a non-adiabatic blueshift is dominant for short pulses (< 100 fs) exhibiting a sharp rise of the electric field. Also it was confirmed that there is only a marginal dependence on density, proving that a single-atom effect is at stake. Similar dynamic chirp effects, occurring in competition with SPM, were investigated by Kim *et al.* [79]. The competition between all chirp inducing phenomena as well as the possibility to apply chirp on the incident laser frequency ν_1 can be used to optimize and control the harmonic photon yield [162].

In the present study a new window is opened for investigation of the chirp phenomenon in HHG. As discussed in Chapter 5, harmonic generation in the non-pertur-

bative regime is demonstrated to be feasible at pulse durations as long as 300 ps [155] and the same setup is now employed to quantitatively address chirp-induced shifts in the 9th and 13th harmonic. The relatively long pulse duration ($10^3 - 10^4$ times longer than in experiments employing fs pulses), the associated narrow bandwidth, and the possibility of continuous wavelength scanning allow for precision metrology studies of the chirp phenomenon using well-calibrated atomic resonances as frequency markers in the extreme-ultraviolet. Previously, in studies employing femtosecond pulses fractional frequency shifts $\Delta\nu/\nu$ in the order of a few % were observed. Under conditions of longer pulses the rate of change of the refractive index is much smaller and hence the expected chirp much less. However the unique metrology setup in our laboratory, with a continuously tunable high-power laser source, allows for registration of such small chirp effects at the $10^{-6} - 10^{-7}$ level.

6.2 Experimental setup and procedure

The experimental apparatus, formed by the laser system providing the tunable fundamental pulses, and the setup for high-order harmonic generation, detection and absorption is presented in Chapters 4 and 5. In the following a description of those properties of importance for the chirp shift measurements are given. A schematic of the experimental apparatus is shown in Figure 6.1. The tunability of the combined set of lasers and amplifiers is determined by that of the continuous wave Ti:Sa ring laser. It may be scanned mode-hop free over a limited range of about 1 cm^{-1} , and it can be set at wavelengths between 750 nm and 800 nm without changing the mirror set. The pulsed-dye-amplifier (PDA), running on LDS-765 (Exciton) dye, allows for coverage of the wavelength range 750-795 nm. The three stage PDA, which is pumped by the compressed pulses (300 ps, 532 nm) from a 1 m long Brillouin cell filled with clean water determines the spectral and temporal properties of the energetic near-infrared (NIR) laser pulses; they follow the time duration of the pump pulse and have a nearly Fourier-transform limited bandwidth ($\sim 1.5 \text{ GHz}$). For the present experiments a 1 cm long Brewster-cut Ti:Sa cylindrical crystal with a diameter of 1 cm was used in the multipass amplifier. The size of pump and seed beam are reduced compared with previous experiments, where an anti-reflection coated plane-parallel crystal was used. As a result the pump energy is also reduced in order not to damage the mirrors in the multipass amplifier. The maximum NIR pulse energy is 150 mJ. The energy of the pulses used for HHG is controllable by means of a variable attenuator formed by a half-wave plate and a thin-film polariser. The spatial beam quality is investigated using a beam profile analyser (DataRay, Model:WinCamD) and a propagation factor of $M^2 = 1.2$ is found. This agrees with the value obtained with the previous amplifier configuration (see Section 4.3.2), indicating that the spatial characteristics of the energetic near-infrared pulses generated by the laser system are almost entirely determined by the TEM₀₀ cw seeding beam. The diameter of the NIR beam at the output of the amplifier is about 6 mm. In order to achieve high intensities needed for HHG a relatively strong focusing is employed using an anti-reflection-coated lens with 15 cm focal length, and allowing for a focal spot intensity of about $5 \times 10^{13} \text{ W/cm}^2$. The confocal parameter of the focused beam is about 1.8 mm.

Harmonics are produced in a freely expanding pulsed gas jet at about 0.5 mm

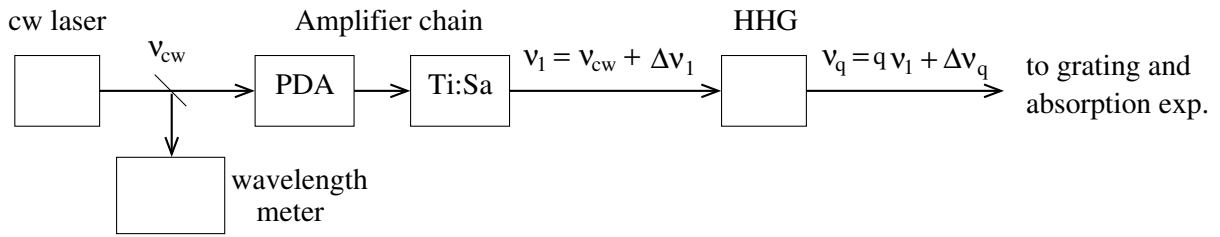


Figure 6.1. Schematic picture of the experimental apparatus.

downstream from the orifice of a piezo-electric pulsed valve with 1 mm opening diameter. The gas jet diameter in the interaction region is about as long as the confocal parameter of the fundamental focused beam. The valve follows the design described in Ref. [169]. Both the backing pressure for the valve and the running pressure in the differentially pumped vacuum chamber are monitored and found to be linearly dependent for a backing pressure in the range 0.5 – 4 bar, with a running pressure in the vacuum chamber in the range 10^{-6} – 10^{-5} mbar. This corroborates the finding reported in [169] that the gas flow varies linearly with the gas backing pressure. In view of this, the backing pressure is assumed to be, with good approximation, a relative measure for the density in the focal region. With a voltage of about 230 Volt on the piezo-electric valve the gas density in the interaction region is estimated to be around $3 \times 10^{17} \text{ cm}^{-3}$ (~ 10 mbar) for a backing pressure of 1 bar.

Of crucial importance for the here reported experiments is the determination of frequencies, at the fundamental as well as at the harmonics. In Figure 6.1 the relevant frequencies involved are shown. For the fundamental frequency accurate wavelength determinations are performed using a wavelength meter (ATOS, Model:LM-007), equipped with four etalons to measure the seeding frequency ν_{cw} of the cw Ti:Sa laser. During the course of the investigations the wavelength meter is re-calibrated several times in measurements on I_2 hyperfine components [124] and each time the calibration was found within 50 MHz, thus setting the uncertainty limit to the calibrated frequencies of the cw seeding light.

In a pulse-amplification system using fluorescent dyes the central frequency of the output pulses is known to undergo effective shifts with respect to the seed-frequency. This is a chirp phenomenon originating from the time-dependent gain in the dye amplifier [126, 127]. The effective net-shift between the seeding frequency and the central frequency of the amplifier output pulses can be determined from transmission profiles of both beams through an etalon, as described in the appendix in Section 6.6. In a previous measurement the effective chirp shift was found to be about 80 MHz (blueshift) for a wavelength of $\lambda_{cw} = 780$ nm. In view of the importance of this value for the analysis of the harmonic chirp the measurements are redone in the present campaign at various wavelengths. The effective frequency shift between cw seed and the amplifier output frequencies, $\Delta\nu_1(\lambda_{cw}) = \nu_1 - \nu_{cw}$, measured in the range 750-790 nm is shown in Figure 6.2. It was verified that the chirp effect in the Ti:Sa amplifiers is negligible; this is related to the fact that relaxation response time in Ti:Sa (μs timescale) is much longer than in dye (ps timescale). The frequency shift $\Delta\nu_1(\lambda_{cw})$ has an almost linear dependence on the wavelength with a negative slope and a zero crossing at $\lambda_{cw} \sim 770$ nm, which is close to the maximum of the dye gain curve at about 765 nm. This

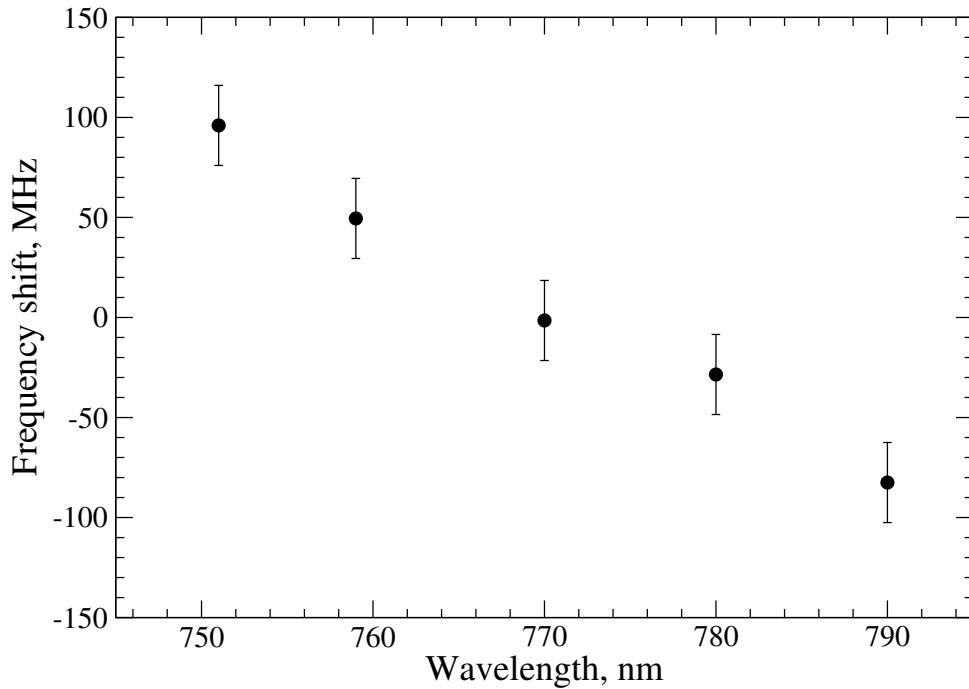


Figure 6.2. Measured frequency shift induced by the amplifier system formed by a pulsed-dye-amplifier, a single-pass Ti:Sa preamplifier and a four-pass Ti:Sa power-amplifier: shift of the central frequency of the output pulses with respect to the frequency of the input cw seeding light.

indicates that chirp-free pulses are produced at a certain wavelength around 770 nm. Chirp-free denotes here the absence of a net-shift between the cw-seed frequency and the central frequency of the laser pulses at the output of the amplifier chain. However, it is well conceivable and expected that frequency excursions higher than the measured net-shift occur during the 300 ps duration of the laser pulses. The particular behavior of a wavelength-dependent chirp over the gain profile of the dye was already found and explained in ns pulsed-dye amplifiers [126, 127]. It has to be noted that the measured shift at 780 nm is about 30 MHz to the red, almost 100 MHz away from the previously measured value of 80 MHz to the blue. This discrepancy is most probably due to a misalignment in the previous measurement setup between the seeding and the amplified beam which can lead to an *apparent* blueshift, as discussed in the appendix in Section 6.6.

In order wavelength-dependent net-shift in the amplifier is accounted for in the determination of the center frequency ν_1 of the near-IR fundamental beam. The central frequency of the fundamental pulses used for the HHG experiment then relate to the calibrated frequencies as: $\nu_1 = \nu_{cw} + \Delta\nu_1(\lambda_{cw})$. An assumption must be made as to how the chirp in the fundamental affects the harmonic frequencies. Since it is not possible to determine the time-dependent frequency excursions during the fundamental pulse of 300 ps duration, as it was demonstrated for ns pulses in Ref. [34], the approximation is made that the net-shift in the central frequency of the fundamental pulse reflects in a proportional way in the harmonic frequencies. Hence we assume

the expected harmonic frequencies to be,

$$\nu_q^e = q \times [\nu_{cw} + \Delta\nu_1(\lambda_{cw})]. \quad (6.1)$$

The fact that harmonics are produced in a certain time window within the fundamental pulse envelop, in which the frequency of the fundamental pulse may be different, is neglected in the subsequent analysis.

In order to determine the shifts as a result of chirp in the HHG process the expected harmonic frequencies ν_q^e will be compared with the actual observed frequencies in the extreme ultraviolet. For this purpose absorption spectra are measured of well calibrated atomic resonances: the ($3p^6\ ^1S_0 \rightarrow 3p^5 3d'[3/2]_1$) transition in Ar at frequency $\nu_{Ar} = 3\,458\,611.8$ GHz or roughly 86.7 nm ($\lambda_{cw} = 780$ nm) and the ($1s^2\ ^1S_0 \rightarrow 1s2p\ ^1P_1$) transition in He at frequency $\nu_{He} = 5\,130\,495.083$ GHz or 58.4 nm ($\lambda_{cw} = 759$ nm). For the argon atom the level energies of electronically excited states are all known to high relative accuracy and it is only the level energy of the ground state that introduces uncertainty. Through the measurement of the ($3p^6\ ^1S_0 \rightarrow 3p^5 4s'[1/2]_1$) transition by Velchev *et al.* [107] the absolute accuracy of all VUV transitions in Ar [158] is established to be within 1.5 GHz. In particular, for the presently used transition in Ar a lower uncertainty of about 0.3 GHz can be inferred using the data reported in Table VI in Ref. [158]. In He the $1s2p$ resonance line was measured to extremely high accuracy (45 MHz) by Eikema *et al.* [34] in agreement with the theoretical calculation in Ref. [159].

Figure 6.3 shows absorption by Ar and He of the 9^{th} and the 13^{th} harmonic respectively recorded by scanning the cw-seed frequency. The resonances are plotted on a scale of the frequency $q\nu_{cw} - \nu_{atom}$ as derived from the wavelength meter, ν_{cw} , and the transition frequency in the absorbing gas, ν_{atom} . Thus, no correction for the frequency chirp in the amplification process is performed on the data shown in Figure 6.3. The solid lines present the results of least-squares fits on the data points with a Gaussian profile, whose centers then determine the chirp shift associated with the HHG process. Note that a redshift in the present graphs represent an actual blueshift of the harmonic frequency, and *vice-versa*. The width of the absorption resonances is a combined effect of Doppler broadening in the free gas jet and the bandwidth of the harmonic. However, most absorption profiles are recorded with about 50% absorption, thus saturation effects are not negligible and a systematic investigation of the broadening of the spectral profile is not performed. For those measurements below saturation a 15 GHz width for the argon resonance at the 9^{th} harmonic, and a 30 GHz width for the helium resonance at the 13^{th} harmonic are observed. Assuming an opening angle for the free jet expansion of $\theta = 40^\circ$ (typical for the solenoid valve used for the absorbing gas jet), a gas speed (v) of 1200 m/s and 400 m/s for He and Ar respectively, the Doppler contribution, given by $\Delta\nu_D = (v/c)\nu \sin \theta$, is 13 GHz and 3 GHz at the 13^{th} and 9^{th} harmonic respectively.

6.3 Results and interpretation

Absorption spectra of the argon and helium resonances are recorded using the 9^{th} and 13^{th} harmonics generated in various gases at different values of the gas backing pres-

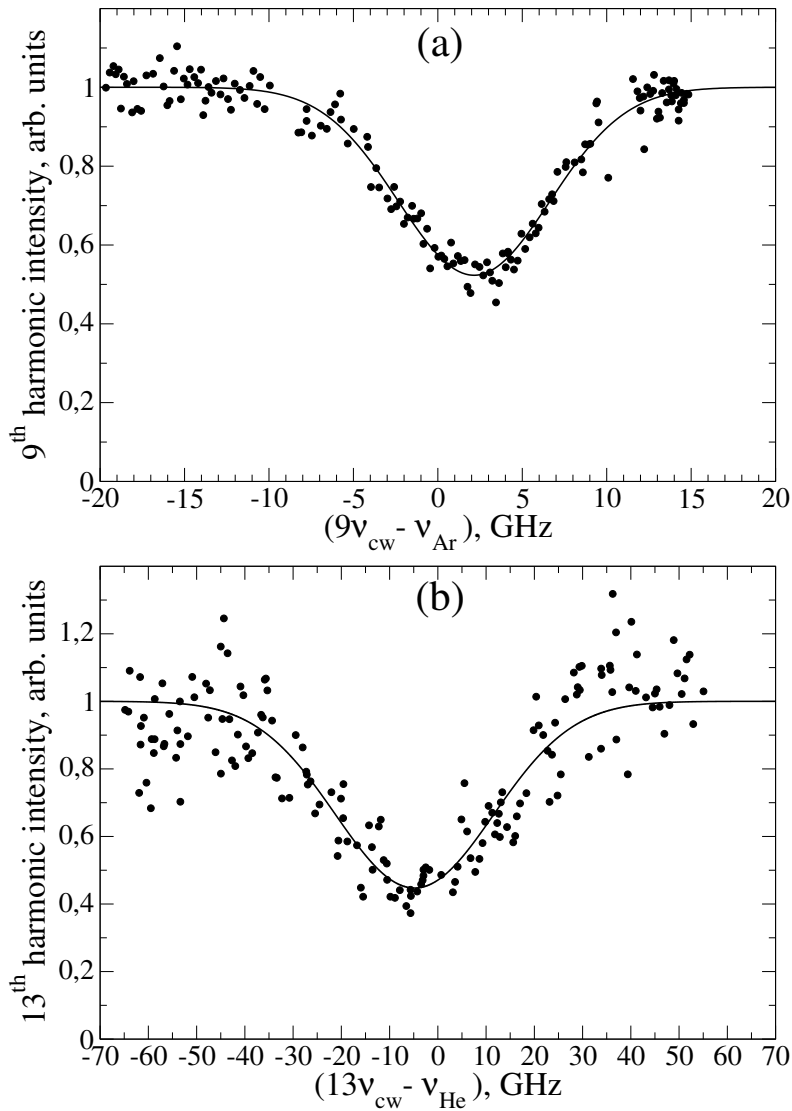


Figure 6.3. Frequency metrology on the generated harmonics: (a) spectral recording of the $(3p^6\ ^1S_0 \rightarrow 3p^53d'\ [3/2]_1)$ transition in Ar at 86.7 nm with the 9th harmonic produced in N₂ at 1.2 bar backing pressure ($\lambda_{cw} = 780$ nm); (b) spectral recording of the $(1s^2\ ^1S_0 \rightarrow 1s2p\ ^1P_1)$ transition in He at 58.4 nm with the 13th harmonic produced in N₂ at 1.4 bar backing pressure ($\lambda_{cw} = 759$ nm).

sure of the piezo-electric valve. The shift of the observed *versus* expected central frequency of the harmonic spectrum is determined as $\Delta\nu_q = \nu_{atom} - q(\nu_{cw} + \Delta\nu_1(\lambda_{cw}))$, thus correcting for the net frequency shift that occurs in the light amplification system. The frequency corrections are, $9\Delta\nu_1(780\text{ nm}) = -270$ MHz and $13\Delta\nu_1(759\text{ nm}) = 650$ MHz for the 9th and 13th harmonics respectively (see Figure 6.2).

In Figure 6.4 the shifts of the 9th harmonic generated in Xe, Kr and N₂ at a peak intensity of 4.3×10^{13} W/cm² are shown along with linear least-square fits on the data points. The shifts increase linearly with gas density and the resulting slopes decrease with increasing ionization potential ($E(\text{Xe}) = 12.1$ eV, $E(\text{Kr}) = 14.0$ eV and $E(\text{N}_2) = 15.6$ eV). The saturation intensities for the varous gases, calculated using

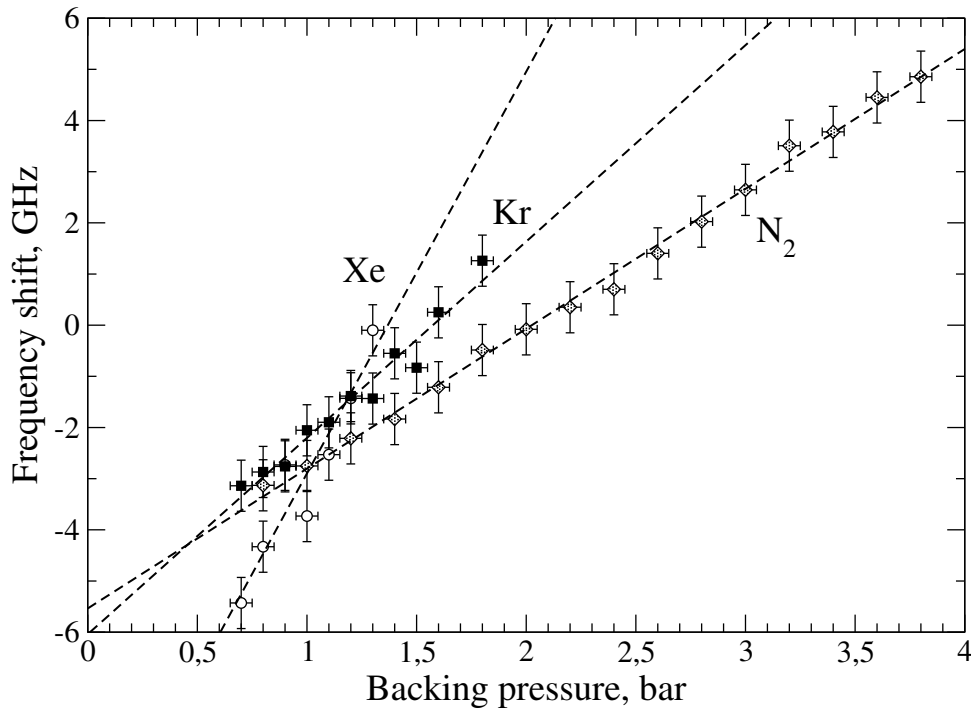


Figure 6.4. Frequency shift of the 9th harmonic produced in Xe (circles), Kr (squares) and N₂ (diamonds) at $4.3 \times 10^{13} \text{ W/cm}^2$ as a function of the backing pressure of the valve. Along the vertical axis the deviation of the central frequency with respect to the expected transition frequency. Also shown are the results of linear least-squares fits (dashed lines).

Eqs. (1.11) and (1.12), are: $I_s^{cal}(\text{Xe}) = 1.1 \times 10^{13} \text{ W cm}^{-2}$, $I_s^{cal}(\text{Kr}) = 2.6 \times 10^{13} \text{ W cm}^{-2}$ and $I_s^{cal}(\text{N}_2) = 4.7 \times 10^{13} \text{ W cm}^{-2}$. The measurements of the ion yield *versus* laser intensity, performed with a grid placed downstream the gas jet, result in saturation intensities of $I_s^{exp}(\text{N}_2) \sim 3.5 \times 10^{13} \text{ W cm}^{-2}$, $I_s^{exp}(\text{Kr}) \sim 2.5 \times 10^{13} \text{ W cm}^{-2}$ and $I_s^{exp}(\text{Xe}) \leq 10^{13} \text{ W/cm}^2$, in good agreement with the calculated values. Since the peak intensity of $4.3 \times 10^{13} \text{ W/cm}^2$ is above the saturation intensities for all the gases used in the experiment, complete ionization is achieved during the pulse. The linear rise of the harmonic frequency shift with density is consistent with a blueshift originating from plasma formation, as will be discussed in detail in Section 6.4. Moreover, the rate of ionization increases with decreasing ionization potential, which explains the trend of the slopes. To check the influence of ionization in the observed shift, the same measurements are repeated for Xe and Kr at an intensity of $1.4 \times 10^{13} \text{ W/cm}^2$, which is above the saturation intensity for Xe but below the saturation intensity of Kr. In Figure 6.5 the results are shown and the different behavior of the two gases is evident. For xenon there is a linear increase of the frequency shift with increasing gas density, indicating that a strong plasma effect is still present. On contrary, for krypton the shift is almost density-independent, which is consistent with a low degree of ionization.

The most striking feature arising from Figures 6.4 and 6.5 is the negative frequency shift (*redshift*), present for all gases at low gas densities. This redshift offset shows an intensity dependent trend, it increases in magnitude with increasing intensity. The intensity dependence of the negative frequency shift offset is investigated in Xe at low backing pressure ($\sim 0.5 \text{ bar}$) and the results are reported in Figure 6.6. The large un-

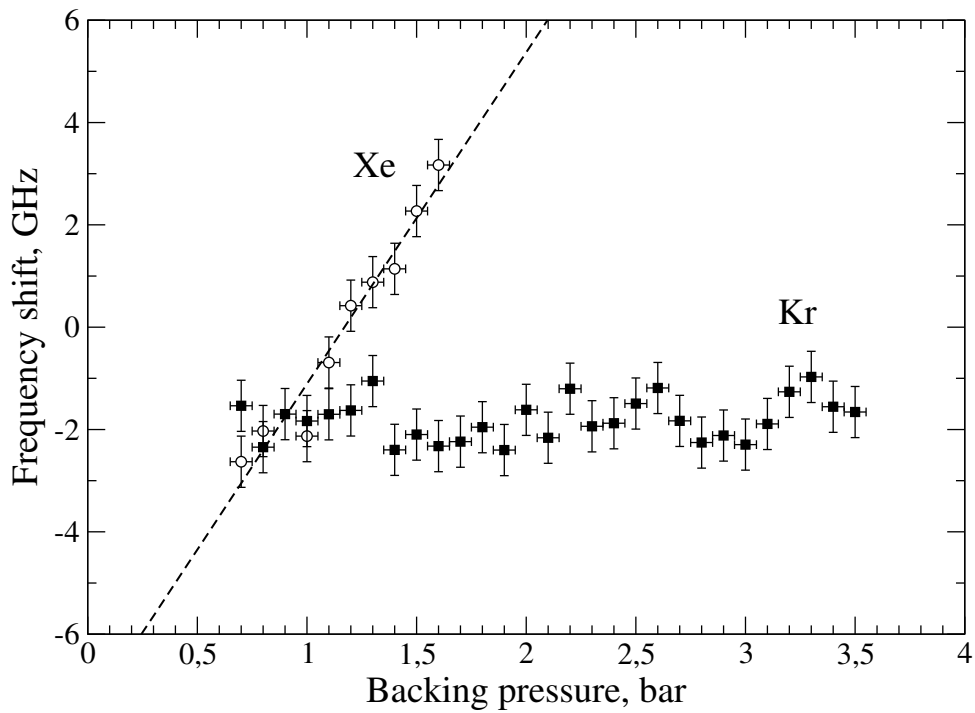


Figure 6.5. Frequency shift of the 9th harmonic produced in Xe (circles) and Kr (squares) at $1.4 \times 10^{13} \text{ W/cm}^2$ as a function of backing pressure of the valve. Along the vertical axis the deviation of the central frequency with respect to the expected transition frequency. Also shown is the result of a linear least-square fit (dashed line).

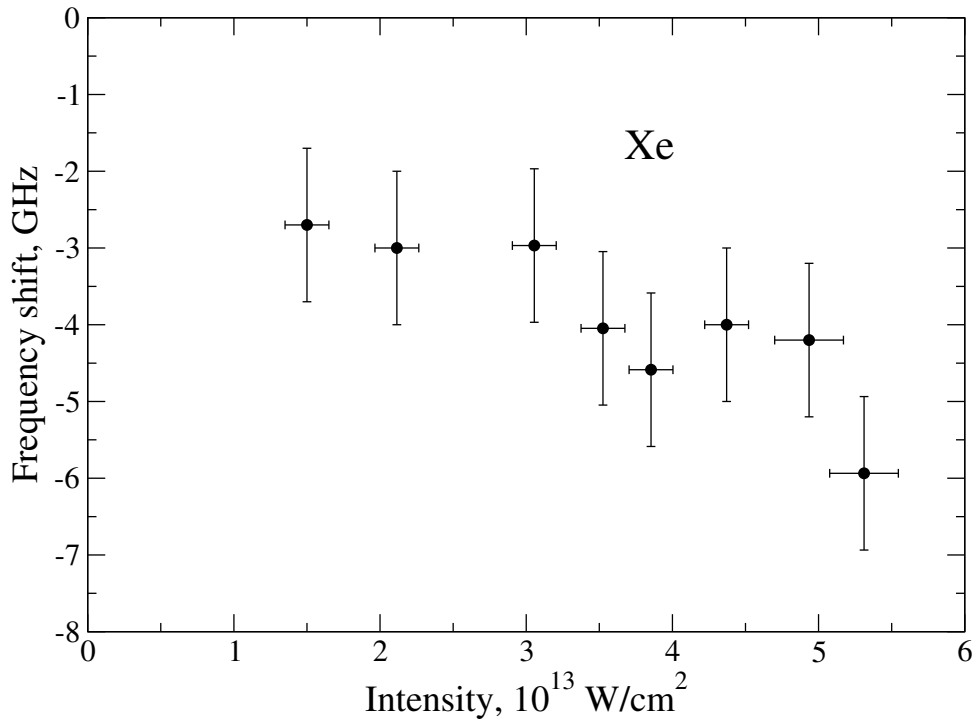


Figure 6.6. Intensity dependence of the redshift observed in xenon. The backing pressure is 0.5 bar

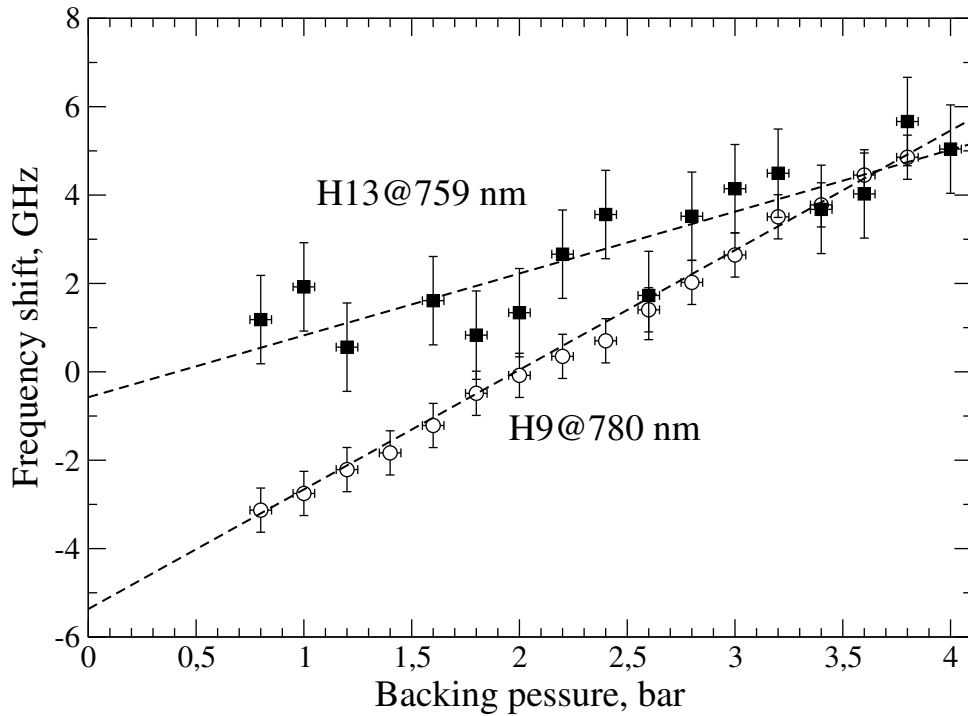


Figure 6.7. Frequency shift of the 13th (H13, $\lambda_{cw} \sim 759$ nm) and 9th (H9, $\lambda_{cw} \sim 780$ nm) harmonic produced in N_2 as a function of the valve backing pressure. Along the vertical axis the deviation with respect to the expected transition frequency. Also shown are the results of linear least-square fits (dashed lines).

certainty on the data points, due to the low number of harmonic photons generated at low gas density, limits the possibility of a quantitative analysis. However, the increase of the redshift offset with increasing laser intensity is qualitatively confirmed by this measurement.

To investigate the order dependence of the harmonic shift, measurements are performed for the 13th harmonic produced in N_2 with an intensity of 4.3×10^{13} W/cm². Here the ($1s^2\ ^1S_0 \rightarrow 1s2p\ ^1P_1$) helium resonance at 58.4 nm ($\lambda_{cw} \sim 759$ nm) is used as a frequency ruler. The results are shown in Figure 6.7, where the frequency shifts measured for the 9th harmonic (see Figure 6.4) are also shown for comparison. The frequency shift of the 13th harmonic also increases linearly with the gas density, indicating that the plasma effect dominates the chirp induced net frequency shift in the harmonics. However, the linear least-squares fit on the data points gives a slope that is almost a factor of two smaller than the slope for the 9th harmonic. Since the plasma effect acts through SFM on the fundamental beam one would expect a linear increase of the slope with increasing harmonic order. The observed behavior seems to indicate that the 13th harmonic is actually produced in a time interval during the pulse when the ionization rate is smaller compared to the ionization rate present when the 9th harmonic is produced. No redshift offset is observed for the 13th harmonic at low gas density.

6.4 Discussion

The observed net frequency shifts confirm the presence of chirp phenomena during the HHG process. In the following the major sources of frequency chirp are discussed and estimates of the expected shifts are given and compared with the experimental results.

Collective effects Chirp phenomena related to collective or macroscopic effects are due to the rate of temporal change of the refractive index in the nonlinear medium. A time-dependent index of refraction induces a time-dependent phase on the incident beam propagating through a length L given by

$$\phi(t) = -\frac{2\pi\nu_0}{c} \int^L n(z, t) dz, \quad (6.2)$$

where ν_0 is the light frequency. Here z is the spatial coordinate along the propagation axis of the laser beam. The resulting variation in phase gives a frequency shift via:

$$\Delta\nu(t) \equiv \nu(t) - \nu_0 = \frac{1}{2\pi} \frac{\partial\phi(t)}{\partial t} = -\frac{\nu_0}{c} \int^L \frac{\partial n(z, t)}{\partial t} dz. \quad (6.3)$$

Based on this effect of SPM of the incident laser pulse at frequency ν_1 a chirp is imposed on all of the harmonics.

High-order harmonic generation is accompanied by ionization of the medium, resulting in a fully ionized plasma at the highest intensities. In a plasma the index of refraction is governed by the free electrons: $n^{el}(\nu, z, t) = [1 - (\nu_p(z, t)/\nu)^2]^{1/2}$ where $\nu_p^2 = e^2 N_e(z, t) / 4\pi^2 m_e \epsilon_0$ is the time dependent electronic plasma frequency and $N_e(z, t)$ the electron density. Plasma formation causes blueshifts in the harmonic frequencies because $N_e(z, t)$ increases during the HHG process. At electron densities typical in HHG experiments ($N_e \ll 10^{21} \text{ cm}^{-3}$) the plasma frequency is much smaller than the laser frequency and the blueshift in the harmonic radiation can be estimated using Eq.(6.3),

$$\Delta\nu_q^{el}(t) = \frac{qe^2}{8\pi^2 cm_e \epsilon_0 \nu_1} \int^L \frac{\partial N_e(z, t)}{\partial t} dz. \quad (6.4)$$

Under conditions of saturation of the photoionization process and assuming a homogeneous medium, the rate $\partial N_e(z, t) / \partial t$ can be approximated by N_0 / τ , where N_0 is the initial atomic density and τ the laser pulse duration. This predicts a blueshift which is linearly dependent on the gas density in the focal region given by

$$\Delta\nu_q^{el} = \frac{qe^2 L}{8\pi^2 cm_e \epsilon_0 \nu_1} \frac{N_0}{\tau}. \quad (6.5)$$

Wahlström *et al.* [63] experimentally observed blueshifted harmonics from a 150 fs fundamental pulse which were explained by the plasma effect.

An estimate of the blueshift due to the plasma can be performed using Eq. (6.5) with $L = 1 \text{ mm}$, $\nu_1 = 4 \times 10^{14} \text{ Hz}$ and $\tau = 300 \text{ ps}$ which lead, for the 9th harmonic generated in a fully ionized gas of pressure 10 mbar ($N_0 \sim 3 \times 10^{17} \text{ cm}^{-3}$), to a shift

of $\Delta\nu_9^{el} \sim 3$ GHz. This is of the same order as the shifts observed experimentally, thus confirming the presence of plasma induced chirp during HHG with 300 ps pulses.

As an increase in the electron density can induce a blueshift in the generated harmonics, so a decrease on N_e will result in redshifted harmonics. It is conceivable that a harmonic redshift can be associated with plasma dynamics. If the laser pulses have sufficiently long duration so that electrons have time to escape the focal zone and/or to recombine with ions via three body collisions, in both cases causing n^{el} to grow again. In the present experiment the fundamental pulses are focused to a spot with radius of about 15 μm ; assuming 1 eV kinetic energy for the generated photo-electrons, they can fly out the interaction region in about 25 ps, much less than the pulse duration. However, a quantitative estimate of the plasma dynamical effect on the chirp of the generated harmonics is not straightforward for 300 ps fundamental pulses, when substantial ionization occurs already before the peak of the pulse. As a side-effect the lowering of the refractive index in the ionizing medium causes defocusing of the incident laser beam, thus complicating even more the analysis of the phenomenon.

A temporal variation of the index of refraction is induced also by the Kerr-effect ($n(t) = n_0 + n_2 I(t)$), which produced a frequency excursion in the fundamental beam given by

$$\Delta\nu^K(t) = -\frac{\nu_1 n_2}{c} \int^L \frac{\partial I(t)}{\partial t} dz, \quad (6.6)$$

where n_2 is the nonlinear refractive index. When the ionization rate during the pulse is small, SPM due to the Kerr-effect will induce an almost symmetric broadening in the frequency spectrum. However, if one assumes HHG to take place predominantly during the leading edge of the intense laser pulse, the Kerr-effect induces a redshift in the harmonic radiation which can be approximated by

$$\Delta\nu_q^K = -\frac{q\nu_1 n_2 I_0 L}{c\tau}. \quad (6.7)$$

An estimate of the expected frequency redshift due to the Kerr effect can be performed considering the value of the nonlinear refractive index of gases, $n_2(\text{Ar}, \text{N}_2) \sim 10^{-19}$ cm^2/W at 1 bar (gas density $\sim 3 \times 10^{19}$ cm^{-3}) [170, 171]. Using Eq.(6.7) with $\tau = 300$ ps, $I_0 = 5 \times 10^{13}$ W/cm^2 , $L = 1$ mm, and $\nu_1 = 4 \times 10^{14}$ Hz the shift for the 9th harmonic generated in a jet with gas pressure of about 10 mbar is $|\Delta\nu_9^K| \sim 2$ MHz. This is almost three orders of magnitude smaller than the experimental results, thus it is ruled out as a possible source of the observed redshift in HHG with 300 ps pulses.

Single-atom effect The single-atom chirp effect in HHG originates from the time dependent electric dipole phase induced by the nonadiabatic change of the fundamental electric field within one optical cycle. An analytical form for the nonadiabatic frequency shift of the harmonic radiation is derived in Ref. [168] based on the strong-field approximation model and assuming a fundamental pulse with a Gaussian intensity profile:

$$\Delta\nu_q^{na} = \frac{I_p}{\pi\tau} \sqrt{4 \ln 2 \ln \left(\frac{I_0}{I_p} \right)} \frac{d\theta_q}{dI} \Big|_{I_p}, \quad (6.8)$$

where I_0 is the laser peak intensity, τ is the pulse duration and I_p is the intensity at the maximum electric dipole acceleration, i.e., maximum harmonic emission, which is found to be almost constant for short pulses ($\tau < 100$ fs). From the SFA model the phase of the q^{th} harmonic is given by $\theta_q = S(t_q) - q\omega_1 t_q$, where t_q is the returning time of the electron and $S(t_q)$ is the classical action of the electron in the intense laser field. A main characteristic of the density-independent single-atom nonadiabatic chirp effect is evident from Eq.(6.8): the harmonic shift is inversely proportional to the pulse duration. As for the harmonic order dependence, calculations and experiments show [168] that the frequency shift is almost quadratic with q . The intensity dependence of the nonadiabatic phase θ_q is with good approximation linear [161, 168]. Calculated values of $d\theta_q/dI$ are around 10^{-13} cm²/W for plateau harmonics generated in Ne with peak intensities higher than 10^{14} W/cm² and pulse durations of hundreds of fs [161, 172, 173]. The only experimental determination of the intensity-dependent dipole phase in HHG is performed using the technique of frequency-resolved optical gating and the value $d\theta_q/dI = 5 \times 10^{-15}$ cm²/W is reported for the fifth harmonic generated in Xe with 40 fs pulses at 6×10^{13} W/cm² [174]. An estimate of the expected single-atom contribution to the presently observed harmonic shift can be done using Eq.(6.8), assuming $I_p \sim I_s$ and $d\theta_q/dI \sim 10^{-14}$ cm²/W. Considering a pulse duration of 300 ps, a saturation intensity of 3×10^{13} W/cm² (typical for Ar, N₂) and a peak intensity of 5×10^{13} W/cm², the nonadiabatic shift is $\Delta\nu_q^{na} = 0.4$ GHz, one order of magnitude smaller than the observed harmonic shift. This leads us to assume that the nonadiabatic chirp is negligible when HHG is performed with 300 ps pulses.

6.5 Conclusions and outlook

A systematic high-resolution study of chirp effects in HHG has been performed. This was possible thanks to the accurate metrology on the fundamental laser frequency and the high spectral purity of the harmonics. Frequency shifts on the 9th and 13th harmonic produced in various gases were measured with an accuracy of $10^{-6} - 10^{-7}$ level, thus enabling a careful investigation of the chirp phenomenon in HHG.

When the peak laser intensity is above the saturation intensity for the nonlinear gaseous medium, the distinct effect of plasma formation is demonstrated by a frequency blueshift proportional to the gas density. The blueshift is superimposed on an almost density-independent redshift offset. This redshift, never observed before in HHG, is found to slightly increase in magnitude with the laser intensity. Self-phase modulation due to the nonlinear refractive index of neutral atoms would be consistent with the observed behavior. However, an estimate of the expected effect gives a value that is two orders of magnitude smaller than the measured frequency shift.

The effect of plasma formation, already demonstrated by the observed blueshift, may lead to a redshift as soon as the electron density in the laser focus decreases. This could be due to electrons leaving the interaction region or recombining with ions during the 300 ps pulse duration. A possible way to experimentally investigate the influence of plasma dynamics in HHG is to perform frequency shift measurements in SF₆/Xe mixtures. SF₆ has a very large electron-capture rate to form (SF₆⁻)^{*} ions, $\beta = 2.5 \times 10^{-7}$ cm³/s [175]. At a gas pressure of 10 mbar, $\beta \sim 10^{11}$ Hz and free electrons

have a lifetime of about 10 ps. Since the ionization energy of SF₆ is 15.3 eV, and that of Xe is 12.1 eV, SF₆ molecules will still be present when xenon is completely ionized, thus influencing the plasma dynamics during the HHG process. The dynamics in a laser formed plasma is complicated by the large gradients present in the process, and the actual influence in chirp phenomena during HHG is difficult to assess.

The redshift in the central frequency of the harmonic pulses may also be ascribed to significant frequency excursion in the instantaneous frequency of the fundamental pulses. The assumption made of a linear propagation of the net frequency shift may underestimate the effect of the chirp in the fundamental pulses. This is especially true if the frequency excursion during the pulse is large and harmonic generation is confined in a limited time window. The frequency chirp of pulsed-dye-amplified nanosecond pulses has been measured to be as large as tens of MHz [34, 126, 127]. Since this chirp is related to the dynamic change of the gain in the dye, frequency excursions up to hundreds of MHz may be present using 300 ps pulses, giving rise to shifts on the order of several GHz in the generated harmonics. It has been found that the frequency chirp reverses its sign at a wavelength close to the maximum of the dye emission curve [126, 127], as well as does the net frequency shift as shown in Figure 6.2. This behavior suggests a way to experimentally study the effect of the frequency chirp in the fundamental pulses, that is to measure the frequency spectrum of the same harmonic at different fundamental wavelength on the opposite side of the dye gain curve. Using the ($3p^6\ ^1S_0 \rightarrow 3p^54d[3/2]_1$) transition in Ar at 83.4 nm [158] to measure the frequency shift of the 9th generated at $\lambda_{cw} = 751$ nm, it should be possible to test the effect of the frequency chirp in the fundamental 300 pulses on the observed shift in the harmonic frequency.

In conclusion, the experiments reported in the present Chapter show that high-resolution studies on the high-order harmonics frequency spectrum are possible thanks to the unique characteristics of continuous tunability and narrow bandwidth of the XUV laser source built in our laboratory. Particularly, it is demonstrated that shift-free high-order harmonics are generated at specific gas densities, when the plasma-induced blueshift and the offset redshift compensate.

6.6 Appendix: measurement of the frequency shift in the amplifier chain

6.6.1 Experimental setup and technique

It is known that frequency chirp in the pulsed-dye-amplification occurs, due to the time varying gain in the amplifying medium, which can result in spectral broadening and frequency shift. This effect is unavoidable, except for fortuitous combinations of light wavelength and dye [126, 127]. For the high-resolution measurements on the net frequency shift in HHG reported in this Chapter, it is important to know the frequency of the fundamental radiation at the time intervall, within the fundamental pulse, when harmonic generation takes place. A technique to measure the instantaneous frequency of ns pulses generated in seeded pulsed-dye-amplifiers has been demonstrated based on heterodyning the cw seed laser with the pulsed output of the PDA [34, 126, 127].

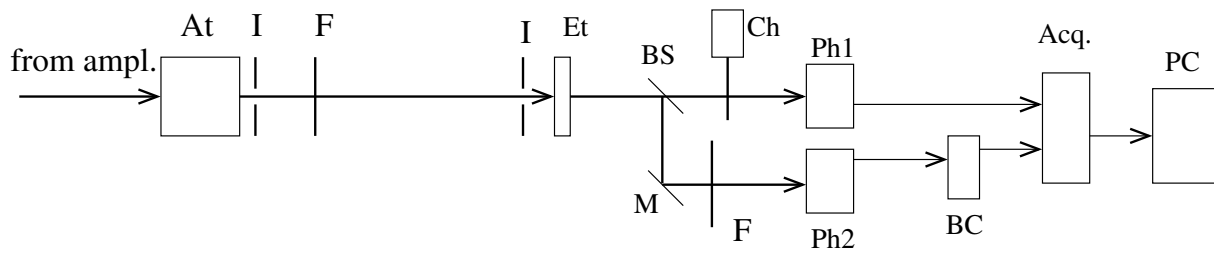


Figure 6.8. Schematic picture of the setup used for the measurement of the PDA output frequency shift: At, attenuator; I, 1mm iris diaphragm; F, neutral density filter; Et, etalon; BS, beam-splitter; M, mirror; Ch, optical chopper; Ph, photodiode; BC, integrator boxcar; Acq., acquisition system; PC, personal computer.

However, the use of such a technique is not straightforward in the present case due to the short duration (~ 300 ps) of the output laser pulses. Alternatively, we study the frequency spectrum of the output pulses by measuring the transmitted light through an etalon. A direct comparison with the transmission peak of the seeding cw light beam enables the determination of the shift of the central frequency of the laser pulses with respect to the seeding light frequency. Using such a technique only the average chirp, i.e., the net frequency shift, can be measured.

A schematic picture of the setup used for the measurement of the PDA output frequency shift is shown in Figure 6.8. The output beam from the amplifier chain (PDA and Ti:Sa amplifiers), which consists of the pulsed beam superimposed to the cw beam, is sent to an etalon (FSR ~ 21 GHz). In order to avoid optical damage on the etalon the beam is attenuated by means of a variable attenuator and neutral density filters. The central part of the beam is selected and collimated by means of two iris diaphragms of 1 mm in diameter and placed 50 cm apart. The etalon is carefully set to be orthogonal the cw beam by aligning the reflected beam on a 1 mm iris diaphragm placed in the incident beam path two meters before the etalon.

The light transmitted by the etalon is split into two paths, which will be called the *cw* and *pulsed-path*. In the *cw-path* the transmitted cw seeding beam is detected using a gated photodiode (Ph1, gate duration ~ 100 μ s). In this path the transmitted pulses are blocked by means of an optical chopper which is synchronised with respect to the pump lasers of the amplifier chain. A beam splitter is used to send few % of the transmitted light through the *pulsed-path*, in which the pulses are detected with a fast photodiode Ph2 and the signal recorded using a boxcar integrator. The signals from Ph1 and Ph2 are synchronously acquired and stored in a personal computer while scanning the cw seeding light frequency through a transmission peak of the etalon. As an example, Figure 6.9 shows the recorded *cw-path* (filled circles) and *pulsed-path* (open squares) data points obtained scanning the cw light frequency around 751 nm. A least-square fit with the Airy function on the *cw-path* data points (solid line) results in a full-width-half-maximum of about 1 GHz, yielding an etalon finesse of about 21. The zero frequency is chosen as the maximum transmission frequency of the cw light. A running average on the *pulsed-path* data points (dashed line) shows a spectral broadening (FWHM ~ 1.7 GHz) and a central frequency shift of about 100 MHz to the red. Note that a redshift in the recorded transmission peak implies an equivalent blueshift of the central frequency of the pulses.

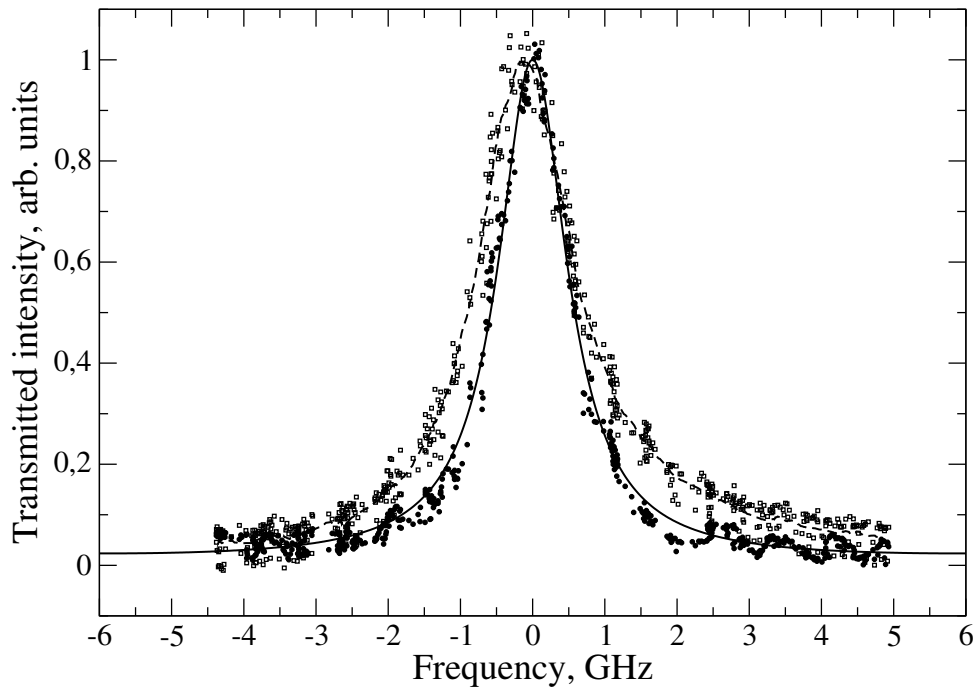


Figure 6.9. Transmission peaks of the etalon synchronously recorded for the *cw*-path (filled circles) and *pulsed*-path (open squares) while scanning the *cw* frequency at 751 nm. Zero-frequency corresponds to the maximum transmission frequency of the *cw*-path data points as obtained by a least-square fit using the Airy function (solid line). A running average is performed on the *pulsed*-path data points (dashed line).

Results of such a measurement for various *cw* wavelengths are reported in Figure 6.2. Two set of measurements performed selecting different parts of the laser beam profile around its center (by means of the iris diaphragms shown in Figure 6.8), give frequency shifts consistent within the error margin (~ 20 MHz).

6.6.2 Misalignment effect

The experimental technique discussed above may suffer from a systematic effect which can result in an *apparent* blueshift of the pulsed light central frequency. This systematic effect is related to the dependence of the etalon transmission curve on the input beam alignment. Assuming that the etalon is placed orthogonally with respect to the *cw* beam propagation direction the transmission curve of the etalon is

$$T_{cw}(\lambda) \equiv \frac{I_{in}}{I_{out}} = \frac{1}{1 + \frac{4R}{1-R^2} \sin^2\left(\frac{2\pi dn}{\lambda}\right)}, \quad (6.9)$$

where R , d and n are the reflectivity, the thickness and refractive index of the etalon respectively, while I_{in} and I_{out} are the input and output laser intensities respectively. The wavelength of maximum transmission is given by $\lambda_{cw}^{max} = \frac{2dn}{m}$, where m is the order of interference. If the pulsed beam is misaligned by an angle θ_p with respect to

the cw beam, then the transmission curve for the pulsed beam is given by

$$T_p(\lambda) = \frac{1}{1 + \frac{4R}{1-R^2} \sin^2\left(\frac{2\pi dn}{\lambda} \cos \theta_p\right)}, \quad (6.10)$$

and the wavelength of maximum transmission for the pulsed is given by $\lambda_p^{max} = \frac{2dn}{m} \cos \theta_p$. The measured wavelength shift between the pulsed and cw light is $\Delta\lambda_p \equiv \lambda_p^{max} - \lambda_{cw}^{max}$, corresponding to a frequency shift $\Delta\nu_p = -\Delta\lambda_p\lambda/\nu$. Thus the misalignment results in an *apparent* frequency blueshift given by

$$\Delta\nu_p^{mis} = \nu_{cw} \frac{\theta_p^2}{2} \geq 0, \quad (6.11)$$

where the assumption $\theta_p \ll 1$ had been made. As example, a misalignment of $\theta_p \sim 1$ mrad results in an *apparent* blueshift offset of about 200 MHz at a wavelength of 780 nm.

Samenvatting

Dit proefschrift (*Kleinschalige afstembare smalbandige extreem ultraviolette bronnen: van lage naar hoge orde optische harmonische generatie*) beschrijft de ontwikkeling en toepassing van kleinschalige (d.w.z. passend op een enkele optische tafel) stralingsbronnen in het vacuüm ultraviolette (VUV, 200-100 nm) en extreem ultraviolette (XUV, 100-10 nm) deel van het elektromagnetische spectrum. Meer specifiek, niet-lineaire conversie van laserstraling in een gasvormig medium wordt benut om smalbandige en continue afstembare straling te genereren. Met een dergelijke lichtbron kan nauwkeurige hoge-resolutie spectroscopie verricht worden in het frequentiedomein, om zodoende de energieniveauctuur van atomen en moleculen te ontrafelen.

Hoofdstuk 1 bevat een inleiding in de niet-lineaire optische processen van harmonische generatie met behulp van intense laserpulsen. Twee verschillende gebieden van lage en van hoge orde harmonische productie worden onderscheiden: lage orde harmonische generatie (LHG) met pulsen van relatief gematigde intensiteit ($I < 10^{13}$ W/cm²) wordt beschreven met storingstheorie; het proces van hoge orde harmonische generatie (HHG) wordt beschreven in termen van een semi-klassiek driestaps botsingsmodel. Als sterke ionisatie optreedt, door multi-foton absorptie en door "tunneling", is storingstheorie niet langer toepasbaar. Specifieke kleinschalige bronnen in het VUV/XUV domein, die gebaseerd zijn op LHG en HHG, en voorbeelden van toepassingen ervan worden besproken.

Deel I (Hoofdstukken 2 en 3) beschrijft spectroscopische metingen aan xenon en krypton, verricht met een VUV stralingsbron gebaseerd op LHG. Metrologische studies met hoge precisie maken het mogelijk de energie van aangeslagen toestanden nauwkeurig te bepalen. De energieniveauctuur van krypton is bepaald met een ongekende absolute nauwkeurigheid van 40 MHz. Een nieuwe nauwkeurige bepaling van de ionisatie-energieën van zowel xenon en krypton wordt beschreven. Met behulp van massa-opgeloste spectroscopie maakt het mogelijk om isotoopverschuivingen en de hyperfijnstructuur van aangeslagen toestanden te bepalen. In zowel xenon als ook in krypton leert een grafische analyse volgens King, dat sterke ladingsafscherming optreedt door het buitenste *p*-electron op het *s*-electron in de voor edelgasen karakteristieke gesloten schil configuratie. Hyperfijnconstanten zijn bepaald voor enkele aangeslagen toestanden in xenon. Onderzoek aan de verschuiving van een twee-foton aangeslagen toestand in krypton door het dynamisch Stark effect geeft belangrijke inzichten voor absolute ijking van XUV-frequenties, als die geproduceerd worden door resonantie versterkte processen.

Deel II behandelt de ontwikkeling en de toepassing van een nieuw type XUV stralingsbron gebaseerd op HHG.

In Hoofdstuk 4 wordt een lasersysteem beschreven, dat nabij-infrarode laserpulsen levert van 300 ps tijdsduur, 225 mJ aan energie en bij 10 Hz herhalingsfrequentie. De in golflengte verstembare pulsen worden geproduceerd in een gepulste kleurstofversterker die gepompt wordt door gepulste Nd:YAG laser en de frequentie wordt bepaald door injectering van licht uit een continue Titaansaffier laser. De pulsen van 300 ps

duur worden op hun beurt geproduceerd door toepassing van de techniek van pulscompressie door gestimuleerde Brillouinverstrooiing. De zo geproduceerde pulsen in het nabije infrarood worden versterkt in een Titaansaffier versterkerketen. De resulterende hoog-energetische pulsen in het nabije infrarood hebben een fraai bundel profiel ($M^2 = 1.2$) en zijn in bandbreedte bijna Fourier begrensd (tijd-frequentie bandbreedte product = 0.48).

In Hoofdstuk 5 wordt de productie en karakterisatie van smalbandige en verstembare hoge orde harmonischen gerapporteerd. Als de hoogvermogen nabij-infrarode pulsen met een 20 cm lens worden gefocusseerd, wordt een lichtintensiteit bereikt van 5×10^{13} W/cm² en daarmee wordt coherente straling geproduceerd in edelgasen met golflengtes zo laag als 40 nm (bij de 21^{ste} harmonische). Het frequentiespectrum van de harmonischen wordt bepaald via lineaire absorptiespectroscopie aan welbekende atomaire spectraallijnen. De bandbreedte van de 9^e en 15^e harmonischen, bij 86 nm en 52 nm geeft een oplossend vermogen ($\lambda/\Delta\lambda$) van 2.8×10^5 . Vanuit het perspectief van bandbreedte en resolutie zijn deze resultaten beter dan wat wordt bereikt bij speciale stations bij synchrotron bronnen, en ze brengen hoge orde harmonische generatie in het domein van hoge resolutie VUV/XUV spectroscopie.

In Hoofdstuk 6 wordt een precisie-studie aan zg. "chirp"-effecten in HHG beschreven. Vooral de frequentieverschuiving in de harmonischen in relatie tot de verwachte waarden (gehele veelvoud van de fundamentele frequentie) is gemeten in hoge resolutie en als functie van de gasdichtheid. We vinden dat de belangrijkste bijdrage aan deze "chirp" in HHG komt van zelf-fasemodulatie in de fundamentele, die geïnduceerd wordt door temporele veranderingen in de brekingsindex van het plasma, dat geproduceerd wordt door de laser. Dit resulteert in een blauw-verschuiving van de harmonische frequenties evenredig met de gasdichtheid. Andere effecten, zoals zelf-fasemodulatie a.g.v. het Kerr-effect van neutrale atomen, of het niet-adiabatische effect gerelateerd aan botsingsprocessen in HHG, geven een verwaarloosbare bijdrage als pulsen van 300 ps worden gebruikt. Van speciaal belang is de waarneming van een dichtheidsafhankelijke roodverschuiving in de harmonische frequentie. Dit fenomeen, tot dusverre nog niet waargenomen in HHG, kan wellicht worden gerelateerd aan plasma-dynamische effecten, of aan een sterke frequentie-"chirp" in de fundamentele. Mogelijk experimenten om de aard van deze roodverschuiving te onderzoeken worden gesuggereerd.

Summary

This thesis (entitled, *Table-top tunable narrow-band extreme-ultraviolet sources: from low to high-order optical harmonic generation*) is devoted to the development and application of table top sources in the vacuum-ultraviolet (VUV, 200-100 nm) and extreme-ultraviolet (XUV, 100-10 nm) regions of the electromagnetic spectrum. Specifically, nonlinear up-conversion of laser radiation in a gaseous medium is used to generate narrow-band continuously tunable radiation. With such a source, on-line accurate frequency domain spectroscopy can be performed at high-resolution, revealing features in the level structures of atoms and molecules.

In Chapter 1 an introduction on the nonlinear physical process of optical harmonic generation in gases with intense laser pulses is given. The two different regimes of low and high-order harmonic generation are presented: low-order harmonic generation (LHG) with pulses of relatively moderate intensity ($I < 10^{13}$ W/cm²) is described in term of perturbation theory; the process of high-order harmonic generation (HHG), occurring at higher intensity ($I > 10^{13}$ W/cm²), is described in terms a of the three-step semiclassical re-collision model. The break-down of the perturbative approach and the on-set of substantial photoionization, due to both multiphoton absorption or tunneling, is also discussed. Specific table-top VUV/XUV sources based on of both low and high-order harmonic generation and examples of their applications are presented.

In Part I (Chapter 2 and 3) VUV spectroscopic measurements of xenon and krypton performed with a table top source based on LHG are presented. Precision metrology studies enable accurate determination of the excited state level energies. Specifically, the energy level structure of krypton is determined with an unprecedented absolute accuracy of about 40 MHz. New accurate determination of the ionization energies of both xenon and krypton is also reported. Mass resolved spectroscopy enables the measurement of the isotope shift and hyperfine structure of the excited states. For both xenon and krypton the well known King plot analysis reveal a strong screening effect of the outer p -electron on the s -electron in the closed shell configuration typical of noble gases. For xenon, hyperfine constants are determined for some excited states. For krypton, investigation on the ac-Stark shift on a specific two-photon transition gives useful insight for the absolute frequency calibration of XUV radiation produced by two-photon resonant-enhanced four-wave-mixing.

Part II concerned with the development and characterization of a novel XUV source based on HHG.

In Chapter 4 an original laser system delivering continuously tunable near-infrared pulses with 300 ps time duration, 225 mJ of energy and 10 Hz repetition rate is presented. The tunable pulses are generated in a pulsed-dye-amplifier pumped by the second harmonic of a Q-switched Nd:YAG laser and seeded by a continuous Ti:Sapphire laser. The 300 ps pump pulses are obtained via a compression technique based on the stimulated-Brillouin-scattering process. The near-infrared pulses are then amplified in a Ti:Sapphire amplifier chain. The energetic near infrared pulses have a good

beam quality ($M^2 = 1.2$) and are close to the Fourier transform limit (time-frequency band-width product = 0.48).

In Chapter 5 the production and characterization of tunable narrow-band high-order harmonics is reported. Focusing the energetic near infrared pulses with a 20 cm focal length lens an intensity of 5×10^{13} W/cm² is achieved and coherent radiation down to 40 nm (21st harmonic order) is generated in noble gases. The frequency spectrum of the harmonics is determined by performing linear absorption on well calibrated narrow atomic lines. Specifically, the band-width of the 9th and 15th harmonic, at 86 nm and 52 nm respectively, is measured demonstrating a resolving power ($\lambda/\Delta\lambda$) of 2.8×10^5 . From the perspectives of band-width and resolution these results are superior to what is achieved at the dedicated high-resolution VUV/XUV beamlines at synchrotrons worldwide, and bring HHG in the realm of high-resolution VUV/XUV spectroscopy.

In Chapter 6 an accurate investigation on frequency chirp in HHG is reported. In particular the frequency shift of the harmonics with respect to the expected value (integer multiple of the fundamental frequency) is measured at high-resolution as function of the gas density. It is found that the major contribution to frequency chirp in HHG is due to self-phase modulation (SPM) of the fundamental beam induced by temporal changes of the refractive index in the laser-produced plasma. This results in a blueshift of the harmonic frequency proportional to the gas density. Other effects, like SPM due to the Kerr-effect of neutral atoms, or the nonadiabatic effect related to the re-collision nature of HHG, give a negligible contribution when 300 ps pulses are used. Of particular interest is the observation of a density-independent redshift in the harmonic frequency. This phenomenon, never observed before in HHG, may be related to plasma dynamic effects or to a strong frequency chirp present in the fundamental pulses. Possible experiments to investigate the origin of this redshift are suggested.

Riassunto

La presente tesi, dal titolo *Sorgeneti nell'estremo ultravioletto, table-top, accordabili in frequenza ed a banda stretta: generazione di armoniche dal basso all'alto ordine*, è dedicata allo sviluppo e all'utilizzo di sorgenti *table-top* nelle regioni dell'ultravioletto del vuoto (VUV, 200-100 nm) e dell'estremo ultravioletto (XUV, 100-10 nm) dello spettro elettromagnetico. In particolare, la conversione di luce laser tramite processi nonlineari in gas è usata per generare radiazione a banda stretta e accordabile in frequenza. Questo tipo di sorgenti aprono nuove prospettive nel campo della spettroscopia in frequenza ad alta risoluzione, permettendo uno studio accurato della struttura dei livelli energetici in atomi e molecole.

Nel Capitolo 1 vengono discussi i processi nonlineari di generazione di armoniche in gas con impulsi laser intensi. In particolare viene affrontato il problema considerando due regimi distinti dipendenti dall'intensità di pompa, ovvero: la generazione di armoniche di basso ordine (LHG) con impulsi di intensità $< 10^{13}$ W/cm², che è consistente con la teoria perturbativa della polarizzazione del mezzo, e il processo di generazione di armoniche di alto ordine (HHG) per intensità $> 10^{13}$ W/cm² che richiede lo sviluppo di modelli non perturbativi. In particolare, desciveremo il modello semiclassico di ricombinazione, noto come *Three-step model*. Sono anche discussi inoltre, sia il limite dell'approccio perturbativo sia l'insorgere del processo di fotoionizzazione, multifotonica e tunnel, all'aumentare dell'intensità dell'impulso. Presenteremo anche specifiche sorgenti *table-top* di radiazione VUV/XUV basate sulla generazione di armoniche di basso ed alto ordine ed esempi di applicazioni.

Nella Parte I della tesi (Capitoli 2 e 3) vengono presentate misure di spettroscopia nel VUV sul krypton e sullo xenon effettuate con una sorgente *table-top* basata sulla LHG. Un'accurata metrologia sulla radiazione eccitante permette una precisa misura dall'energia dei livelli eccitati. In particolare, la struttura energetica del krypton è stata determinata con una precisione di 40 MHz, mai ottenuta in precedenza. Sono stati anche ottenuti nuovi valori per il potenziale di ionizzazione del krypton e dello xenon. L'utilizzo di tecniche per la spettroscopia risolta in massa hanno permesso lo studio degli shift isotopici e della struttura iperfine dei livelli eccitati. Tramite un'analisi basata sul metodo dei King plot è stato osservato un importante effetto di screening da parte degli elettroni negli orbitali p esterni sugli elettroni negli orbitali s nella configurazione a guscio chiuso tipica dei gas nobili. Per lo xenon sono state determinate le costanti di struttura fine di alcuni livelli eccitati. Per il krypton, lo studio dello Stark shift dimanico ha fornito utili informazioni per la calibrazioni della frequenza di radiazione XUV generata mediante il processo nonlineare di four-wave-mixing risonante a due fotoni.

La Parte II della tesi è dedicata allo sviluppo e caratterizzazione di una nuova sorgente di radiazione XUV basata sul processo di HHG.

Nel Capitolo 4 è presentato un originale sistema laser che genera impulsi di 300 ps accordabili in frequenza nell'infrarosso con un'energia di 225 mJ ed una frequenza di ripetizione di 10 Hz. Gli impulsi accordabili in frequenza sono generati in un pulsed-dye-amplifier pompato dalla seconda armonica di un Q-switched Nd:YAG laser ed

iniettato con un cw Ti:Sapphire laser. Gli impulsi di pompa da 300 ps sono ottenuti mediante una tecnica di compressione basata sul processo di stimulated-Brillouin-scattering. Gli impulsi infrarossi sono amplificati in una catena di amplificatori al Ti:Sapphire. Il fascio finale ha un'ottima qualità spaziale ($M^2 = 1.2$) e gli impulsi energetici sono quasi al limite della trasformata di Fourier (prodotto banda-durata = 0.48).

Nel Capitolo 5 è presentata la generazione e caratterizzazione di armoniche di alto ordine accordabili in frequenza. Focalizzando gli intensi impulsi laser mediante una lente di focale 20 cm si ottiene un'intensità di 5×10^{13} W/cm² che permette di generare radiazione fino a 40 nm (21esima armonica) usando gas nobili. Lo spettro in frequenza delle singole armoniche è stato determinato mediante spettroscopia in assorbimento su transizioni atomiche note. In particolare, la larghezza di banda è stata misurata per le armoniche di ordine 9 e 15 (rispettivamente a 86 nm e 52 nm), dimostrando un potere risolutivo, $\lambda/\Delta\lambda$, di 2.8×10^5 . Per quanto riguarda la larghezza di banda e la risoluzione, questi risultati sono migliori di ciò che è attualmente ottenuto con specifiche VUV/XUV beamline ad alta risoluzione nei sincrotroni e dimostrano l'efficacia della tecnica di HHG nel campo della spettroscopia ad alta risoluzione.

Nel Capitolo 6 è presentato uno studio accurato degli effetti di chirp in frequenza nel processo di HHG, realizzato grazie alle specifiche caratteristiche di accordabilità ed alta risoluzione della sorgente XUV. In particolare abbiamo studiato lo spostamento in frequenza delle armoniche rispetto al valore ideale, cioè multiplo intero della frequenza del fascio fondamentale. L'effetto maggiore è dovuto alla variazione dell'indice di rifrazione degli elettroni nel plasma generato durante l'interazione gas-laser. Tale effetto risulta in uno spostamento in frequenza verso il blu proporzionale alla densità del gas. Altri fenomeni, tipo modulazione di fase dovuta all'effetto Kerr degli atomi neutri o fenomeni nonadiabatici in HHG, producono effetti trascurabili usando impulsi di 300 ps. Particolarmente interessante è la presenza di uno spostamento in frequenza verso il rosso che risulta indipendente dalla densità del gas. Tale effetto, mai osservato in HHG, potrebbe essere dovuto a fenomeni legati alla dinamica del plasma o a rilevanti chirp in frequenza presenti nell'impulso fondamentale. Infine, discutiamo possibili esperimenti per indagare la natura dello shift in frequenza verso il rosso.

Acknowledgments

I am deeply grateful to Wim Ubachs for his valuable scientific advises and ideas that made this thesis possible, and also for his understanding and support in difficult personal situation.

Many thanks to all the members of the Atomic Physics group, with whom I had great time during the past four years, and the visitors of our laboratory with whom I had the opportunity to work with.

Special thanks to Jacques Bouma, for his technical help in the laboratory (and for the wonderful dinners on the floating house), and Petra de Gijzel for her help in solving practical living problems as a foreigner in Amsterdam.

In fine, il mio pensiero va a Roberta per la pazienza avuta ed il supporto datomi durante gli ultimi tre anni, come pure per la gioia di condividere nostro figlio Tommaso.

Publications

Journal papers

-) *High-Order Harmonic Generation Yielding Tunable Extreme-Ultraviolet Radiation of High Spectral Purity*; **F. Brandi**, D. Neshev and W. Ubachs; Phys. Rev. Lett. **91** (2003) 163901; **selected for the November 2003 issue of the Virtual Journal of Ultrafast Science at <http://www.vjultrafast.org>**;
awarded as the best article of the LCVU in 2003.

-) *A novel narrow-band wavelength-tunable laser system delivering high-energy 300 ps pulses in the near-infrared*; **F. Brandi**, I. Velchev, D. Neshev, W. Hogervorst and W. Ubachs; Rev. Sci. Instr. **74** (2003) 32; **selected for the February 2003 issue of the Virtual Journal of Ultrafast Science at <http://www.vjultrafast.org>**..

-) *Bound energy levels at the $n=2$ dissociation threshold in HD*; T. Pielage, A. de Lange, **F. Brandi** and W. Ubachs; Chem. Phys. Lett. **366** (2002) 583.

-) *Predissociation of the $4p\pi L^1\Pi$ Rydberg state of carbon monoxide*; P. Cacciani, **F. Brandi**, J.P. Sprengers, A. Johansson, A. L'Huillier, C.-G. Wahlström and W. Ubachs; Chem. Phys. **282** (2002) 63.

-) *High-resolution vacuum-ultraviolet and ultraviolet photoionization spectroscopy of krypton*; **F. Brandi**, W. Hogervorst and W. Ubachs. J. of Phys. **B 35** (2002) 1071, **Iop select**.

-) *Vacuum-ultraviolet spectroscopy of Xe: hyperfine splittings, isotope shifts and isotope-dependent ionization energies*; **F. Brandi**, I. Velchev, W. Hogervorst and W. Ubachs; Phys. Rev. **A 64** (2001) 032505.

-) *Isotope dependent predissociation in the $C^1\Sigma^+, v=0$ and $v=1$ states of CO*; P. Cacciani, **F. Brandi**, I. Velchev, A. L'Huillier, C.-G. Wahlström and W. Ubachs; Eur. Phys. J. **D 15** (2001) 47.

-) *Stress-optic modulator: a novel device for high sensitivity linear birefringence measurements*; **F. Brandi**, E. Polacco and G. Ruoso; Meas. Sci. Technol. **12** (2001) 1503.

-) *Cotton-Mouton effect of molecular oxygen: a novel measurement*; **F. Brandi**, F. Della Valle, A. M. De Riva, P. Micossi, F. Perrone, C. Rizzo, G. Ruoso and G. Zavattini; J. Opt. Soc. Am. **B 15** (1998) 1278.

-) *Measurement of the phase anisotropy of very high reflectivity interferential mirrors*; **F. Brandi**, F. Della Valle, A. M. De Riva, P. Micossi, F. Perrone, C. Rizzo, G. Ruoso and G.

Zavattini; Appl. Phys. **B 65** (1997) 351.

Conference papers

-) *Precision laser spectroscopy on Ar, Kr and Xe*; I. Velchev, **F. Brandi**, W. Hogervorst and W. Ubachs; Conference Digest of the International Quantum Electronics Conference (2000); IEEE, Piscataway, NJ (USA).

-) *First run of the PVLAS experiment: dark matter candidates production and detection*; G. Cantatore, F. Della Valle, E. Zavattini, F. Brandi, S. Carusotto, E. Polacco, M. Bregant, G. Ruoso, U. Gastaldi, R. Pengo, G. Di Domenico, G. Zavattini, E. Milotti; Proceedings of IDM2000- N.J.C. Spooner, V. Kudryavtsev Eds.- World Scientific (2001).

-) *Optical production and detection of dark matter candidates*; **F. Brandi**, Bregant M, Cantatore G, Della Valle F, Carusotto S, Di Domenico G, Gastaldi U, Milotti E, Pengo R, Polacco E, Rizzo C, Ruoso G, Zavattini E, Zavattini G; Nucl. Instrum. Meth. **A 461** (2001) 329.

-) *The PVLAS collaboration: experimental search for anisotropy of the phase velocity of light in vacuum due to a static magnetic field*; E. Zavattini, F. Brandi, M. Bregant, G. Cantatore, S. Carusotto, F. Della Valle, G. Di Domenico, U. Gastaldi, E. Milotti, R. Pengo, G. Petrucci, E. Polacco, G. Ruoso, and G. Zavattini; AIP Conference Proceedings **564** (2001) 77.

-) *Magnetic birefringence of vacuum: the PVLAS experiment*; R. Pengo, Bakalov, U. Gastaldi, G. Petrucci, G. Bialolenker, F. Brandi, E. Polacco, G. Cantatore, F. Della Valle, P. Micossi, E. Milotti, C. Rizzo, E. Zavattini, E. Iacopini, M. Bregant, G. Ruoso, G. Zavattini; Proceedings of the Workshop on Frontier test of QED and Physics of the Vacuum (1998) 59; Heron Press, Sofia (Bulgaria).

-) *Experimental method to detect the magnetic birefringence of vacuum*; D. Bakalov, F. Brandi, G. Cantatore, G. Carugno, S. Carusotto, F. Della Valle, A.M. De Riva, U. Gastaldi, E. Iacopini, P. Micossi, E. Milotti, R. Onofrio, R. Pengo, F. Perrone, G. Petrucci, E. Polacco, C. Rizzo, G. Ruoso, E. Zavattini, G. Zavattini; Quantum and Semiclass. Opt. **10** (1998) 239.

-) *The measurement of vacuum polarization: The PVLAS experiment*; D. Bakalov, F. Brandi, G. Cantatore, G. Carugno, S. Carusotto, F. Della Valle, A. De Riva, U. Gastaldi, E., Iacopini, P. Micossi, E. Milotti, R. Onofrio, R. Pengo, F. Perrone, G. Petrucci, E. Polacco, C. Rizzo, G. Ruoso, E. Zavattini, G. Zavattini; Hyperfine Interactions **114** (1998) 103.

Bibliography

- [1] T. H. Maiman. *Nature* **187**, 493 (1960).
- [2] P. A. Franken, A. E. Hill, C. W. Peters and G. Weinreich. *Phys. Rev. Lett.* **7**, 118 (1961).
- [3] T. Ditmire, J. K. Crane, H. Nguyen, L. B. DaSilva and M. D. Perry. *Phys. Rev. A* **51**, R902 (1995).
- [4] A. Rundquist, C. G. Dufree, Z. Chang, C. Herne, S. Backus, M. M. Murnane and H. C. Kapteyn. *Science* **280**, 1412 (1998).
- [5] J.-F. Hergott, M. Kovacev, H. Merdij, C. Hubert, Y. Mairesse, E. Jean, P. Breger, P. Agostini, B. Carré and P. Salières. *Phys. Rev. A* **66**, 021801(R) (2002).
- [6] Z. Chang, A. Rundquist, H. Wang, M. M. Murnane and H. C. Kapteyn. *Phys. Rev. Lett.* **79**, 2967 (1997).
- [7] M. Hentschel, R. Keinberg, C. Spielmann, G. A. Reider, N. Milosevic, T. Brabec, P. Corkum, U. Heinzmann, M. Drescher and F. Krausz. *Nature* **414**, 509 (2001).
- [8] F. Reintjes. *Nonlinear Optical Parametric Processes in Liquids and Gases* (Academic Press, New York, 1984).
- [9] R. W. Boyd. *Nonlinear Optics* (Academic Press, Boston, 1994).
- [10] G. C. Bjorklund. *IEEE J. Quantum Electron.* **11**, 287 (1975).
- [11] M. Nurhuda, A. Suda and K. Midorikawa. *RIKEN Review* **48**, 40 (2002).
- [12] M. Nurhuda, A. Suda and K. Midorikawa. *Phys. Rev. A* **66**, 041802(R) (2002).
- [13] J. A. Armstrong, N. Bloembergen, J. Ducuing and P. S. Pershan. *Phys. Rev.* **127**, 1018 (1962).
- [14] J. F. Ward and G. H. C. New. *Phys. Rev.* **185**, 185 (1969).
- [15] S. E. Harris and R. B. Miles. *Appl. Phys. Lett.* **19**, 385 (1971).
- [16] J. F. Young, G. C. Bjorklund, A. H. Kung, R. B. Miles and S. E. Harris. *Phys. Rev. Lett.* **27**, 1551 (1971).
- [17] R. T. Hodgson, P. P. Sorokin and J. J. Wynne. *Phys. Rev. Lett.* **32**, 343 (1974).
- [18] J. Reintjes, C.-Y. She and R. C. Eckardt. *IEEE J. Quantum Electron.* **14**, 581 (1978).
- [19] A. H. Kung. *Opt. Lett.* **8**, 24 (1983).
- [20] R. Hilbig and R. Wallenstein. *IEEE J. Quantum Electron.* **19**, 194 (1983).
- [21] G. Hilber, A. Lago and R. Wallenstein. *J. Opt. Soc. Am B* **4**, 1753 (1987).
- [22] H. Pummer, T. Srinivasan, H. Egger, K. Boyer, T. S. Luk and C. H. Rhodes. *Opt. Lett.* **7**, 93 (1982).
- [23] T. Srinivasan, H. Egger, H. Pummer and C. H. Rhodes. *IEEE J. Quantum Electron.* **19** (1983).
- [24] W. Jamroz and P. B. Stoicheff. In *Progress in Optics*, edited by E. Wolf, vol. 20, 324 (North Holland, Amsterdam, 1983).
- [25] C. R. Vidal. In *Tunable Lasers*, vol. 59, chap. 3 (Springer, Heidelberg, 1987).
- [26] A. H. Kung, J. F. Young, G. C. Bjorklund and S. E. Harris. *Phys. Rev. Lett.* **29**, 985 (1972).
- [27] E. Cromwell, T. Trickl, Y. T. Lee and A. H. Kung. *Rev. Sci. Instrum.* **60**, 2888 (1989).

- [28] T. Trickl, M. J. J. Vrakking, E. Cromwell, Y. T. Lee and A. H. Kung. *Phys. Rev. A* **39**, 2948 (1989).
- [29] K. S. E. Eikema, W. Ubachs, W. Vassen and W. Hogervorst. *Phys. Rev. Lett.* **76**, 1216 (1996).
- [30] P. Cacciani, F. Brandi, J. P. Sprengers, A. Johansson, A. L'Huillier, C.-G. Wahlström and W. Ubachs. *Chem. Phys.* **282**, 63 (2002).
- [31] J. Sprengers, W. Ubachs, K. Baldwin, B. Lewis and W.-U. Tchang-Brillet. *J. Chem. Phys.* **119**, 3160 (2003).
- [32] T. Pielage, A. de Lange, F. Brandi and W. Ubachs. *Chem. Phys. Lett.* **366**, 583 (2002).
- [33] E. Eyler, A. Yiannopoulou, S. Gangopadhyay and N. Melikechi. *Opt. Lett.* **22**, 49 (1997).
- [34] K. S. E. Eikema, W. Ubachs, W. Vassen and W. Hogervorst. *Phys. Rev. A* **55**, 1866 (1997).
- [35] P. R. Herman, P. E. LaRocque, R. H. Lipson, W. Jamroz and B. P. Stoicheff. *Can. J. Phys.* **63**, 1581 (1985).
- [36] C. H. Muller, D. D. Lowenthal, M. A. DeFaccio and A. V. Smith. *Opt. Lett.* **13**, 651 (1988).
- [37] R. Hilbig and R. Wallenstein. *IEEE J. Quantum Electron.* **19**, 1759 (1983).
- [38] Y. Hirakawa, A. Nagai, K. Muraoka, T. Okada and M. Maeda. *Opt. Lett.* **9**, 735 (1993).
- [39] K. K. Innes, B. P. Stoicheff and S. C. Wallace. *Appl. Phys. Lett.* **29**, 715 (1976).
- [40] K. Tsukiyama, M. Momose, M. Tsukakoshi and T. Kasuya. *Opt. Comm.* **79**, 88 (1990).
- [41] G. W. Faris, S. A. Meyer, M. J. Dyer and M. J. Banks. *J. Opt. Soc. Am. B* **17**, 1856 (2000).
- [42] K. Miyazaki, H. Sakai and T. Sato. *Appl. Opt.* **28**, 699 (1989).
- [43] J. P. Marangos, N. Shen, H. Ma, M. H. R. Hutchinson and J. P. Connerade. *J. Opt. Soc. Am. B* **7**, 1254 (1990).
- [44] A. Balakrishnan, V. Smith and P. B. Stoicheff. *Phys. Rev. Lett.* **68**, 2149 (1992).
- [45] A. Balakrishnan, V. Smith and P. B. Stoicheff. *Phys. Rev. A* **49**, 2460 (1994).
- [46] U. Hollenstein, H. Palm and F. Merkt. *Rev. Sci. Instrum.* **71**, 4023 (2000).
- [47] U. Hollenstein, R. Seiler and F. Merkt. *J. Phys. B* **36**, 893 (2003).
- [48] H. J. Wörner, U. Hollenstein and F. Merkt. *Phys. Rev. A* **68**, 032510 (2003).
- [49] P. Rupper and F. Merkt. *Rev. Sci. Instrum.* **75**, 613 (2004).
- [50] A. L'Huillier, L. A. Lompré, G. Mainfray and C. Manus. *J. Phys. B* **16**, 1363 (1983).
- [51] X. F. Li, A. L'Huillier, M. Ferray, L. A. Lompré and G. Mainfray. *Phys. Rev. A* **39**, 5751 (1989).
- [52] M. D. Perry, O. L. Landen, A. Szöke and E. M. Campbell. *Phys. Rev. A* **37**, 747 (1988).
- [53] C. Cornaggia, J. Lavancier, D. Normand, J. Morellec and H. X. Liu. *Phys. Rev. A* **42**, 5464 (1990).
- [54] B. Chang, P. R. Bolton and D. N. Fittinghoff. *Phys. Rev. A* **47**, 4193 (1993).
- [55] M. V. Ammosov, N. B. Delone and V. P. Krainov. *Sov. Phys. JETP* **64**, 1191 (1986).
- [56] S. Augst, D. D. Meyerhofer, D. Strikland and S. L. Chin. *J. Opt. Soc. Am. B* **8**, 858 (1991).

- [57] I. V. Keldysh. Sov. Phys. JETP **20**, 1307 (1965).
- [58] P. Lambropoulos. Phys. Rev. Lett. **55**, 2141 (1985).
- [59] L. A. Lompré, G. Mainfray, C. Manus, S. Repoux and J. Thebault. Phys. Rev. Lett. **36**, 949 (1976).
- [60] K. Nakazawa, T. Onodera and M. Sasago. Jap. J. Appl. Phys. 1 **38**, 3001 (1999).
- [61] M. Ferray, A. L'Huillier, X. F. Li, L. A. Lompré, G. Mainfray and C. Manus. J. Phys. B **21**, L31 (1988).
- [62] J. Wildenauer. J. Appl. Phys. **62**, 41 (1988).
- [63] C.-G. Wahlström, J. Larsson, A. Persson, T. Starczewski, S. Svanberg, P. Salières, P. Balcou and A. L'Huillier. Phys. Rev. A **48**, 4709 (1993).
- [64] K. Miyazaki and H. Takada. Phys. Rev. A **52**, 3007 (1995).
- [65] M. Schnürer, C. Spielmann, P. Wobrauschek, N. H. B. C. Strelti, C. Kan, K. Ferencz, R. Koppitsch, Z. Cheng, T. Brabec and F. Krausz. Phys. Rev. Lett. **80**, 3236 (1998).
- [66] P. B. Corkum. Phys. Rev. Lett. **71**, 1994 (1993).
- [67] K. C. Kulander, K. J. Schafer and J. L. Krause. In *Proceedings of the Workshop, Super Intense laser Atom Physics (SILAP) III*, edited by B. Piroux (Plenum Press, New York, 1994).
- [68] J. L. Krause, K. J. Schafer and K. C. Kulander. Phys. Rev. A **45**, 4998 (1992).
- [69] M. Lewenstein, P. Balcou, M. Y. Ivanov, A. L'Huillier and P. B. Corkum. Phys. Rev. A **49**, 2117 (1994).
- [70] L. Gao, X. Li, P. Fu, R. R. Freeman and D.-S. Guo. Phys. Rev. A **61**, 063407 (2000).
- [71] T. Cheng, X. Li, S. Ao, L.-A. Wu and P. Fu. Phys. Rev. A **68**, 033411 (2003).
- [72] S. Meyer, B. N. Chichkov, B. Wellegehausen and A. Sanpera. Phys. Rev. A **61**, 063811 (2000).
- [73] C.-G. Wahlström. Physica Scripta **49**, 201 (1994).
- [74] M. Protopapas, C. H. Keitel and P. L. Knight. Rep. Prog. Phys. **60**, 389 (1997).
- [75] L. A. Lompré, A. L'Huillier, M. Ferray, P. Monot, G. Mainfray and C. Manus. J. Opt. Soc. Am B **7**, 754 (1990).
- [76] B. W. Shore and K. C. Kulander. J. Mod. Opt **36**, 857 (1989).
- [77] A. L'Huillier, K. J. Schafer and K. C. Kulander. Phys. Rev. Lett. **66**, 2200 (1991).
- [78] A. L'Huillier, L. A. Lompré, G. Mainfray and C. Manus. *Atoms in Intense Laser Fields*, 139 (Accademic Press, New York, 1992).
- [79] H. T. Kim, I. J. Kim, K.-H. Hong, D. G. Lee, J.-H. Kim and C. H. Nam. J. Phys. B **37**, 1141 (2004).
- [80] L. Nugent-Glandorf, M. Scheer, M. Krishnamurthy, J. W. Odom and S. R. Leone. Phys. Rev. A **62**, 023812 (2000).
- [81] L. Nugent-Glandorf, M. Scheer, D. A. Samuels, V. Bierbaum and S. R. Leone. Rev. Sci. Instrum. **73**, 1875 (2002).
- [82] D. Riedel, J. L. Hernandez-Pozos, R. E. Palmer, S. Baggott, K. W. Kolasinski and J. S. Foord. Rev. Sci. Instrum. **72**, 1977 (2001).
- [83] P. Balcou, P. Salières, K. S. Budil, T. Ditmire, M. D. Perry and A. L'Huillier. Z. Phys. D **34**, 107 (1995).
- [84] S. Cavalieri, M. Materazzi and R. Eramo. Opt. Laser Eng. **37**, 577 (2002).
- [85] S. Cavalieri, R. Eramo, M. Materazzi, C. Corsi and M. Bellini. Phys. Rev. Lett. **89**, 133002 (2002).
- [86] M. M. Salour and C. Cohen-Tannoudji. Phys. Rev. Lett. **38**, 757 (1977).

- [87] R. Teets, J. Eckstein and T. W. Hänsch. *Phys. Rev. Lett.* **38**, 760 (1977).
- [88] M. M. Salour. *Rev. Mod. Phys.* **50**, 667 (1978).
- [89] S. Witte, R. T. Zinkstok, W. Hogervorst and K. S. E. Eikema. *Appl. Phys. B* **78**, 5 (2004).
- [90] M. B. Gaarde, P. Antoine, A. Persson, B. Carré, A. L'Huillier and C.-G. Wahlström. *J. Phys. B* **29**, L163 (1996).
- [91] H. Eichmann, S. Meyer, K. Riepel, C. Momma and B. Wellegehausen. *Phys. Rev. A* **50**, R2834 (1994).
- [92] M. Bellini. *Appl. Phys. B* **70**, 773 (2000).
- [93] B. Shan, A. Cavalieri and Z. Chang. *Appl. Phys. B* **74**, S23 (2002).
- [94] C. Altucci, R. Bruzzese, C. de Lisio, M. Nisoli, S. Stagira, S. D. Silvestri, O. Svelto, A. Boscolo, P. Ceccherini, L. Poletto, G. Tondello and P. Villoresi. *Phys. Rev. A* **61**, 021801(R) (1999).
- [95] C. Altucci, R. Bruzzese, C. de Lisio, M. Nisoli, G. Cerullo, S. Stagira, S. D. Silvestri, O. Svelto, A. Boscolo, P. Ceccherini, L. Poletto, G. Tondello and P. Villoresi. *J. Opt. A* **2**, 289 (2000).
- [96] H. T. Kim, D. G. Lee, K.-H. Hong, J.-H. Kim, I. W. Choi and C. H. Nam. *Phys. Rev. A* **67**, 051801(R) (2003).
- [97] C. Lyngå, F. Oessler, T. Metz and J. Larsson. *Appl. Phys. B* **72**, 913 (2001).
- [98] J. Larsson, E. Mevel, R. Zerne, A. L'Huillier, C.-G. Wahlström and S. Svanberg. *J. Phys. B* **28**, L53 (1995).
- [99] A. Johansson, M. K. Raarup, Z. S. Li, V. Lokhnygin, D. Descamps, C. Lyngå, E. Mevel, J. Larsson, C.-G. Wahlström, S. Aloise, M. Gisselbrecht, M. Meyer and A. L'Huillier. *Eur. Phys. J. D* **22**, 3 (2003).
- [100] P. Cacciani, F. Brandi, I. Velchev, C. Lyngå, C.-G. Wahlström and W. Ubachs. *Eur. Phys. J. D* **15**, 47 (2001).
- [101] A. L'Huillier, D. Descamps, A. Johansson, J. Norin, J. Mauritsson and C.-G. Wahlström. *Eur. Phys. J. D* **26**, 91 (2003).
- [102] L. Nahon, C. Alcazar, J.-L. Markats, B. Lagarde, F. Polack, R. Thissen, D. Lepère and K. Ito. *Rev. Sci. Instrum.* **72**, 1320 (2001).
- [103] T. Feder. *Phys. Today* **53**, 47 (2000).
- [104] H. Eichmann, A. Egbert, C. Momma, B. Wellegehausen, W. Becker, S. Long and J. K. McIver. *Phys. Rev. A* **51**, R3414 (1995).
- [105] F. Brandi, I. Velchev, W. Hogervorst and W. Ubachs. *Phys. Rev. A* **64**, 032505 (2001).
- [106] K. S. E. Eikema, W. Ubachs and W. Hogervorst. *Phys. Rev. A* **49**, 803 (1994).
- [107] I. Velchev, W. Hogervorst and W. Ubachs. *J. Phys. B* **32**, L511 (1999).
- [108] M. Plimmer, P. Baird, C. Foot, D. Stacey, J. Swan and G. Woodgate. *J. Phys. B* **22**, L241 (1989).
- [109] S. C. Xu, R. van Dierendonck, W. Hogervorst and W. Ubachs. *J. Mol. Spectr.* **201**, 256 (2000).
- [110] H. Kopfermann. *Nuclear Moments* (Accademic Press, New York, 1958).
- [111] W. H. King. *Isotope Shifts in Atomic Spectra* (Plenum Press, New York, 1984).
- [112] P. Aufmuth, K. Heilig and A. Steudel. *At. Data Nucl. Data Tables* **37**, 455 (1987).
- [113] P. Aufmuth and M. Hاونert. *Physica B & C* **123C**, 109 (1983).
- [114] F. Schneider. Ph.D. thesis, Freie Universität Berlin (1985).

- [115] H. Geisen, T. Krumpelmann, D. Neuschafer and C. Ottinger. *Phys. Lett. A* **130**, 299 (1988).
- [116] K. Yoshino and D. E. Freeman. *J. Opt. Soc. Am. B* **2**, 1268 (1985).
- [117] R. Knight and L.-G. Wang. *J. Opt. Soc. Am. B* **2**, 1084 (1985).
- [118] C. J. Humphreys and E. J. Paul. *J. Opt. Soc. Am.* **60**, 1302 (1970).
- [119] D. Jackson and M. Coulombe. *Proc. R. Soc. Lond.* **343**, 453 (1975).
- [120] D. Jackson and M. Coulombe. *Proc. R. Soc. Lond.* **338**, 277 (1974).
- [121] F. Brandi, W. Hogervorst and W. Ubachs. *J. Phys. B* **35**, 1071 (2002).
- [122] S. Yoon and W. L. Glab. *J. Phys. B* **27**, 4133 (1994).
- [123] K. S. E. Eikema, W. Ubachs, W. Vassen and W. Hogervorst. *Phys. Rev. Lett.* **71**, 1690 (1993).
- [124] I. Velchev, R. van Dierendonck, W. Hogervorst and W. Ubachs. *J. Mol. Spectr.* **187**, 21 (1998).
- [125] M. S. Fee, K. Danzmann and S. Chu. *Phys. Rev. A* **45**, 4911 (1992).
- [126] S. Gangopadhyay, N. Melikechi and E. E. Eyler. *J. Opt. Soc. Am B* **11**, 231 (1994).
- [127] N. Melikechi, S. Gangopadhyay and E. E. Eyler. *J. Opt. Soc. Am B* **11**, 2402 (1994).
- [128] V. Kaufman. *J. Res. Natl. Inst. Stand. Technol.* **98**, 717 (1993).
- [129] B. D. Cannon and G. R. Janik. *Phys. Rev. A* **42**, 397 (1990).
- [130] M. Keim, E. Arnold, W. Borchers, U. Georg, A. Klein, R. Neugart, L. Vermeeren, R. E. Silverans and P. Lievens. *Nucl. Phys. A* **586**, 219 (1995).
- [131] H. A. Schuessler, A. Alousi, R. M. Evans, M. Brieger, F. Buchinger and Y. F. Li. *Phys. Rev. Lett* **65**, 1332 (1990).
- [132] V. Kaufman and J. Humphreys. *J. Opt. Soc. Am* **59**, 1614 (1969).
- [133] D. Klar, M. Aslam, M. A. Baig, K. Ueda, M.-W. Ruf and H. Hotop. *J. Phys. B* **34**, 2402 (2001).
- [134] J. C. Camparo and P. P. Lambropoulos. *J. Opt. Soc. Am B* **19**, 2163 (1992).
- [135] M. S. Pindzola, A. H. Glasser and M. G. Payne. *Phys. Rev A* **30**, 1800 (1984).
- [136] J. C. Camparo and P. P. Lambropoulos. *Opt. Comm.* **137**, 413 (1997).
- [137] C. Dorman, I. Kucukkara and J. P. Marangos. *Phys. Rev. A* **61**, 013802 (1999).
- [138] C. E. Moore. *Atomic Energy Levels*, vol. 2, 170 (Washington, DC: US Government Printing Office, 1952).
- [139] K. Yoshino and Y. Tanaka. *J. Opt. Soc. Am* **69**, 159 (1979).
- [140] C. Delsart, J.-C. Keller and C. Thomas. *J. Phys. B* **14**, 4241 (1981).
- [141] J. Sugar and A. Musgrove. *J. Phys. Chem. Ref. Data* **20**, 859 (1991).
- [142] M. Bounakhla, J. P. Lemoigne, J. P. Grandin, X. Husson, H. Kucal and M. Aymar. *J. Phys. B* **26**, 345 (1993).
- [143] J. Bömmels, J. M. Weber, A. Gopalan, N. Herschbach, E. Leber, A. Schramm, K. Ueda, M.-W. Ruf and H. Hotop. *J. Phys. B* **32**, 2399 (1999).
- [144] F. Brandi, I. Velchev, D. Neshev, W. Hogervorst and W. Ubachs. *Rev. Sci. Instrum.* **74**, 32 (2003).
- [145] C. Spielmann, N. H. Burnett, S. Sartania, R. Koppitsch, M. Schnurer, C. Kan, M. Lenzner, P. Wobrauschek and F. Krausz. *Science* **278**, 661 (1997).
- [146] P. A. Heimann, M. Koike, C. W. Hsu, D. Blank, X. M. Yang, A. G. Suits, Y. T. Lee, M. Evans, C. Y. Ng, C. Flaim and H. A. Padmore. *Rev. Sci. Instrum.* **68**, 1945 (1997).
- [147] W. Schade, B. Garbe and V. Helbig. *Appl. Opt.* **29**, 3950 (1990).

- [148] P. P. Yaney, D. A. V. Kliner, P. E. Schrader and R. Farrow. *Rev. Sci. Instrum.* **71**, 1296 (2000).
- [149] P. Cacciani, W. Ubachs, P. C. Hinnen, C. Lyngå, A. L'Huillier and C. G. Wahlström. *Astrophys. Jour.* **499**, L223 (1998).
- [150] S. Schiemann, W. Ubachs and W. Hogervorst. *IEEE J. Quantum Electron.* **33**, 358 (1997).
- [151] S. Schiemann, W. Hogervorst and W. Ubachs. *IEEE J. Quantum Electron.* **34**, 407 (1998).
- [152] D. Neshev, I. Velchev, W. Majewski, W. Hogervorst and W. Ubachs. *Appl. Phys. B* **68**, 671 (1999).
- [153] H. Knöckel, S. Kremser, B. Bodermann and E. Tiemann. *Z. Phys. D* **37**, 43 (1996).
- [154] N. Hodgson and H. Weber. *Optical Resonators* (Springer, London, 1997).
- [155] F. Brandi, D. Neshev and W. Ubachs. *Phys. Rev. Lett.* **91**, 163901 (2003).
- [156] M. Drescher, M. Hentschel, R. Kienberg, G. Tempea, C. Spielmann, G. A. Reider, P. B. Corkum and F. Krausz. *Science* **291**, 1923 (2001).
- [157] R. A. Bartels, A. Paul, H. Green, H. C. Kapteyn, M. M. Murnane, S. Backus, I. P. Christov, Y. Liu, D. Attwood and C. Jacobsen. *Science* **297**, 376 (2002).
- [158] L. Minnhagen. *J. Opt. Soc. Am* **63**, 1185 (1973).
- [159] G. W. F. Drake and W. C. Martin. *Can. J. Phys.* **76**, 679 (1998).
- [160] J. J. Macklin, J. D. Kmetec and C. L. Gordon. *Phys. Rev. Lett.* **70**, 766 (1993).
- [161] P. Salières, A. L'Huillier, P. Antoine and M. Lewenstein. *Adv. At. Mol. and Opt. Phys.* **41**, 83 (1998).
- [162] D. G. Lee, J.-H. Kim, K.-H. Hong and C. H. Nam. *Phys. Rev. Lett.* **87**, 243902 (2001).
- [163] M. Lewenstein, P. Salières and A. L'Huillier. *Phys. Rev. A* **52**, 4747 (1995).
- [164] C. Kan, C. E. Capjack, R. Rankin and N. H. Burnett. *Phys. Rev. A* **52**, R4336 (1995).
- [165] E. Yablonovitch. *Phys. Rev. A* **10**, 1888 (1974).
- [166] E. Yablonovitch. *Phys. Rev. Lett.* **60**, 795 (1988).
- [167] H. J. Shin, D. G. Lee, Y. H. Cha, K. H. Hong and C. H. Nam. *Phys. Rev. Lett.* **83**, 2544 (1999).
- [168] H. J. Shin, D. G. Lee, Y. H. Cha, J.-H. Kim, K. H. Hong and C. H. Nam. *Phys. Rev. A* **63**, 053407 (2001).
- [169] D. Proch and T. Trickl. *Rev. Sci. Instrum.* **60**, 713 (1988).
- [170] E. T. J. Nibbering, G. Grillon, M. A. Franco, B. S. Prade and A. Mysyrowicz. *J. Opt. Soc. Am. B* **14**, 650 (1997).
- [171] R. L. Sutherland. *Handbook of nonlinear optics* (Marcel Dekker, New York, 1996).
- [172] J.-H. Kim, D. G. Lee, H. J. Shin, J.-H. Kim and C. H. Nam. *Phys. Rev. A* **63**, 063403 (2001).
- [173] M. B. Gaarde, F. Salin, E. Constant, P. Balcou, K. J. Schafer, K. C. Kulander and A. L'Huillier. *Phys. Rev. A* **59**, 1376 (1999).
- [174] T. Sekikawa, T. Katsura, S. Miura and S. Watanabe. *Phys. Rev. Lett.* **88**, 193902 (2002).
- [175] T. M. Miller, A. E. S. Miller, J. F. Paulson and X. J. Liu. *J. Chem. Phys.* **100**, 8841 (1994).